

X-ray Study of the Variable Neutral Iron Line Emission of
the Sgr B2 Complex in the Galactic Center Region

Tatsuya Inui
Department of Physics, Faculty of Science
Graduate School of Kyoto University

March 13, 2008

Abstract

We report the first discovery of the neutral iron line variability in the Galactic molecular complex Sgr B2. This discovery is a crucial hint not only for the origin of the neutral iron line emission in the Galactic center but also for the past activity of the quiescent Galactic center black hole Sgr A* in the present.

We operate a comparison analysis with the past observations from 1994 to 2005. We make the cross calibration of the absolute efficiency among the four different observatories using the invariable 6.67 keV line and find a clear variability of the 6.40 keV line emission. The variability is primarily originated from the two distinct sources, M 0.66–0.02 (Sgr B2 cloud) and G 0.570–0.018. The intensity of the 6.40 keV line has a peak in 2000 and decreases to 66% in five years. The ten year time scale of variability requires that the origin invoking the 6.40 keV line emission has nearly a light speed, strongly supporting the X-ray reflection scenerio. At the same time, the 6.40 keV light curve indicates the past activity of the irradiating source. The most possible source is the Galactic center black hole Sgr A*, which was thought to be in an active phase about 300 years ago. We now see a decay of the giant flare through the 6.40 keV line of the molecular clouds.

The high energy resolving power of the Suzaku XIS provides the separate maps of the K-shell transition lines from Fe I (6.40 keV) and Fe XXV (6.67 keV) and has discovered new X-ray sources from each map. Whereas the 6.67 keV lines are smoothly distributed over the Sgr B2 region, which is due to the Galactic hot plasma, a local excess is found near at $(l, b) = (0^\circ 61, 0^\circ 01)$, possibly due to a new young SNR. The plasma temperature is $kT = 3$ keV and the age is estimated to be younger than 7×10^3 years. The 6.40 keV image is clumpy with local excesses near at the Sgr B2 cloud and at $(l, b) = (0^\circ 74, -0^\circ 09)$. Since the spectral features are quite similar to those of the Sgr B2 cloud, the other excess can be a new X-ray reflection nebulae (XRN).

Contents

1	Introduction	1
2	Review	3
2.1	The Galactic Center Region	3
2.1.1	Galactic Nucleus Sgr A*	3
2.1.2	The Galactic Center Diffuse X-ray Emission	5
2.1.3	Supernova Remnants	8
2.1.4	Giant Molecular Complexes	8
2.2	A Giant Molecular Complex — Sgr B	12
2.2.1	Sgr B2	12
2.2.2	Sgr B1	14
2.3	X-ray Emission Processes from Neutral Elements	14
2.3.1	Photoionizaion	14
2.3.2	Collisional Ionization by Electrons	14
2.3.3	Collisional Ionization by Fast Ions	18
3	Instruments	20
3.1	X-ray Satellites and their Mirrors	20
3.1.1	ASCA	20
3.1.2	Chandra	22
3.1.3	XMM-Newton	25
3.1.4	Suzaku	28
3.2	CCD cameras	29
3.2.1	SIS	30
3.2.2	ACIS	33
3.2.3	EPIC	36
3.2.4	XIS	39
4	Observations	49
4.1	The Suzaku Observation	49
4.1.1	Data Collection	49
4.1.2	The Gain Tuning	49
4.1.3	The Position Tuning	50
4.2	The XMM-Newton Observations	50
4.2.1	Data Collection	50

4.2.2	The Position Tuning	53
4.3	The Chandra Observations	53
4.3.1	Data Collection	53
4.3.2	Position Accuracy	54
4.4	The ASCA Observations	55
4.4.1	Data Collection	55
4.4.2	The Position Tuning	55
5	Result I — Suzaku Discoveries of New Diffuse Sources	56
5.1	Suzaku Overview of the Sgr B2 Region	56
5.2	New Diffuse Sources	60
5.2.1	SNR Candidate — G 0.61+0.01	60
5.2.2	XRN Candidate — M 0.79–0.09	66
6	Result II — Time Variabilities of Neutral Iron Line	74
6.1	Spectral Analysis and Error Estimation	74
6.1.1	Suzaku	75
6.1.2	XMM-Newton	77
6.1.3	Chandra	81
6.1.4	ASCA	81
6.1.5	Comparison Analysis	82
6.2	Variability Verifications on Individual Sources	86
6.2.1	Surface Brightness Mapping	86
6.2.2	M 0.66–0.02	86
6.2.3	G 0.570–0.018	93
7	Summary and Discussion	96
7.1	Ionized Iron Line Sources	96
7.1.1	Galactic Center Diffuse X-ray Emission	96
7.1.2	Supernova Remnants	96
7.2	Neutral Iron Line Sources	97
7.2.1	The Origin	97
7.2.2	Relation to the Past Activity of Sgr A*	98
A	Tables for Spectral Results of M 0.66–0.02	104
A.1	Continuum Models	104
A.2	Background Analysis of the MOS and the PN detector	104
B	Tables for Spectral Results of G 0.570–0.018	110
B.1	Continuum Models	110
B.2	Background Analysis of the MOS and the PN detector	110

List of Figures

2.1	Adaptively smoothed 0.5–7.0 keV image of Sgr A* overlaid contours of VLA 6 cm (Baganoff et al. 2003).	4
2.2	Wideband spectrum of Sgr A*. The spectrum of Sgr A* is based on measurements at 7 mm, 450 μm , 850 μm , 3.6 μm , 1.6 μm , and X-rays at 1 keV. The quiescent X-ray and near-IR fluxes are taken from Baganoff et al. (2001), Genzel et al. (2003), and Ghez et al. (2005). The quiescent flux is shown in blue color and the flux associated with flaring activity including the X-ray flare is shown in red color. The hard gamma ray emission from the Galactic center at 1 TeV based on HESS observations (Aharonian et al. 2004) and the high fluxes from INTEGRAL observations are not connected and are only shown by themselves in black. Further descriptions are shown in Yusef-Zadeh et al. (2006).	6
2.3	6.7 keV narrow band image of the Galactic Center obtained with the Suzaku XIS.	7
2.4	2.45 keV narrow band image of the Galactic Center obtained with the Suzaku XIS.	9
2.5	Velocity-integrated CS $J=1-0$ emission in the Galactic center region (Tsuboi et al. 1999). The velocity integrated range is from -200 to 200 km s^{-1}	10
2.6	6.4 keV narrow band image of the Galactic Center with the Suzaku XIS.	11
2.7	2–10 keV band image of Sgr B2 obtained with the Chandra ACIS (Takagi et al. 2002), overlaid on contours of H II regions (Gaume et al. 1995). The solid circles indicate X-ray point sources.	12
2.8	Adaptively smoothed Chandra image in the 6.15–6.55 keV band (Murakami et al. 2001), overlaid on contours of ^{13}CO line flux (Sato et al. 2000) .	13
2.9	(a) Cross sections for K-shell ionization of various atoms. Solid curves indicate the calculated result by electron impacts from the semi-empirical formula. Dashed curves indicate cross sections for K-shell photoionization of N and Fe. (b) Stopping range of low-energy electrons in hydrogen. See Tatischeff (2003) for detail descriptions. . . .	15

2.10	Simulated equivalent width of fluorescent Fe K line as a function of the thickness N_{H} of scattering matter. The simulation is made in the following cases; I: primary source is directly observed, II: X-rays from primary source are absorbed by a surrounding matter, III: primary source is totally hidden or scattering matter is irradiated by an external source.	16
2.11	X-ray emission produced by suprathermal electrons with the source spectrum of $\propto E_e^{-2}$ interacting in a thick target composed of a neutral atomic gas of the solar abundance. The dashed line shows the effect of photoelectric absorption, with a H column density of $4 \times 10^{21} \text{ cm}^{-2}$	17
2.12	X-ray emission produced by fast ions with cosmic-ray source (CRS) composition. IB: inverse bremsstrahlung; SEB: secondary electron bremsstrahlung; RRC: radiative recombination continuum. See Tatischeff (2003) for detailed descriptions.	19
3.1	Schematic pictures of the ASCA (upper left), Chandra (upper right), XMM-Newton (lower left) and Suzaku satellites (lower right).	21
3.2	ASCA XRT effective area (one telescope) for different off-axis angle (θ) and azimuthal angle (ϕ).	23
3.3	The four nested HRMA mirror pairs and associated structures. See http://cxc.harvard.edu/proposer/POG/html/HRMA.html	24
3.4	The HRMA/ACIS and HRMA/HRC effective areas versus X-ray energy in linear (top) and log (bottom) scale.	26
3.5	The net effective area of all XMM-Newton X-ray telescopes, EPIC and RGS.	27
3.6	Effective area of one XRT + XIS system, for both the FI and BI chips. (No contamination included)	29
3.7	Cross section of SIS (Gendreau 1995).	31
3.8	Left: Four individual CCDs are combined in a single package to make a single SIS focal plane (Gendreau 1995). Right: Configuration of the two SIS on the ASCA focal plane.	31
3.9	Energy resolution of the GIS and the SIS. For the SIS, measured or estimated energy resolutions of SIS1 in the 1CCD mode are plotted for at launch and 1, 2, 3, 4 and 5 years after the launch.	32
3.10	The SIS spectrum for the dark earth data (Gendreau 1995).	33
3.11	A schematic drawing of the ACIS focal plane; insight to the terminology is given in the lower left. Note the nominal aimpoints: on S3 (the '+') and on I3 (the 'x') (Weisskopf et al. 2003).	34
3.12	The ACIS background spectra of I0 (black) and S3 (red) extracted from the Chandra blank-sky database.	35
3.13	An example of the ACIS background counting rate versus time: S3 (the BI chip; top curve) and I2 (the FI chip; bottom curve).	37
3.14	A sketch of the field of view of the two types of EPIC camera; MOS (left) and PN (right).	38

3.15	Energy resolution of MOS1-CCD1 (red asterisk), MOS2-CCD1 (green square) and PN-CCD4 (black triangle).	39
3.16	Upper: Background spectra for the MOS1 camera (left) and the PN camera (right) during an observation with the filter wheel in the closed position. Lower: Images of the MOS camera of Al K line at 1.48 keV (left) and the PN of Cu K at 8.04 keV (right) (Carter & Read 2007).	40
3.17	Layout of the XRTs on the Suzaku spacecraft.	41
3.18	One XIS instrument.	42
3.19	The time history of the energy resolution for Mn K α from the ^{55}Fe calibration sources for XIS.	44
3.20	The XIS background rate for each of the four XIS detectors, with prominent fluorescent lines marked. These spectra are based on the observations of the dark Earth for ~ 800 ks.	45
3.21	ACTY dependence of the NXB for XIS1 and XIS2.	47
3.22	Cut-off rigidity dependence of the NXB (average intensity in 5–10 keV) for each sensor.	48
4.1	The Suzaku image of the Sgr B region in the 2–10 keV band. All the four XIS data are co-added. The dotted square is the XIS field of view (FOV).	51
4.2	Background light curves of 2001 (left) and 2004 (right) observations with the MOS and the PN detectors. Events with over 10 keV and pattern 0 are accumulated. Horizontal lines indicate the screening criteria (0.4 counts s $^{-1}$ for MOS and 1.0 counts s $^{-1}$ for PN).	52
4.3	The XMM-Newton image of the Sgr B region in the 0.3–10 keV band. All MOS and PN data in 2004 are co-added. Circles indicate point sources identified with the Chandra point source catalogue (Muno et al. 2003).	53
4.4	The distribution of the Chandra aspect offsets (Weisskopf et al. 2003).	54
5.1	The X-ray spectra from the full FOV of the XIS, except the CCD corners irradiated by the build-in calibration sources. All four XIS data sets are co-added.	57
5.2	Fluxes of the 6.40 keV (a) and the 6.67 keV lines (b), the flux ratio of 6.97 keV/6.67 keV (c), and the continuum flux (normalization of the 7-keV bremsstrahlung) map (d). The embedded numbers are fluxes in units of 10^{-6} photons cm $^{-2}$ s $^{-1}$ arcmin $^{-2}$ or flux ratios. The color means that the average value is white, and the increasing (decreasing) excess above (below) the average is given with increasing deepness of red (green), where the maximum (minimum) is 2.0 (0.1) times of the average value.	59

5.3	The 6.67 keV line map (the 6.58–6.74 keV band map) showing bright spot at the northwest corner with the 2–5 keV continuum map as green contours. The fluxes are normalized by the 6.7 keV flat-field image. The source and background regions are shown by the white solid and dotted ellipses, respectively.	60
5.4	The exposure corrected 6.67 keV line maps of (a) Chandra 2000 and (b) XMM-Newton 2004. The source regions are shown by the solid circles.	62
5.5	Top: the X-ray spectrum of the sum of 3 FI CCDs (XIS0, 2 and 3) for the new SNR (G 0.61+0.01) with the best-fit VPSHOCK model. Bottom: same as the top, but of the BI CCD (XIS1).	63
5.6	The 6.40 keV line map (the 6.33–6.46 keV band map) showing bright spots at the Sgr B2 cloud and M 0.74-0.09. The fluxes are normalized by the 6.40 keV flat-field image. The sources and background regions are shown by the solid circles and dotted ellipse, respectively.	67
5.7	The exposure corrected 6.40 keV line maps of (a) Chandra in 2000 and (b) XMM-Newton in 2004. The source regions are shown by the solid circles.	69
5.8	Top: the X-ray spectrum of the sum of the 3 FI CCDs (XIS0, 2 and 3) for M 0.66–0.02 (Sgr B2 cloud) with an absorbed power-law model and two Gaussian lines. Bottom: same as the top but of the BI CCD (XIS1).	70
5.9	Same as figure 5.8, but for a new source M 0.74-0.09.	71
6.1	The XMM-Newton image in 6–7 keV band. The source region for the Sgr B2 region is described in a solid line. Dashed line circles are individual sources discovered in this region.	75
6.2	The blank-sky-subtracted spectra of the Sgr B2 region, with the Suzaku XIS FI sensors (a) and BI sensor (b) in 2005, XMM-Newton MOS (c) and PN (d) in 2004, (e) and (f) in 2001, Chandra ACIS-I (g) in 2001 and (h) in 2000, and ASCA SIS (i) in 1994. The solid lines indicate the best-fit models (see text).	76
6.3	The 6.67 keV line surface brightness obtained with each observation in the Sgr B2 region. In this plot, each error bar indicates the 90% confidence. The values are marked with red circles for Model I, green x marks for Model II, blue squares for Model III and aqua triangles for Model IV.	83
6.4	The 6.67 keV line surface brightness with Model I but each error bar in this plot indicates one sigma statistical error plus the systematic error of the detector. The data are marked with a triangle mark for Suzaku, a circle for XMM-Newton, an asterisk for Chandra and a square for ASCA. The average flux is shown in a solid horizontal line.	84
6.5	The light curve of the corrected 6.40 keV line surface brightness in the Sgr B2 region. The XMM-Newton values are the average of MOS and PN. In this plot, each error bar indicates the 90% confidence limit.	85

6.6	The surface brightness maps of iron lines obtained with (a) Suzaku XIS 2005, (b) XMM-Newton MOS and PN 2004, (c) Chandra ACIS-I 2000, and (d) ASCA SIS 1994. Each pixel size is $50'' \times 50''$	87
6.7	The spectra for M0.66–0.02 obtained with Suzaku XIS FI sensors (a) and BI sensor (b) in 2005, XMM-Newton MOS (c) and PN (d) in 2004, (e) and (f) in 2001, Chandra ACIS-I (g) in 2000, and ASCA SIS (h) in 1994. The solid lines indicate the best-fit models with Model I.	88
6.8	The 6.67 keV line surface brightness obtained with each observation in M0.66–0.02. In this plot, each error bar indicates the 90% confidence. The values are marked with red circles for Model I, green x marks for Model II, blue squares for Model III and aqua triangles for Model IV.	90
6.9	The light curve of the 6.40 keV line surface brightness from M0.66–0.02 (Sgr B2 cloud). In this plot, each error bar indicates the 90% confidence limit.	91
6.10	The spectra for G0.570–0.018 obtained with Suzaku XIS FI sensors (a) and BI sensor (b) in 2005, XMM-Newton MOS (c) and PN (d) in 2004, (e) and (f) in 2001, Chandra ACIS-I (g) in 2000, and ASCA SIS (h) in 1994. The solid lines indicate the best-fit models.	92
6.11	The light curve of the 6.40 keV line surface brightness from G 0.570–0.018. In this plot, each error bar indicates the 90% confidence limit.	95
7.1	The time trend of the continuum fluxes in M0.66–0.02. XMM values in 2001 and 2004 are the average of MOS and PN. In this plot, each error bar indicates the 90% confidence limit.	98

List of Tables

3.1	Comparison of X-ray telescopes	21
3.2	Comparison of X-ray CCDs	30
4.1	Observation data list	49
5.1	The best-fit parameters for G 0.61+0.01 with the VPSHOCK model plus two emission lines	64
5.2	The physical parameters of G 0.61+0.01	66
5.3	The result of spectral fittings of M 0.66–0.02 (Sgr B2 cloud) and M 0.74–0.09 with a power-law and two Gaussian models.	73
6.1	The Suzaku result of spectral fitting for the Sgr B2 region	78
6.2	The XMM-Newton 2004 result of spectral fitting for the Sgr B2 region	79
6.3	The XMM-Newton 2001 result of spectral fitting for the Sgr B2 region	79
6.4	The XMM-Newton 2004 results of spectral fitting for the Sgr B2 region with multiplied blank-sky backgrounds	80
6.5	The XMM-Newton 2001 results of spectral fitting for the Sgr B2 region with multiplied blank-sky backgrounds	81
6.6	The Chandra 2000 and 2001 results of spectral fitting for the Sgr B2 region	82
6.7	The ASCA 1994 result of spectral fitting for the Sgr B2 region	83
6.8	The result of spectral fitting for M 0.66–0.02 with Model I	89
6.9	The result of spectral fitting for G 0.570–0.018 with Model I plus one Gaussian function	94
A.1	The result of spectral fitting for M 0.66–0.02 with Model II	105
A.2	The result of spectral fitting for M 0.66–0.02 with Model III	106
A.3	The result of spectral fitting for M 0.66–0.02 with Model IV	107
A.4	The XMM-Newton 2004 results of spectral fitting for M 0.66–0.02 with multiplied blank-sky backgrounds	108
A.5	The XMM-Newton 2001 results of spectral fitting for M 0.66–0.02 with multiplied blank-sky backgrounds	109
B.1	The result of spectral fitting for G 0.570–0.018 with Model II plus one Gaussian function	111
B.2	The result of spectral fitting for G 0.570–0.018 with Model III plus one Gaussian function	112

B.3	The result of spectral fitting for G 0.570–0.018 with Model IV plus one Gaussian function	113
B.4	The XMM-Newton 2004 results of spectral fitting for G 0.570–0.018 with multiplied blank-sky backgrounds	114
B.5	The XMM-Newton 2001 results of spectral fitting for G 0.570–0.018 with multiplied blank-sky backgrounds	115

Chapter 1

Introduction

The Milky Way galaxy, our Galaxy, harbors the closest massive black hole at the center. The Galactic center (GC), crowded with various objects, is one of the most interesting targets in astronomy. The most puzzling problem is the central super massive black hole with anomalously low luminosity.

One key to solve this problem was found with the past X-ray observations of the Galactic molecular clouds whose temperature is too low to emit X-ray photons by themselves. The discovery of neutral iron fluorescence line emission with the ASCA and Chandra X-ray satellites suggested that the possible irradiating source is the central supermassive black hole Sgr A* and that 300 years ago the luminosity was six order larger than that at the present. Murakami (2002) summarized these results of the past observations. However, this hypothesis still has two problems. Firstly, the neutral iron line emission can be also produced by energetic cosmic particles. Secondly, no time variability of the line emission had been found expected in this hypothesis.

In this thesis, we shed light on the largest Galactic molecular complex Sgr B2 with the strongest neutral iron line emission and aim to solve these problems. Noted above, the GC region is the complex area with hot plasma, supernova remnants (SNRs), HII regions and so on. The first objective is to reveal the emission structure all over the Sgr B2 region with the high performance of detecting a faint diffuse emission of the Suzaku X-ray satellite. The second objective is to find the time variability of neutral iron line emission from molecular clouds by comparing the past observations.

In chapter 2, we review the observational results of our Galactic center and the Sgr B2 region, and X-ray line emission processes from neutral elements in a cool molecular cloud. We use X-ray data obtained with CCD cameras onboard four different satellites. We introduce the characteristics of the X-ray satellites,

particularly their efficiencies and backgrounds, in chapter 3. We explain the data reduction processes for the observations in chapter 4. In chapter 5, we report the results of the Suzaku observation for the first objective. In chapter 6, we report the discovery of time variability of the neutral iron line by a comparison analysis using the past observations with the precise systematic error study of each instrument. Finally we discuss and summarize these results in chapter 7.

Chapter 2

Review

2.1 The Galactic Center Region

The GC region, shrouded by the intervening gas and dust, is actively explored at radio, infrared, X-ray and gamma ray bands. The environment of the GC is so complex that many components coexist within a central deep gravitational potential well. The principal components are the supermassive black hole Sagittarius A* (Sgr A*), surrounding clusters of stars, ionized gas streamers, diffuse hot gas, supernova remnants and molecular rings. Hereafter, we assume 8.5 kpc as the distance to the GC (Reid et al. 1988) and $6 \times 10^{22} \text{ cm}^{-2}$ as the Galactic absorption hydrogen column density.

2.1.1 Galactic Nucleus Sgr A*

Sgr A* was found as a compact radio source (Balick & Brown 1974). The motions of stars in the central part of our Galaxy indicate the presence of a supermassive black hole with a mass of about $4 \times 10^6 M_{\odot}$, coincident with Sgr A* (Eisenhauer et al. 2005; Ghez et al. 2005). In spite of the huge gravitational energy, the radiation is quite weak, particular in the X-ray band. The direct observation of Sgr A* in the X-ray band was first made with Chandra as shown in figure 2.1, which found that its quiescent luminosity is only $2 \times 10^{33} \text{ erg s}^{-1}$ (Baganoff et al. 2001). This luminosity is far fainter than that of a typical active galactic nucleus ($\sim 10^{41-46} \text{ erg s}^{-1}$). Flare activities with a duration time of 10 ks were also found (Baganoff et al. 2001; Goldwurm et al. 2003), but their amplitudes were just a factor of ten.

Observations with other wavelengths have been extensively done. Recently, the long-sought near-IR counterpart to Sgr A* was discovered (Genzel et al. 2003), and the point-like detection of TeV gamma ray source coincident within 1 arcmin of Sgr A* is reported (Aharonian et al. 2004; Tsuchiya et al. 2004; Kosack et al. 2004). The

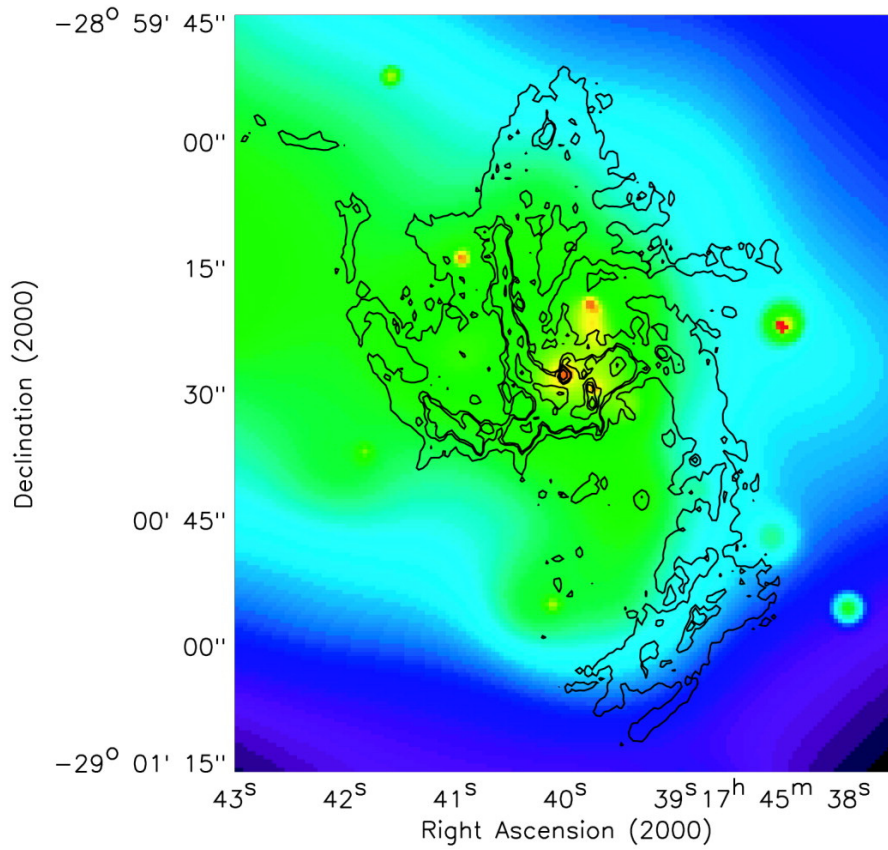


Figure 2.1: Adaptively smoothed 0.5–7.0 keV image of Sgr A* overlaid contours of VLA 6 cm (Baganoff et al. 2003).

wideband spectrum of Sgr A* is displayed in figure 2.2 (Yusef-Zadeh et al. 2006). A number of theoretical models are proposed to explain its faint quiescent luminosity (e.g., Liu et al. 2004; Yuan et al. 2004; Atoyan & Dermer 2004; Goldston et al. 2005; Markoff 2005; Eckart et al. 2006).

2.1.2 The Galactic Center Diffuse X-ray Emission

The Ginga X-ray satellite first detected the iron K-shell lines near the Galactic Center (Koyama et al. 1989, Yamauchi et al. 1990). The line energy is about 6.7 keV and the emission extends about 1° – 2° over the GC region, which is called as the Galactic Center Diffuse X-ray Emission (GCDX). ASCA resolved the iron K-shell line detected with Ginga into three distinct lines at 6.4, 6.7, and 6.9 keV (Koyama et al. 1996). The 6.7 and 6.9 keV lines are likely due to He-like (Fe XXV) and hydrogenic (Fe XXVI) ions of iron. With respect to the 6.7 keV and 6.9 keV lines, collisional excitation in optically-thin, high-temperature plasma, and charge exchange recombination are both considered. Suzaku obtained the global distribution of the 6.7 keV line emission shown in figure 2.3 and the GCDX spectrum with the highest quality determining the line centroid energy of Fe XXV within 1 eV (Koyama et al. 2007d). The line center energies and widths of Fe XXV $K\alpha$ and Fe XXVI $Ly\alpha$ favor a collisional excitation plasma for the origin of the GCDX. The electron temperature determined from the line flux ratio of Fe XXV $K\alpha$ / Fe XXV $K\beta$ is similar to the ionization temperature determined from that of Fe XXV $K\alpha$ / Fe XXVI $Ly\alpha$. Thus the GCDX plasma is close to ionization equilibrium. The temperature of the thin thermal plasma determined from the GCDX spectrum is ~ 10 keV. The total thermal energy is estimated to be 10^{53-54} erg, or equivalent to 10^2 – 10^3 supernovae explosions. The temperature of ~ 10 keV is higher than that bounded by the Galactic gravity, hence the plasma should escape from the GC region. The time scale estimated by the plasma size (1° or ~ 150 pc at 8.5 kpc) divided by the sound velocity of the ~ 10 keV plasma is $\sim 10^5$ years. Therefore the energy of $\sim 10^{53-54}$ erg should be supplied in the past $\sim 10^5$ years; 1 supernova every 100–1000 years is required in the GC region.

The 6.4 keV line is likely to be $K\alpha$ from the neutral and/or a blend of low charge states of iron (Fe I). In fact, the 6.4 keV line is localized near molecular clouds such as the radio complex Sgr B2 and the Radio Arc regions. Detailed descriptions about 6.4 keV are made in section 2.1.4.

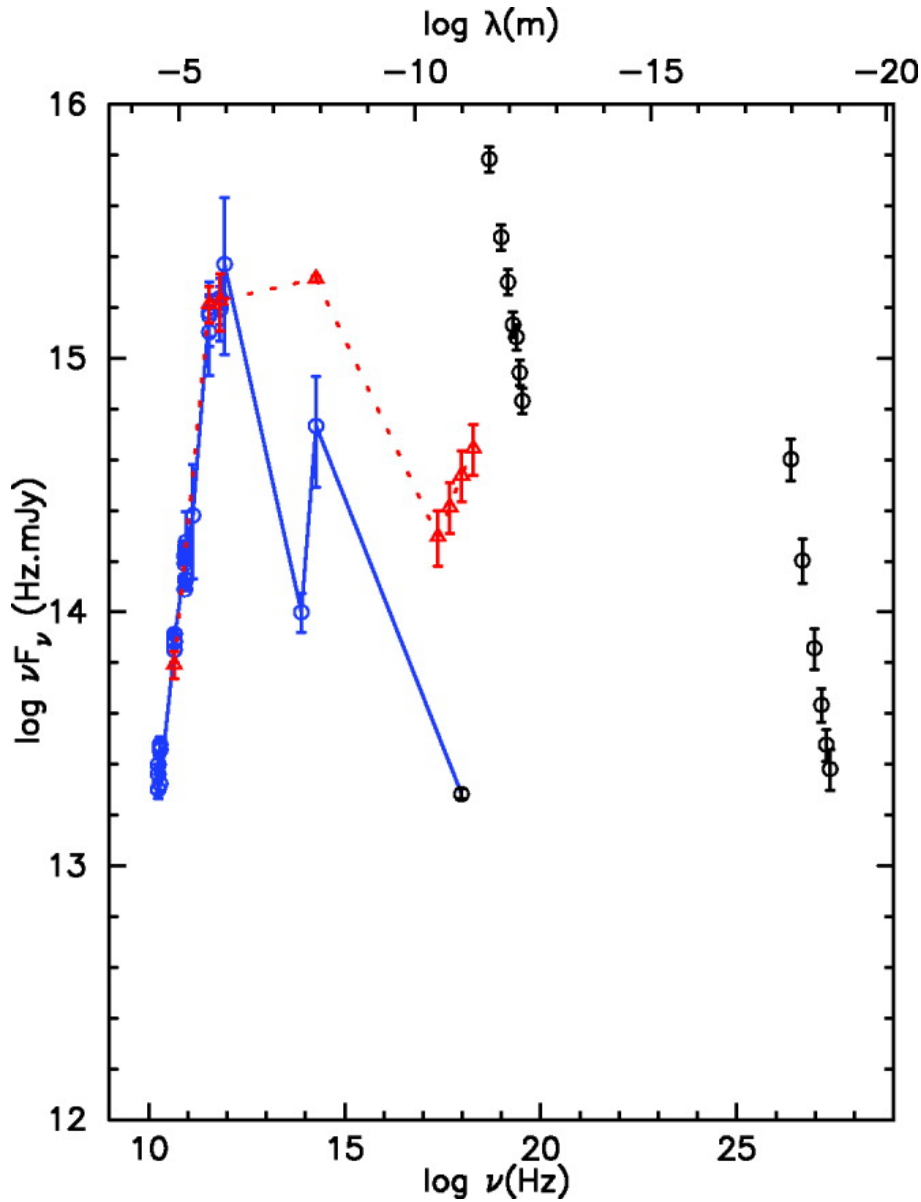


Figure 2.2: Wideband spectrum of Sgr A*. The spectrum of Sgr A* is based on measurements at 7 mm, 450 μm , 850 μm , 3.6 μm , 1.6 μm , and X-rays at 1 keV. The quiescent X-ray and near-IR fluxes are taken from Baganoff et al. (2001), Genzel et al. (2003), and Ghez et al. (2005). The quiescent flux is shown in blue color and the flux associated with flaring activity including the X-ray flare is shown in red color. The hard gamma ray emission from the Galactic center at 1 TeV based on HESS observations (Aharonian et al. 2004) and the high fluxes from INTEGRAL observations are not connected and are only shown by themselves in black. Further descriptions are shown in Yusef-Zadeh et al. (2006).

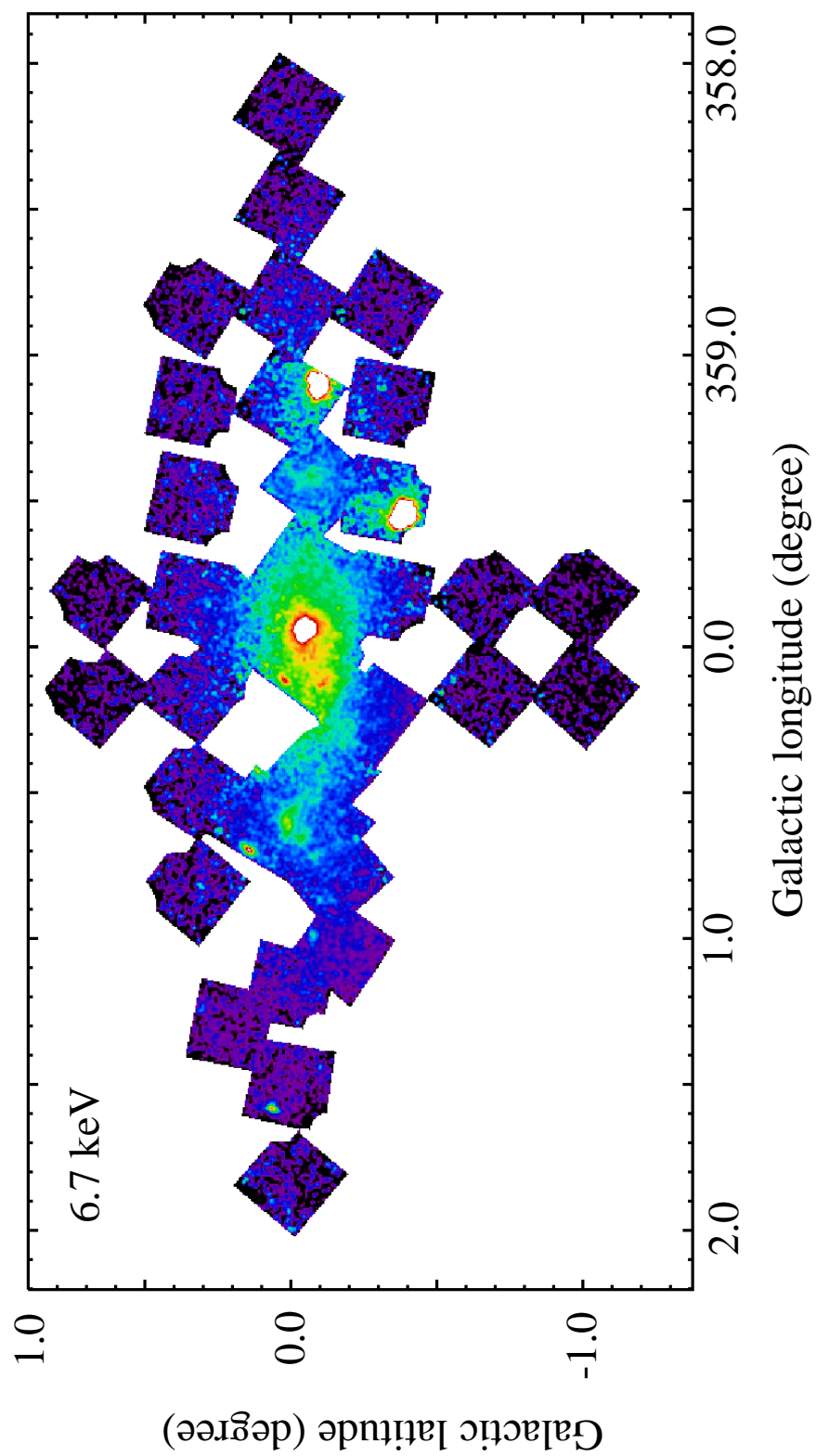


Figure 2.3: 6.7 keV narrow band image of the Galactic Center obtained with the Suzaku XIS.

2.1.3 Supernova Remnants

With radio studies of our Galaxy, over two hundred SNRs are known (Green 2004). Nine of them are located in the GC region (1° – 2°) and three of the SNRs associate X-ray emissions. These X-ray emissions are seen as globular diffuse morphologies while the radio ones are shell-like morphologies which are so called “Mixed-Morphology SNRs” (Rho & Petre 1998). One interpretation of the MM SNR is that a hot ($\sim 10^7$ K) central ejecta is seen with X-ray and cool ($\leq 10^6$ K) thermal shell are obscured with Galactic high density interstellar medium. The thermal plasma with a temperature of 1 keV exhibits a strong SXV $K\alpha$ (2.45 keV) line emission. Therefore the narrow line imaging of the SXV $K\alpha$ line is the best probe to search a Galactic SNR. The Suzaku satellite has observed many GC regions and composed the SXV $K\alpha$ line map (shown in figure 2.4). Some structures have been already reported as SNR sources (Koyama et al. 2007c; Nobukawa et al. 2008; Mori et al. 2008).

2.1.4 Giant Molecular Complexes

Cold molecular gas is strongly concentrated in the inner few hundred parsecs of the Galaxy. It seems to form a huge cloud complex with a size of $\Delta l \times \Delta b = 3^\circ \times 1^\circ$, which is called as the Galactic center molecular cloud complex. In the Galactic center molecular cloud complex, gas temperature is known to be relatively high (30–60 K) and roughly uniform over several hundred parsecs. The total molecular mass is $\geq 2 \times 10^7 M_\odot$ (Oka et al. 1998).

Figure 2.5 shows the spatial distribution of dense molecular clouds in the Galactic center region with velocity-integrated CS $J=1-0$ emission in the range $v=-200$ to 200 km s^{-1} , which corresponds to the central molecular zone (CMZ) (Morris & Serabyn 1996). The molecular clouds, which consist of long and curved streams mainly along the Galactic plane, are roughly associated with strong continuum sources, the Sgr A radio arc complex, Sgr B, Sgr C, and Sgr D.

Although these molecular clouds are so cool that they cannot emit X-ray photons themselves, 6.4 keV neutral iron line (FeI) emissions were found (Koyama et al. 1996). Figure 2.6 is the Suzaku view of the GC region in the 6.4 keV band. The X-ray emissions show clumpy structure associating some molecular cloud complexes. They need external sources, such as X-rays or particles, to cause inner-shell ionizations. Further details of Sgr B and the emission mechanism of neutral lines, the main theme of this thesis, are described in the following sections.

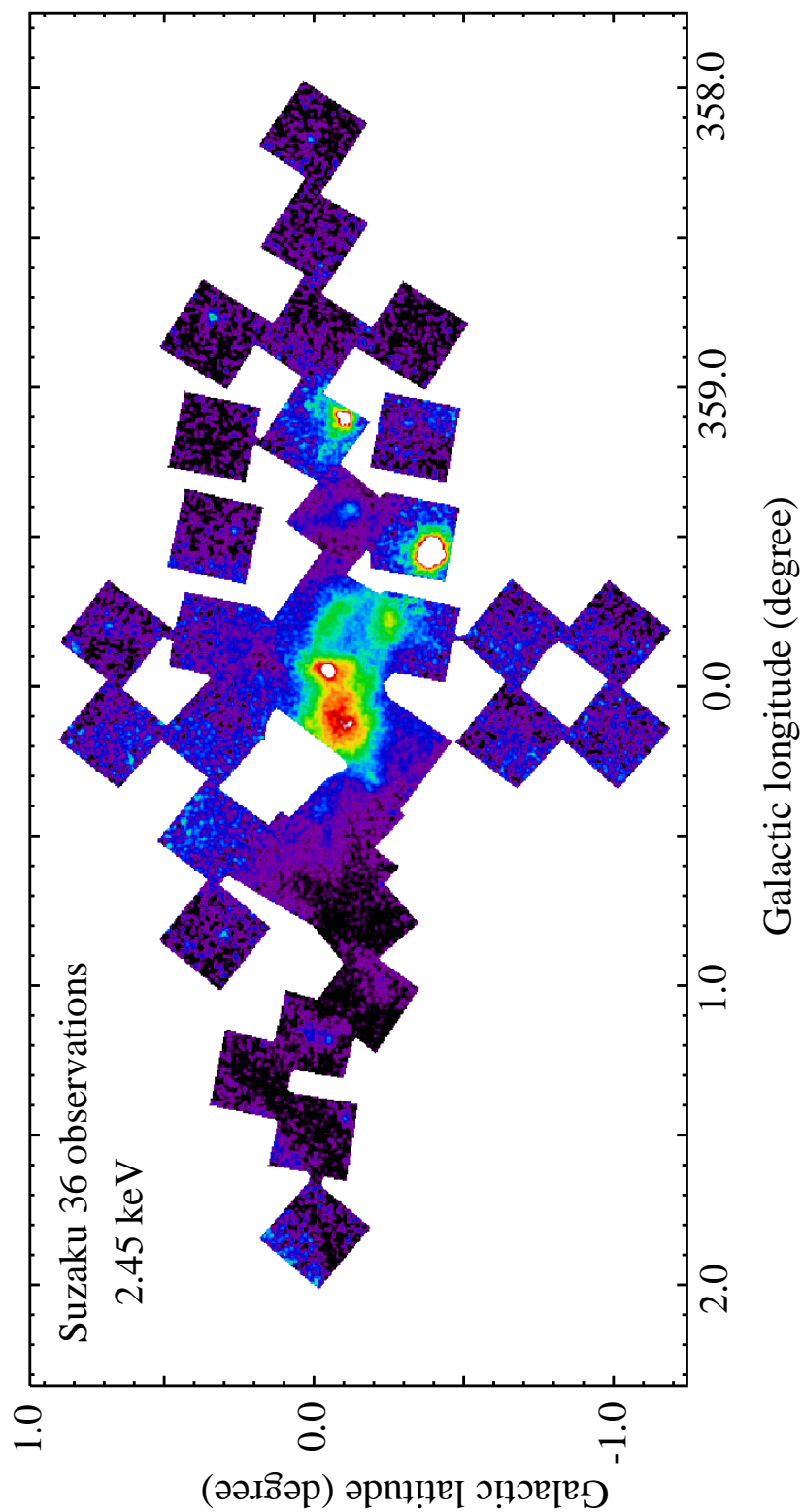


Figure 2.4: 2.45 keV narrow band image of the Galactic Center obtained with the Suzaku XIS.

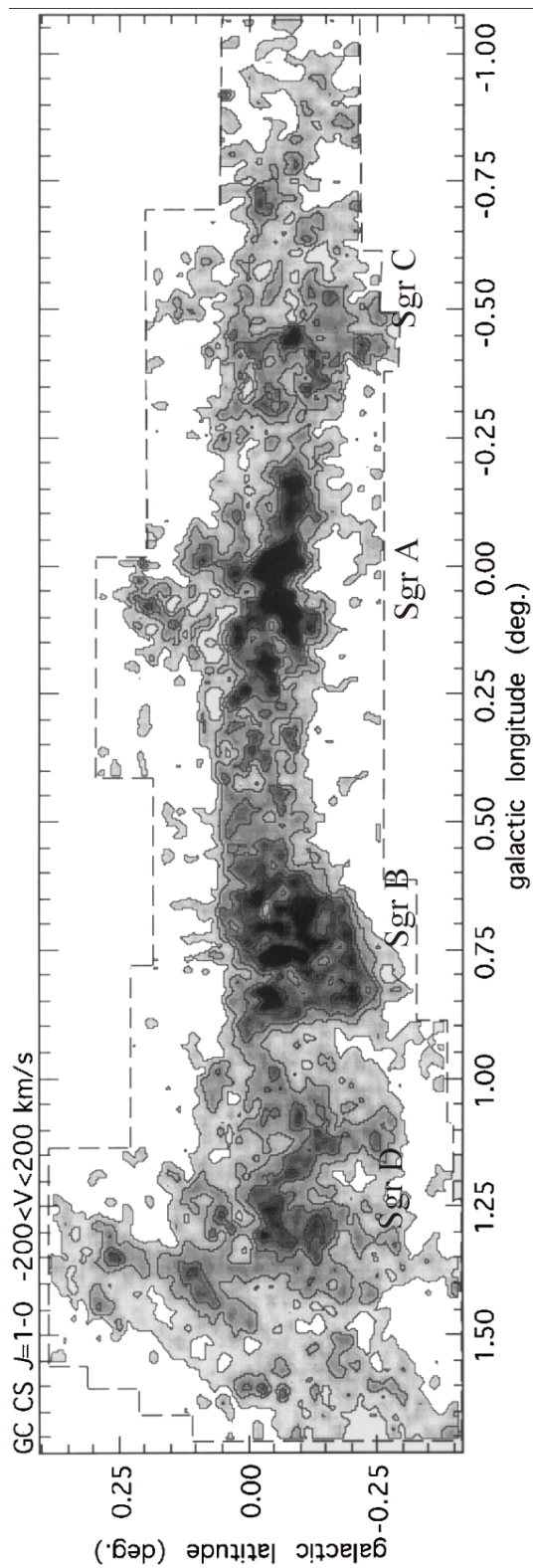


Figure 2.5: Velocity-integrated CS $J=1-0$ emission in the Galactic center region (Tsuboi et al. 1999). The velocity integrated range is from -200 to 200 km s^{-1} .

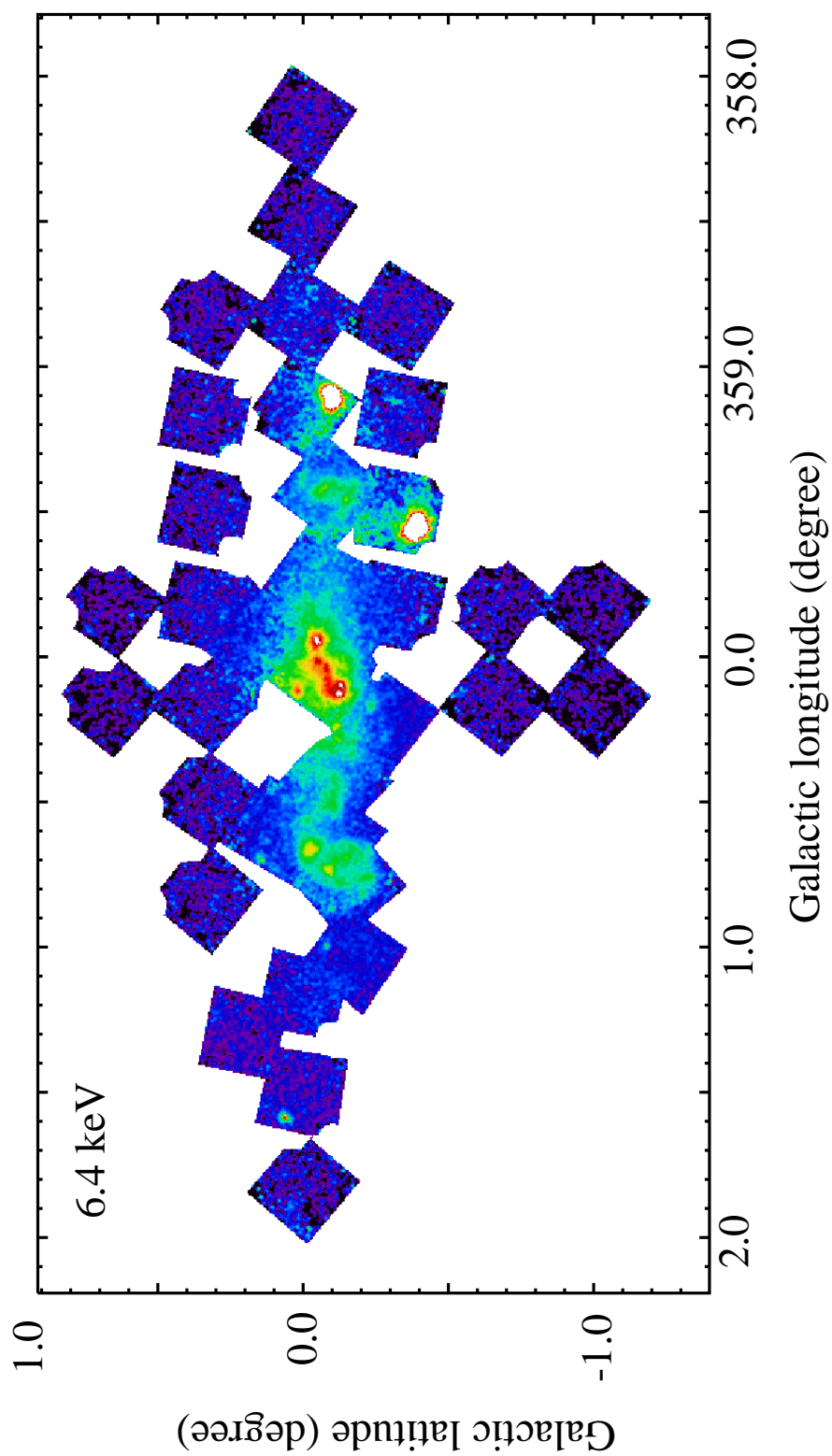


Figure 2.6: 6.4 keV narrow band image of the Galactic Center with the Suzaku XIS.

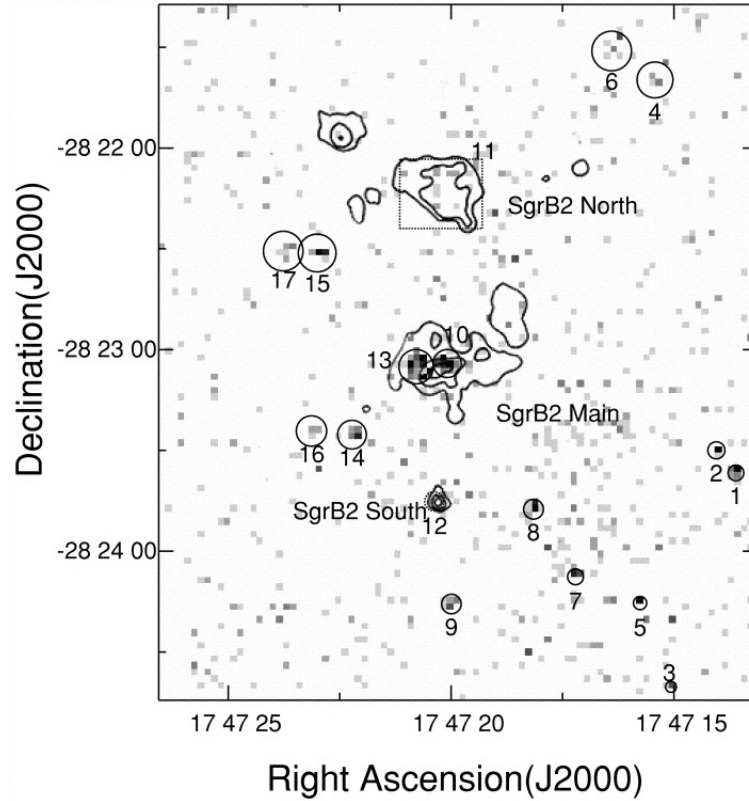


Figure 2.7: 2–10 keV band image of Sgr B2 obtained with the Chandra ACIS (Takagi et al. 2002), overlaid on contours of H II regions (Gaume et al. 1995). The solid circles indicate X-ray point sources.

2.2 A Giant Molecular Complex — Sgr B

Sgr B is one of a number of Giant Molecular Complexes (GMCs) bound in relatively tight orbits at a projected distance of ~ 100 pc around Sgr A*. The total mass is $0.4\text{--}1.0 \times 10^7 M_{\odot}$ (Tsuboi et al. 1999). The Sgr B complex contains two bright subregions, Sgr B1 and Sgr B2, which were named in radio continuum observations (Mehringer et al. 1995).

2.2.1 Sgr B2

Sgr B2 is the largest molecular cloud in the Galaxy and contains one of its largest complexes of H II regions, being dominated by numerous ultracompact and hypercompact H II regions which inhabit three dense cores (labeled "north", "main", and "south"). These are, themselves, located inside a structure labeled "the Envelope" (Gordon et al. 1993). The cores are small (0.5 pc), light ($10^3\text{--}10^4 M_{\odot}$; correspond-

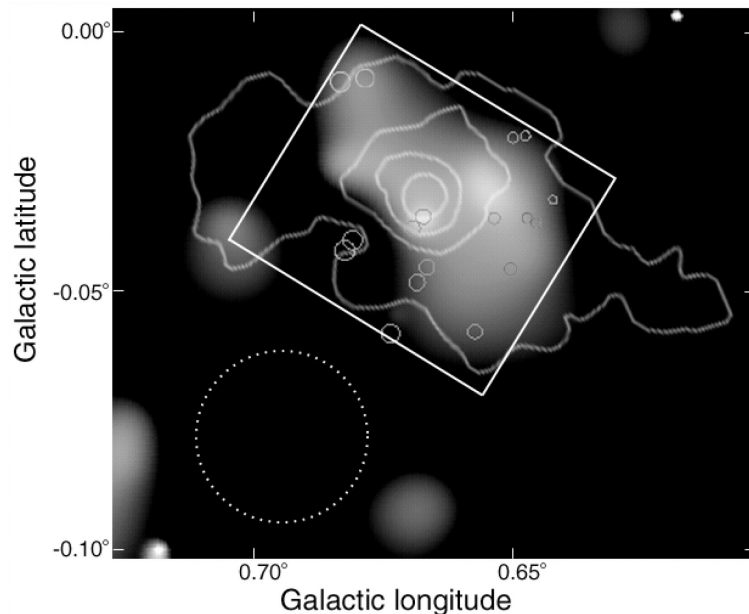


Figure 2.8: Adaptively smoothed Chandra image in the 6.15–6.55 keV band (Murakami et al. 2001), overlaid on contours of ^{13}CO line flux (Sato et al. 2000)

ing to 5% of the Sgr B2 mass), and dense (10^6 – 10^7 cm^{-3}). On the other hand, the Envelope is massive ($7.6 \times 10^5 M_{\odot}$), and less dense (10^5 cm^{-3}). The average hydrogen density across Sgr B2 is 10^6 cm^{-3} . There have been many ultracompact (UC) H II sources identified in the Sgr B2 main alone (Gaume et al. 1995). Takagi et al. (2002) have discovered many compact X-ray sources in the cloud center with Chandra and the X-ray fluxes and spectra indicate that these are likely high mass young stellar objects.

Sgr B2 is also a strong 6.4 keV line source. ASCA first discovered the 6.4 keV line emission with a strong Fe K absorption edge (Koyama et al. 1996), and Chandra has resolved its morphology (figure 2.8, Murakami et al. 2001). The equivalent width of this line is about 1–2 keV and the depth of the absorption edge is equivalent to $N_{\text{H}} \sim 10^{24}$ cm^{-2} . The X-ray morphology is a concave shape at the GC side. With these observational facts, they proposed that Sgr B2 is an X-ray reflection nebula (XRN) irradiated by the GC source Sgr A*, which was thought to be X-ray bright about 300 years ago, the light traveling time between Sgr B2 and Sgr A*. On the other hand, the counter scenario is proposed in Yusef-Zadeh et al. (2007). The nonthermal electrons cause the 6.4 keV line emission by colliding with ambient matter to produce the inner-shell ionizations of iron atoms. The determination of the 6.4 keV line origin is one of the main theme of this thesis.

2.2.2 Sgr B1

Sgr B1 is comparatively less studied than Sgr B2. It is an H II region of optical depth much less than cm wavelengths, suggesting that it is an older, evolved structure no longer containing the dense, hot star forming UC H II regions found in Sgr B2 (Mehringer et al. 1995). In the recent study with the Suzaku satellite, two diffuse sources are found (Nobukawa et al. 2008). G 0.42–0.04 is a candidate for a supernova remnant which exhibits a strong SXV $K\alpha$ emission line. M 0.51–0.10 has a prominent Fe I $K\alpha$ emission line and a strongly absorbed continuum which is similar to the X-ray spectrum of Sgr B2.

2.3 X-ray Emission Processes from Neutral Elements

Here we review the X-ray line emission processes from neutral elements, largely owing to Inoue (1985) and Tatischeff (2003). We introduce three processes to cause inner-shell ionization; X-ray photoionization and collisional ionization by electrons and by ions.

2.3.1 Photoionization

Figure 2.9a shows a compilation of cross sections for K-shell ionization. The photoionization cross sections are step functions of energy varying approximately as E_X^{-3} from ionization thresholds. Inoue (1985) operated a numerical simulation of the fluorescence iron line emission from neutral matter. The incident X-rays which have a spectrum with an index of 1.1 invoke the K-shell ionization of iron and produce the Fe K line and the continuum emission by Thomson scattering. Figure 2.10 shows the expected equivalent width of the Fe K line as a function of the thickness of the matter N_H . The line I represents the fluorescence efficiency for the incident X-rays. The efficiency first increases with the thickness N_H of the gas but turns to decrease due to the absorption of the line photons in a certain N_H . The line II indicates the equivalent width for the continuum including the absorption of the incident X-rays and the scattered component and the line III only considers only the scattered continuum.

2.3.2 Collisional Ionization by Electrons

The cross sections for the collisional ionization, shown in figure 2.9a, have a much weaker energy dependence than that for photoionization, in particular, arise in the

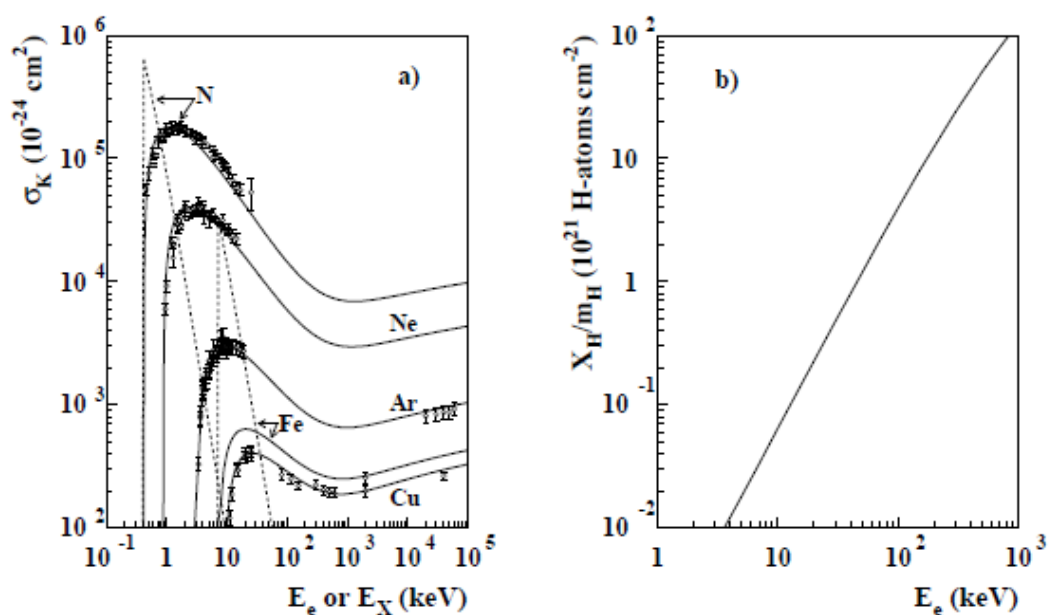


Figure 2.9: (a) Cross sections for K-shell ionization of various atoms. Solid curves indicate the calculated result by electron impacts from the semi-empirical formula. Dashed curves indicate cross sections for K-shell photoionization of N and Fe. (b) Stopping range of low-energy electrons in hydrogen. See Tatischeff (2003) for detail descriptions.

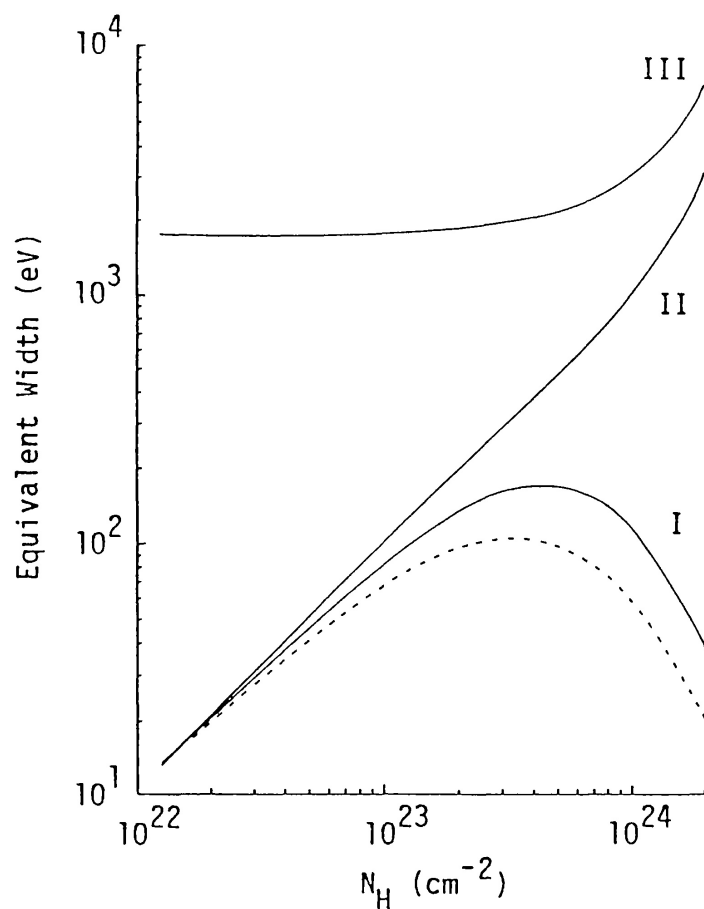


Figure 2.10: Simulated equivalent width of fluorescent Fe K line as a function of the thickness N_H of scattering matter. The simulation is made in the following cases; I: primary source is directly observed, II: X-rays from primary source are absorbed by a surrounding matter, III: primary source is totally hidden or scattering matter is irradiated by an external source.

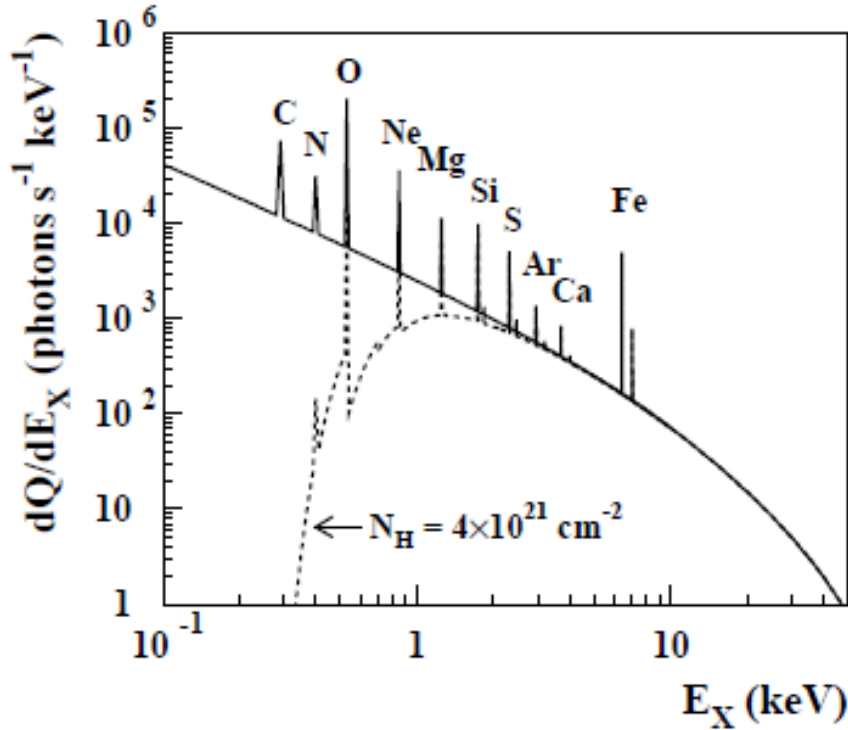


Figure 2.11: X-ray emission produced by suprathermal electrons with the source spectrum of $\propto E_e^{-2}$ interacting in a thick target composed of a neutral atomic gas of the solar abundance. The dashed line shows the effect of photoelectric absorption, with a H column density of $4 \times 10^{21} \text{ cm}^{-2}$.

MeV region caused by relativistic effects (e.g. Hoffmann et al. 1979). The most efficient energy for an interaction of iron is 10–100 keV. Figure 2.9b shows the stopping range of low-energy electrons in a neutral H gas. Suprathermal electrons with an energy of 10–100 keV would stop in a neutral atomic gas of solar composition with a thickness of $4 \times 10^{21} \text{ cm}^{-2}$. Taking these basic configurations into account, Tatischeff (2003) calculated the spectrum (shown in figure 2.11) for suprathermal electrons with an index of 2. The equivalent width of $K\alpha$ lines from O, Ne, Si and Fe is 355, 107, 73 and 290 eV, respectively. A significant line emission from elements of relatively low atomic number could allow to distinguish X-ray line production by suprathermal electrons from fluorescence emission, since the strong decrease of the fluorescence yields with decreasing atomic number z is compensated by the approximate $z^{-4.3}$ dependence of the K-shell ionization cross section for electrons while $z^{-2.3}$ for photons (figure 2.9a).

2.3.3 Collisional Ionization by Fast Ions

Tatischeff (2003) also calculated an X-ray spectrum from accelerated ion interactions shown in figure 2.12. The energetic particles are assumed to be the same composition as the Galactic cosmic-ray ions. In this calculation, photoelectric absorption in the ambient medium is not taken into account for both clarity and simplicity.

The narrow lines are due to K-shell vacancy production in the ambient atoms by the fast ions. In comparison with the similar lines produced by photoionization or by electron impact, the lines produced by heavy ion collisions could be shifted by several tens of electron-volts, significantly broadened and split up into several components, owing to multiple simultaneous ionizations (Garcia et al. 1973), which is not taken into account in the calculation shown in figure 2.12. For example, the neutral Fe $K\alpha$ line produced by 1.9 MeV/nucleon O impacts is blueshifted by ~ 50 eV in comparison with that produced by proton impacts, and has a width of ~ 100 eV (FWHM). The prominent, broad line features in figure 2.12 are due to atomic de-excitations in the fast ions following electron capture by charge-transfer reactions and collisional excitation.

Continuum X-rays are essentially produced by inverse bremsstrahlung (IB), which is the kinematic inverse of normal bremsstrahlung, i.e. the radiation of an electron at rest in the moving Coulomb field of a fast ion. Thus, for nonrelativistic protons of kinetic energy E_p interacting in stationary H, the inverse bremsstrahlung cross section is almost identical to the bremsstrahlung cross section for electrons of energy $(m_e/m_p)E_p$ also interacting in stationary H. The recent study in shocked astrophysical plasmas shows that IB from accelerated ions is generally expected to be much lower than bremsstrahlung from suprathermal electrons. There are the other two continuum emission from the radiative recombinations of ambient electrons to the K-shell of the fast ions (RRC; Dogiel et al. 1998) and from the secondary, knocked-on electrons that subsequently produce bremsstrahlung by interacting with the ambient atoms (SEB). These two emissions should generally be dominated by the IB production.

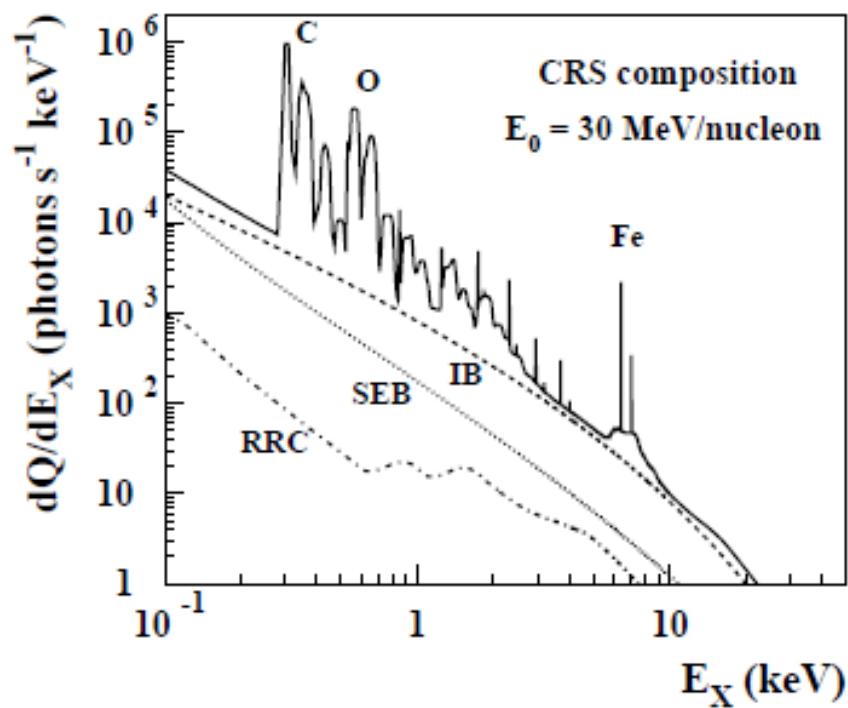


Figure 2.12: X-ray emission produced by fast ions with cosmic-ray source (CRS) composition. IB: inverse bremsstrahlung; SEB: secondary electron bremsstrahlung; RRC: radiative recombination continuum. See Tatischeff (2003) for detailed descriptions.

Chapter 3

Instruments

In this study, the X-ray detector with the sufficient energy resolution to resolve the Fe K lines and the spatial resolution to distinguish diffuse sources with a scale of an arcsecond is necessary. A Charge-Coupled Device (CCD) is the most powerful imaging device for the present X-ray astronomy with the energy resolution of ~ 130 eV at 5.9 keV (FWHM), and sufficient detection efficiency in the 0.1–10 keV band. Thus, the X-ray CCD detectors are the most suitable devices for this study.

We use observation data from four X-ray satellites boarding the CCD cameras, ASCA, Chandra, XMM-Newton and Suzaku. We introduce these space observatories in the point of the efficiency of their mirrors, the space environments, and the backgrounds of the CCD cameras.

3.1 X-ray Satellites and their Mirrors

The characteristics of four satellites are different among each other, which specify imaging or spectroscopy reflecting on the X-ray mirror system. Figure 3.1 is schematic views of the four X-ray observatories, ASCA, Chandra, XMM-Newton and Suzaku. The typical properties of their spacecrafts and mirrors are listed in table 3.1.

3.1.1 ASCA

The Advanced Satellite for Cosmology and Astrophysics, ASCA, is the Japanese fourth X-ray satellite launched on February 20th, 1993 (Tanaka et al. 1994). The orbital heights at perigee and apogee are about 520 km and 620 km, respectively, whereas the inclination is 31.1° . The orbital period is approximately 96 minutes. The satellite re-entered into the atmosphere on March 2, 2000. ASCA has four identical X-ray telescope with nested thin foil mirrors (XRT; Serlemitsos et al. 1995). The

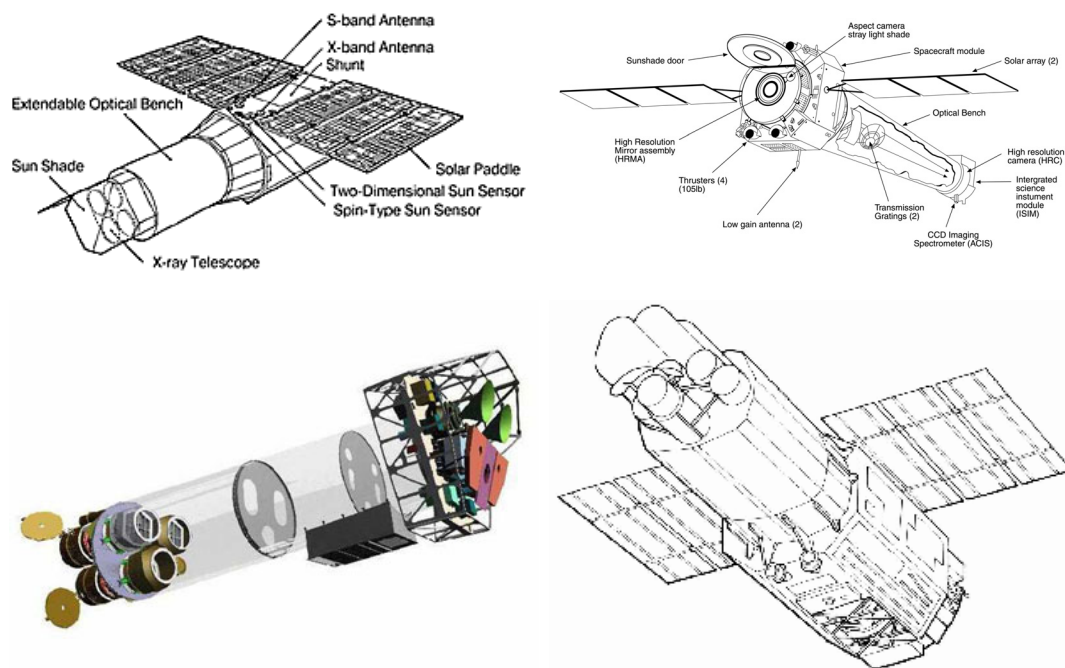


Figure 3.1: Schematic pictures of the ASCA (upper left), Chandra (upper right), XMM-Newton (lower left) and Suzaku satellites (lower right).

Table 3.1: Comparison of X-ray telescopes

Observatory	ASCA	Chandra	XMM-Newton	Suzaku
Country	Japan	USA	ESA	Japan
Year	1993–2000	1999–	1999–	2005–
Orbit [km]	520–620	16,000–133,000	7,000–114,000	568
Orbital period	96 mins	48 hrs	64 hrs	96 mins
Mirror system	XRT	HRMA	—	XRT
Focal length [m]	3.5	10	7.5	4.75
Effective area@1 keV [cm ²]	325 × 4	800 × 1	1500 × 3	450 × 4
Field of view	24′	30′	30′	17′
Angular Resolution	2′9	0′′5	15′′	2′

focal-plane instruments consist of two kinds of detectors: two CCD cameras and two gas counters. The former are called Solid-state Imaging Spectrometers (SISs: Burke et al. 1994), and the latter are called Gas Imaging Spectrometers (GISs: Ohashi et al. 1996; Makishima et al. 1996).

The XRT of ASCA utilizes total X-ray reflection under the Wolter type I configuration, which employs paraboloid and hyperboloid surfaces as the primary and the secondary mirrors. The basic design of the telescope approximates the conventional optical paired hyperbolic and parabolic surfaces with conical surfaces realised as a set of closely nested concentric thin foils (120 per telescope) held together in quadrants by metal fittings. The foils are made of aluminium and coated with 10 to 20 microns of acrylic and 60 nm of gold, which provided the reflecting surface. Although the use of foils, which cannot be smoothed by polishing, reduces the sharpness of the image compared with conventional X-ray optics, it does provide a larger collecting area and broader pass band. The angular resolution is so poor as ~ 3 arcmin due to the shape errors of the mirror surfaces. The effective area of XRT is shown in figure 3.2.

3.1.2 Chandra

Chandra (Weisskopf et al. 2003) was launched on the Space Shuttle Columbia on July 23, 1999. The orbit of the satellite is elliptical with the perogee altitude of 16,000 km, and the apogee altitude of 133,000 km. The orbital period is about 64 hours, which is allowing uninterrupted observing intervals of more than 48 hours.

The most vivid characteristic of Chandra is the highest angular resolution in all the previous X-ray satellites. The Chandra telescope, “High Resolution Mirror Assembly (HRMA)”, consists of four mirrors of Wolter type I geometry formed by glass, and achieved the angular resolution of $0''.5$. The mirrors are coated with iridium on a binding layer of chromium. In order to keep high accuracy of the mirror surface, the glass is very thick and heavy with the total mass of about 1,500 kg.

Chandra has two X-ray detectors on the focal plane: the Advanced CCD Imaging Spectrometer (ACIS) and the High Resolution Camera (HRC). The HRC is a multiple-channel plate optimized for imaging without the ability of spectroscopy. Chandra can operate two types of grating: the High-Energy Transmission Grating (HETG) and the Low-Energy Transmission Grating (LETG).

The HRMA, shown schematically in figure 3.3, contains the nested mirrors, center, forward and aft aperture plates, baffles, inner and outer cylinders, mounts, pre- and post-collimators, fiducial light transfer components, mirror support sleeves, for-

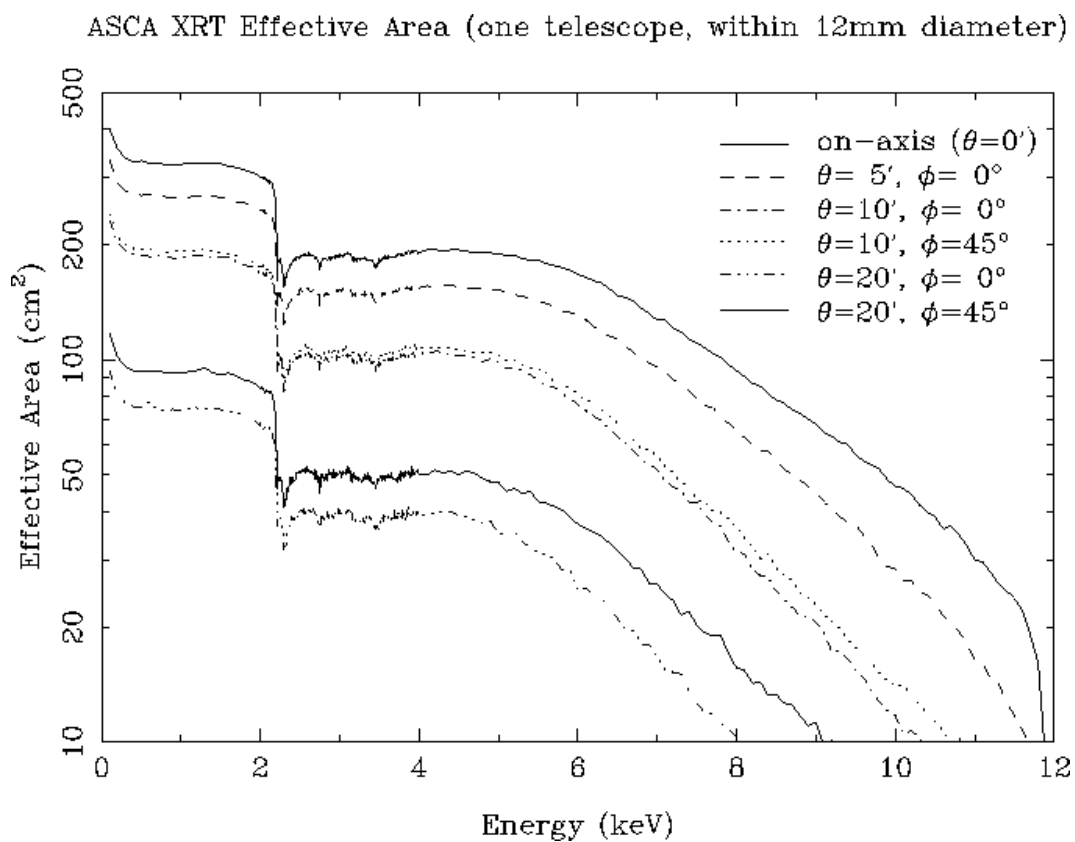


Figure 3.2: ASCA XRT effective area (one telescope) for different off-axis angle (θ) and azimuthal angle (ϕ). See http://heasarc.gsfc.nasa.gov/docs/asca/asca_nra06/appendix_e/appendix_e.html.

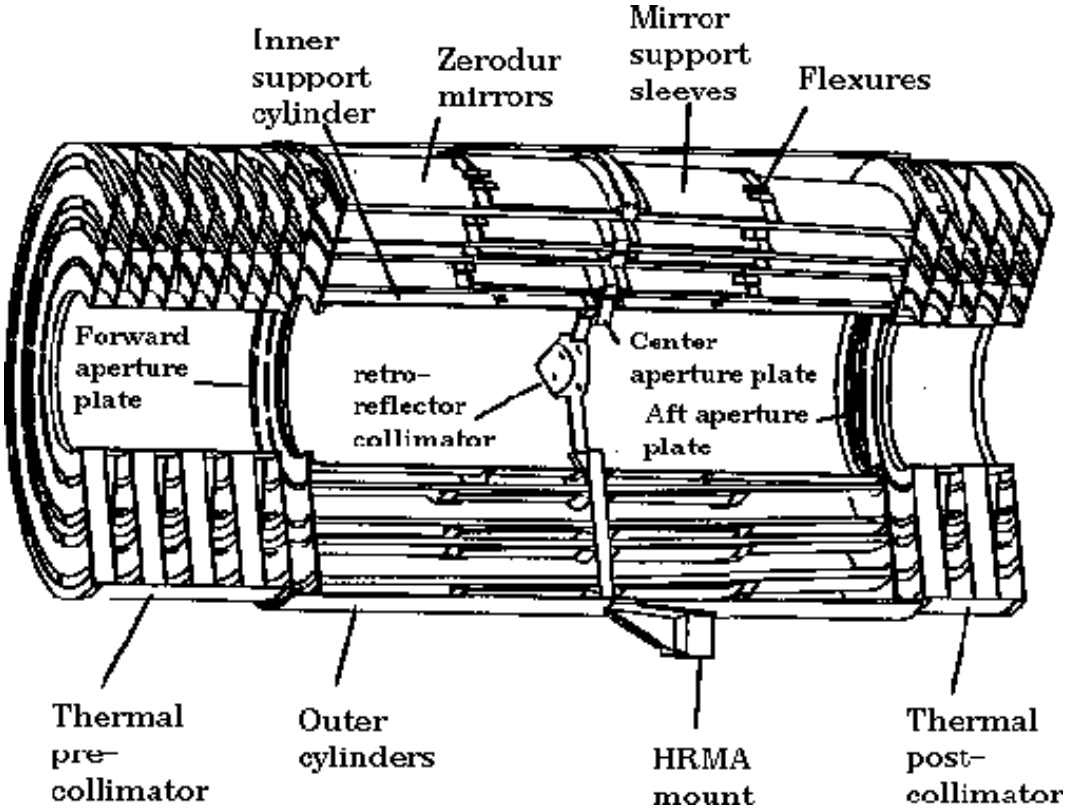


Figure 3.3: The four nested HRMA mirror pairs and associated structures. See <http://exc.harvard.edu/proposer/POG/html/HRMA.html>.

ward and aft contamination covers, flux contamination monitors, and thermal control hardware. The outer mirror pair is number 1, and, progressing inwards, 3, 4, and 6. The original design had six mirror pairs; numbers 2 and 5 were eliminated. The pair diameters range from about 0.65 to 1.23 meters. The distance from the center of the Central Aperture Plate (CAP) separating the paraboloid and hyperboloid mirrors to the HRMA focus is 10.0548 meters, with each mirror pair varying slightly about this value. Note that this distance is close to, but not exactly, the focal length. An annular on-axis beam enters each mirror pair, is reflected from paraboloids and hyperboloids and exits to converge to a focus.

Figure 3.4 shows the HRMA effective areas with focal plane detectors as a function of X-ray energy. The structure near 2 keV is due to the iridium M-edge.

3.1.3 XMM-Newton

XMM-Newton is a ESA's X-ray observatory launched on December 10th, 1999. It carries two distinct types of telescopes: three X-ray telescopes with different X-ray detectors in their foci, and a 30-cm optical/UV telescope with a microchannel-plate preamplified CCD detector in its focal plane. XMM-Newton provides three scientific instruments: European Photon Imaging Camera (EPIC) comprised of three X-ray CCD detectors, Reflection Grating Spectrometer (RGS) with high resolution X-ray spectroscopy and Optical Monitor (OM).

Each of the three X-ray telescopes on board XMM-Newton consists of 58 Wolter I grazing-incidence mirrors which are nested in a coaxial and cofocal configuration. The design of the optics was driven by the requirement of obtaining the highest possible effective area over a wide range of energies, with particular emphasis in the region around 7 keV. Thus, the mirror system had to utilize a very shallow grazing angle of $30'$ in order to provide sufficient reflectivity at high energies. The focal length of the telescopes is 7.5 meters and the diameter of the largest mirrors is 70 cm, to be compatible with the shroud of the launcher. Each telescope includes, apart from the mirror modules, baffles for visible and X-ray stray-light suppression and an electron deflector for diverting soft electrons. Figure 3.5 shows the effective area of all XMM-Newton X-ray telescopes, EPIC and RGS. The XMM-Newton mirrors are most efficient in the energy range from 0.1 to 10 keV, with a maximum at about 5 keV and a pronounced edge near 2 keV (Au M edge).

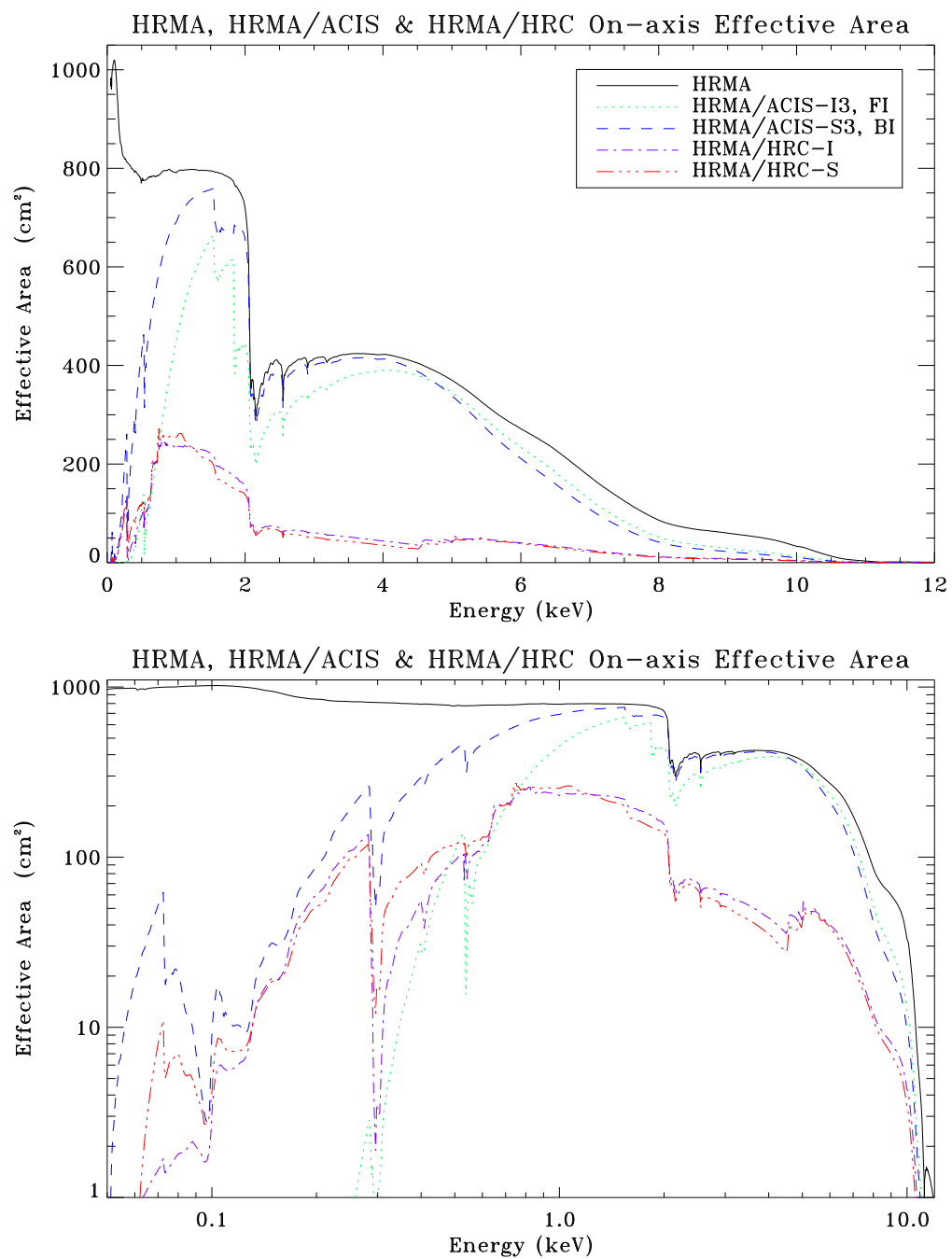


Figure 3.4: The HRMA/ACIS and HRMA/HRC effective areas versus X-ray energy in linear (top) and log (bottom) scale. See <http://cxc.harvard.edu/proposer/POG/html/HRMA.html> for details.

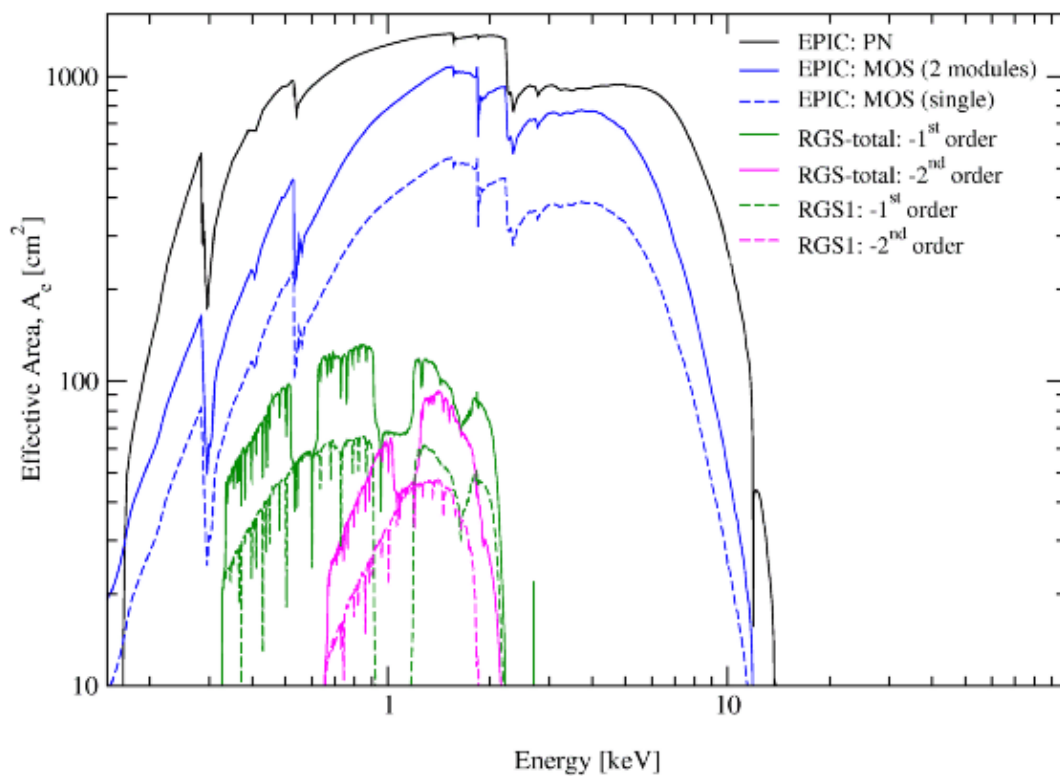


Figure 3.5: The net effective area of all XMM-Newton X-ray telescopes, EPIC and RGS. See http://xmm.vilspa.esa.es/external/xmm_user_support/documentation/uhb_2.5/node20.html.

3.1.4 Suzaku

Suzaku is the fifth Japanese X-ray astronomy satellite. It was developed under Japan-US international collaboration and was launched on July 10, 2005, from JAXA Uchinoura Space Center. The scientific payload of Suzaku initially consisted of three distinct co-aligned scientific instruments. Suzaku is in many ways similar to ASCA in terms of orbit, pointing, and tracking capabilities. As a result, the operational constraints for Suzaku are also similar to those of ASCA. Suzaku is placed in a near-circular orbit with an apogee of 568 km, an inclination of 31.9° , and an orbital period of about 96 minutes. The maximum slew rate of the spacecraft is 6 degrees/min, and settling to the final attitude takes ~ 10 minutes, using the star trackers. The normal mode of operations will have the spacecraft pointing in a single direction for at least 1/4 day. With this constraint, most targets will be occulted by the Earth for about one third of each orbit, but some objects near the orbital poles can be observed nearly continuously. The observing efficiency of the satellite as measured after a year of operation is about 45%.

There are four X-ray sensitive imaging CCD cameras (X-ray Imaging Spectrometers; XISs), three front-illuminated (FI; energy range 0.4–12 keV) and one back-illuminated (BI; energy range 0.2–12 keV), capable of moderate energy resolution. Each XIS is located in the focal plane of a dedicated X-ray telescope (XRT). The second instrument is the non-imaging, collimated Hard X-ray Detector (HXD), which extends the bandpass of the observatory to much higher energies with its 10–600 keV bandpass. Since, a thermal short between the helium and neon tanks resulted in the liquid helium coolant venting to space, which was happened on August 8, 2005, the high resolution spectrometer, the X-Ray Spectrometer (XRS), is no longer operational.

The Suzaku XRTs consist of closely nested thin-foil reflectors, reflecting X-ray at small grazing angles. An XRT is a cylindrical structure, having the following layered components: 1. a thermal shield at the entrance aperture to help maintain a uniform temperature; 2. a pre-collimator mounted on metal rings for stray light elimination; 3. a primary stage for the first X-ray reflection; 4. a secondary stage for the second X-ray reflection; 5. a base ring for structural integrity and interface with the EOB of the spacecraft. All these components, except the base rings, are constructed in 90° segments. Four of these quadrants are coupled together by interconnect-couplers and also by the top and base rings. The telescope housings are made of aluminum for an optimal strength to mass ratio. Each reflector consists of a substrate also made of aluminum and an epoxy layer that couples the reflecting gold surface to the substrate.

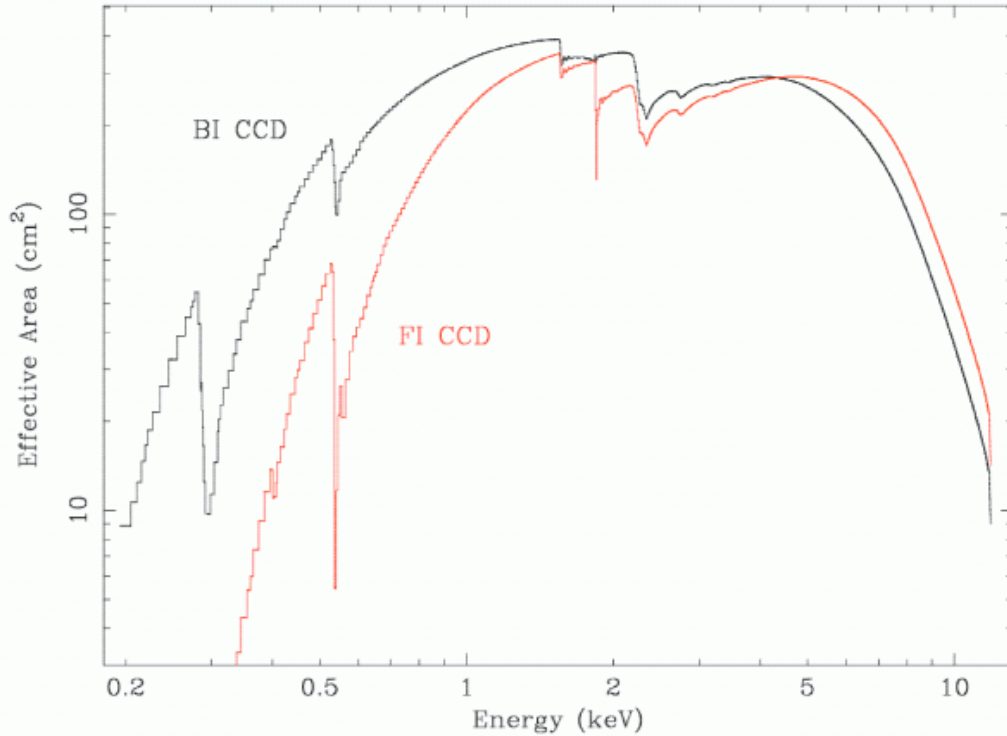


Figure 3.6: Effective area of one XRT + XIS system, for both the FI and BI chips. (No contamination included)

Including the alignment bars, collimating pieces, screws and washers, couplers, retaining plates, housing panels and rings, each XRT-I consists of over 4112 mechanically separated parts. In total, nearly 7000 qualified reflectors were used and over 1 million cm^2 of gold surface was coated.

Each of the co-aligned XRTs features an X-ray mirror with an angular resolution of $\sim 2'$ (HPD). Figure 3.6 shows the total effective area of the XIS+XRT, which includes features due to the elemental composition of the XIS and XRT. K-shell absorption edges from the oxygen (0.54 keV) and aluminum (1.56 keV) in the blocking filters are present, as well as a number of weak M-shell features between 2–3 keV arising from the gold in the XRT.

3.2 CCD cameras

Table 3.2 shows typical parameters of the CCD cameras onboard ASCA, Chandra, XMM-Newton and Suzaku.

Every CCD initially had a good energy resolution of ~ 130 eV. However, Charge

Table 3.2: Comparison of X-ray CCDs

Observatory	ASCA	Chandra	XMM-Newton		Suzaku
Country	Japan	USA	ESA		Japan
Year	1993–2000	1999–	1999–		2005–
Detector	SIS	ACIS	MOS	PN	XIS
No. of chips	8	8 (FI) / 2 (BI)	7	12	3 (FI) / 1 (BI)
No. of pixels/chip	420×420	1024×1024	600×600	378×64	1024×1024
Pixel size [μm]	27	24	40	150	24
Depletion depth [μm]	35	70	35	280	70(FI) / 45(BI)
Readout noise [e^-]	4–6	2	—	—	2

transfer efficiency (CTE), a measure of how effectively the CCD transfers the charge from one pixel to the next, gradually decreases due to the radiation damage in space. The decrease of the CTE, or in other words, the increase of the charge transfer inefficiency (CTI), causes the loss of charge during the charge transfer. This reduces the apparent X-ray energy and hence brings about a reduction of gain. Although the gain can be recovered by the measurement of the CTI, the energy resolution remains degraded.

Another problem in space is a background. The in-flight background spectrum of a CCD depends on the readout electronics in the soft band and the particle environment in the high energy bands. The particle environments depend on the orbits of the satellites. We describe the details in the following.

3.2.1 SIS

The SIS (Burke et al. 1994) is the first satellite-borne X-ray experiment that utilizes CCDs in the photon counting mode. Designed focal plane and configuration of the SIS are shown in figure 3.8.

Energy resolution

Figure 3.9 shows the energy resolution of SIS and GIS. The energy resolution of SIS is degraded because of the increase of the CTI. Additionally, the residual dark distribution (RDD) effect caused additional degradation of the spectral response. CCDs always have read-out noise: pixels without photon or particle events will have a mean of "dark level" and some distribution around this mean level. This is usually

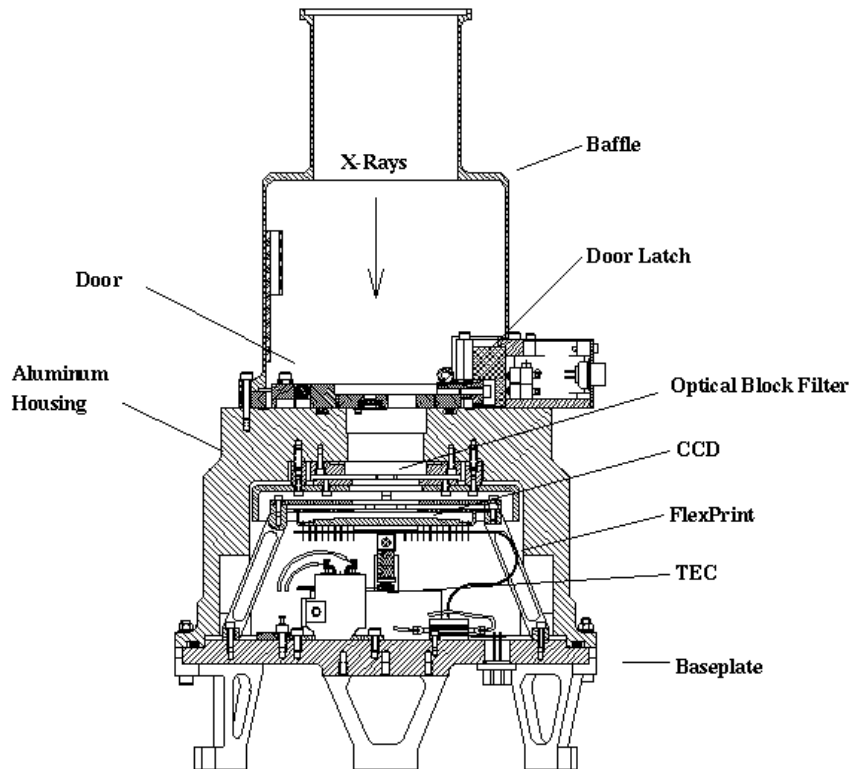


Figure 3.7: Cross section of SIS (Gendreau 1995).

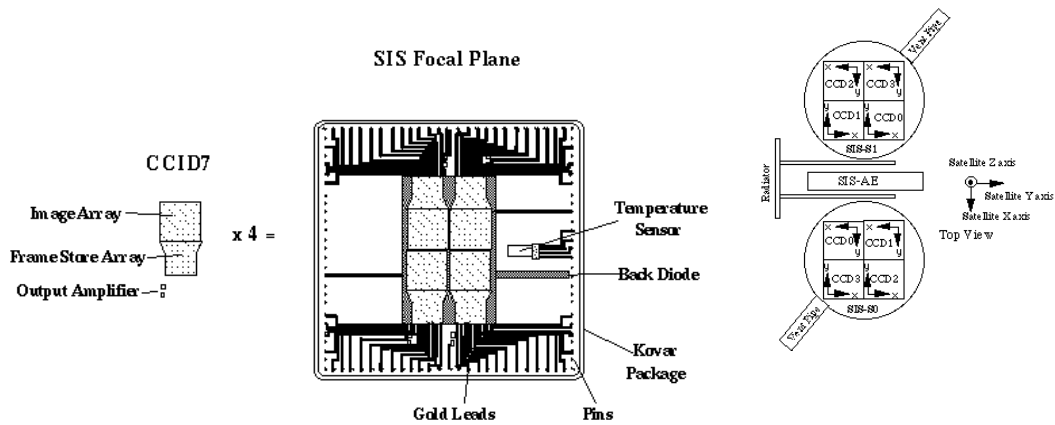


Figure 3.8: Left: Four individual CCDs are combined in a single package to make a single SIS focal plane (Gendreau 1995). Right: Configuration of the two SIS on the ASCA focal plane.

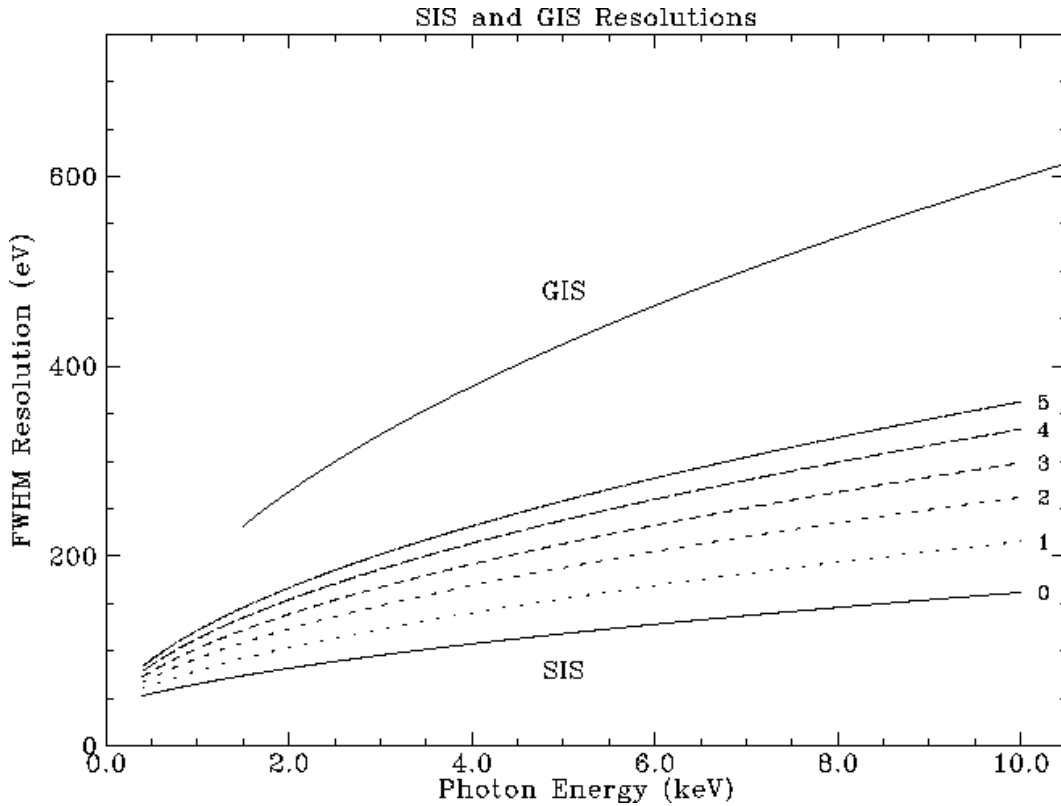


Figure 3.9: Energy resolution of the GIS and the SIS. For the SIS, measured or estimated energy resolutions of SIS1 in the 1CCD mode are plotted for at launch and 1, 2, 3, 4 and 5 years after the launch. SIS0 resolution is degrading somewhat more slowly than that of SIS1. In 2 and 4 CCD modes, the RDD effect further degrades the resolution somewhat. See http://heasarc.gsfc.nasa.gov/docs/asca/asca_nra06/appendix_e/node9.html for details.

treated as the Gaussian distribution. In the case of ASCA, the on-board processor maintains a coarse map of the dark levels (each chip is divided into 16 by 16 regions by default) and subtracts these from individual pixel values. The dark frame map is calculated assuming a symmetric noise around the mean dark level. Unfortunately, the cumulative effects of the radiation damage have created a population of active pixels which skews this distribution, leading to imperfect dark level subtraction on-board. This effect is called the Residual Dark Distribution (RDD). The RDD depends on the clocking mode, and therefore, it is most pronounced in 4-CCD mode (an integration time of 16 s), and less important in 1-CCD mode (an integration time of 4 s).

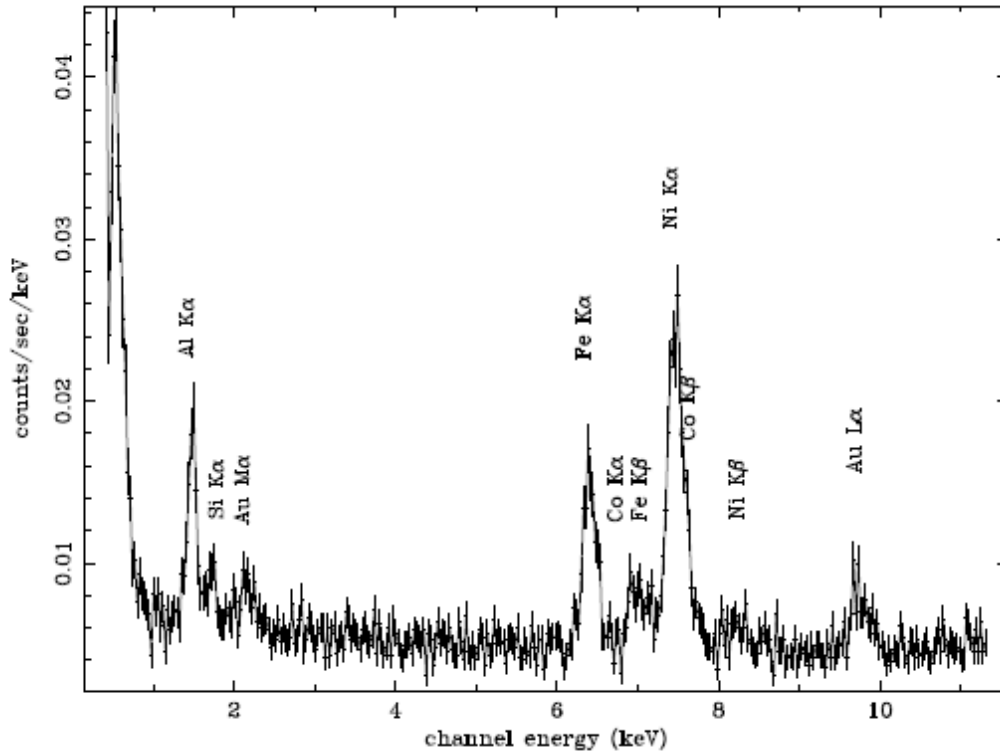


Figure 3.10: The SIS spectrum for the dark earth data (Gendreau 1995).

Background

The SIS background is quite stable and its count rate correlates with the local cutoff rigidity value, indicating that the background is mainly induced by high energy particles, except at the South Atlantic Anomaly (SAA). Figure 3.10 shows the SIS spectrum of the dark earth data. Since ASCA took an almost circular orbit with an average altitude of 520–620 km, inside the Earth’s magnetosphere, the SIS was little affected by soft protons, which seriously damaged ACIS and EPIC described in the following sections.

3.2.2 ACIS

The Advanced CCD Imaging Spectrometer (ACIS) is comprised of ten CCDs with 1024×1024 pixels; 2×2 array of ACIS-I(I0–I3) for imaging and 1×6 array of ACIS-S (S0–S5) for imaging and grating spectroscopy. The pixel size is $24 \mu\text{m}$ and the angular resolution with the HRMA is 0.5 arcmin. Two CCDs (S1 and S3) are back-illuminated (BI) and the others are front-illuminated (FI). The layout of CCD chips

ACIS FLIGHT FOCAL PLANE

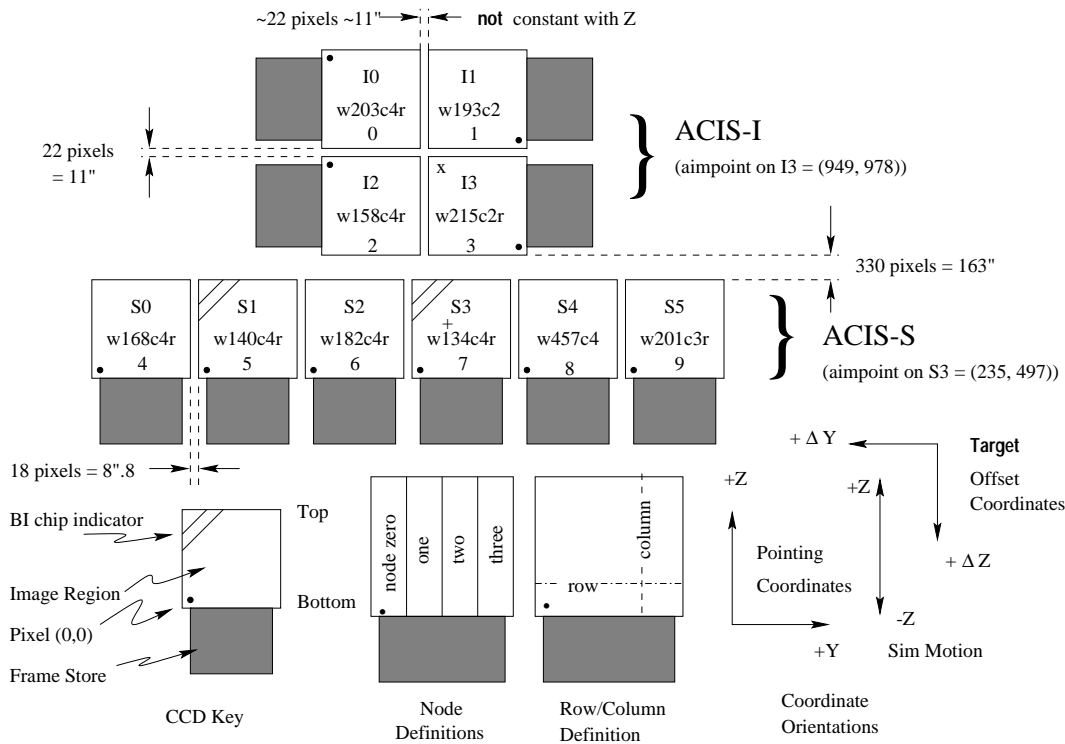


Figure 3.11: A schematic drawing of the ACIS focal plane; insight to the terminology is given in the lower left. Note the nominal aimpoints: on S3 (the '+') and on I3 (the 'x') (Weisskopf et al. 2003).

is shown in figure 3.11.

Energy resolution

After the launch, the CCD chips were seriously damaged with low energy protons reflected by the X-ray telescope onto the focal plane during radiation belt passage. Low energy protons deposited their energy in the buried channels at the HRMA side of the FI chips and increased the CTI. BI chips, on the other hand, were not impacted although they exhibited poorer resolution in pre-launch. Since the channels are near the gates and the gates face in the direction opposite to the HRMA, the energy resolution for the BI chips remains nearly at pre-launch values. In the present operation, the ACIS is not left at the focal position during the radiation belt passage, and no serious degradation in performance has been encountered. By decreasing the CCD temperature from -90°C (before damaged) to -120°C , the CTI

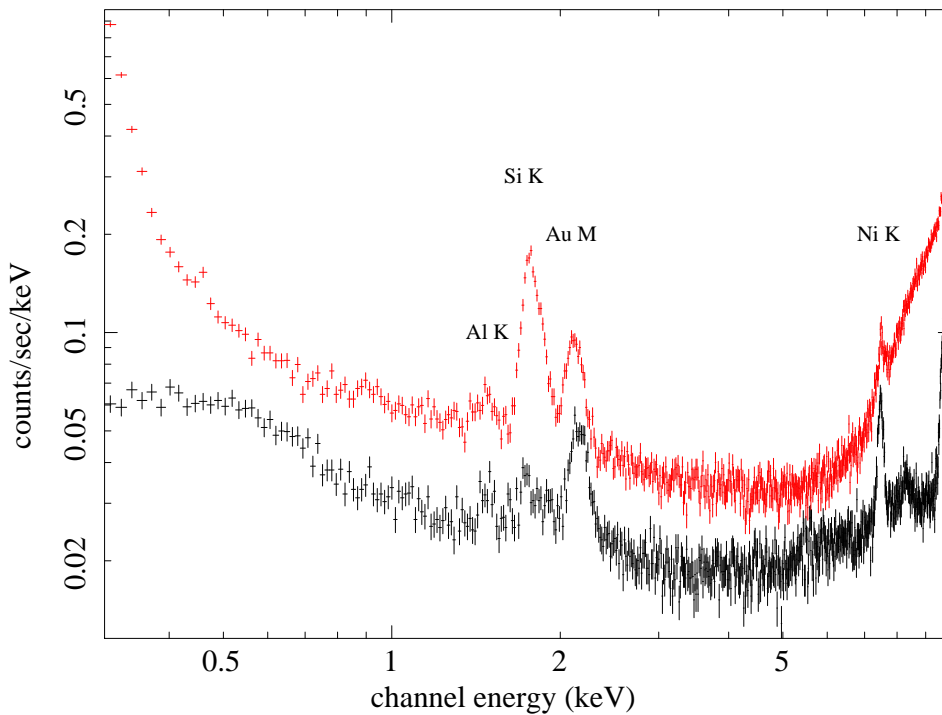


Figure 3.12: The ACIS background spectra of I0 (black) and S3 (red) extracted from the Chandra blank-sky database.

effect is reduced as possible.

Background

Figure 3.12 shows the ACIS background spectra measured in a stowed position (moving ACIS further away from the external calibration source than in the HRC-I position). In general, the background counting rates are stable during an observation. Furthermore, the spectral shape of the non-X-ray background has been remarkably constant during 2000–2005 for both BI and FI chips, even though the overall background rate showed secular changes by 20–30%. When the quiescent background spectra from different observations are normalized to the same rate in the 10–12 keV interval, they match each other to within $\pm 3\%$ across the whole Chandra energy band. Occasionally, however, there are large variations (flares). Figure 3.13 shows the frequency of such variations when compared to the quiescent background. An average fraction of the exposure affected by flares above the filtering threshold used for the blank-sky background datasets (a factor of 1.2 above the

nominal rate) was about 6% for the FI chips and up to 1/3 for the BI chips during the first few years of the mission.

3.2.3 EPIC

The European Photon Imaging Camera (EPIC) consists of two MOS (Metal Oxide Semiconductor) CCD cameras (Turner et al. 2001) and one pn-type CCD camera (PN) (Strüder et al. 2001). The PN chip array is slightly offset with respect to the optical axis of its X-ray telescope so that the nominal, on-axis observing position does not fall on the central chip boundary. This ensures that $\geq 90\%$ of the energy of an on-axis point source are collected on one PN chip. The two EPIC MOS cameras are rotated by 90° with respect to each other. The dead spaces between the MOS chips are not gaps, but unusable areas due to detector edges. The MOS chips physically overlap each other, the central one being located slightly behind the ones in the outer ring.

Energy resolution

The energy resolution of EPIC, shown in figure 3.15, is monitored by the onboard calibration source, which produces strong Al $K\alpha$ and Mn $K\alpha$ lines. The resolution of the MOS cameras degraded significantly with time up to the epoch where the cameras were cooled from -100°C to -120°C . After this epoch the degradation has been minima. In the same description of the ACIS CCD, the PN CCDs are less affected since they are back-illumination type.

Background

XMM-Newton takes a highly elliptical orbit with an apogee of about 115,000 km and a perigee of about 6000 km and thus mostly fly outside of the Earth's magnetosphere. This is thought to be responsible for the violent variability of the background of the EPIC cameras as large as two orders of magnitudes. This variation is caused by protons scattered through the mirror system.

The background of the EPIC cameras consists of mainly two components: the cosmic X-ray background (CXB) and the instrumental non-Xray background (NXB). The latter component is mainly due to the interactions of charged particles with the structure surrounding the detectors and the detectors themselves. This component can be further divided into two components: a transient component and a quiescent component. Since spatial and temporal characteristics are different between these components, it is important to study them separately.

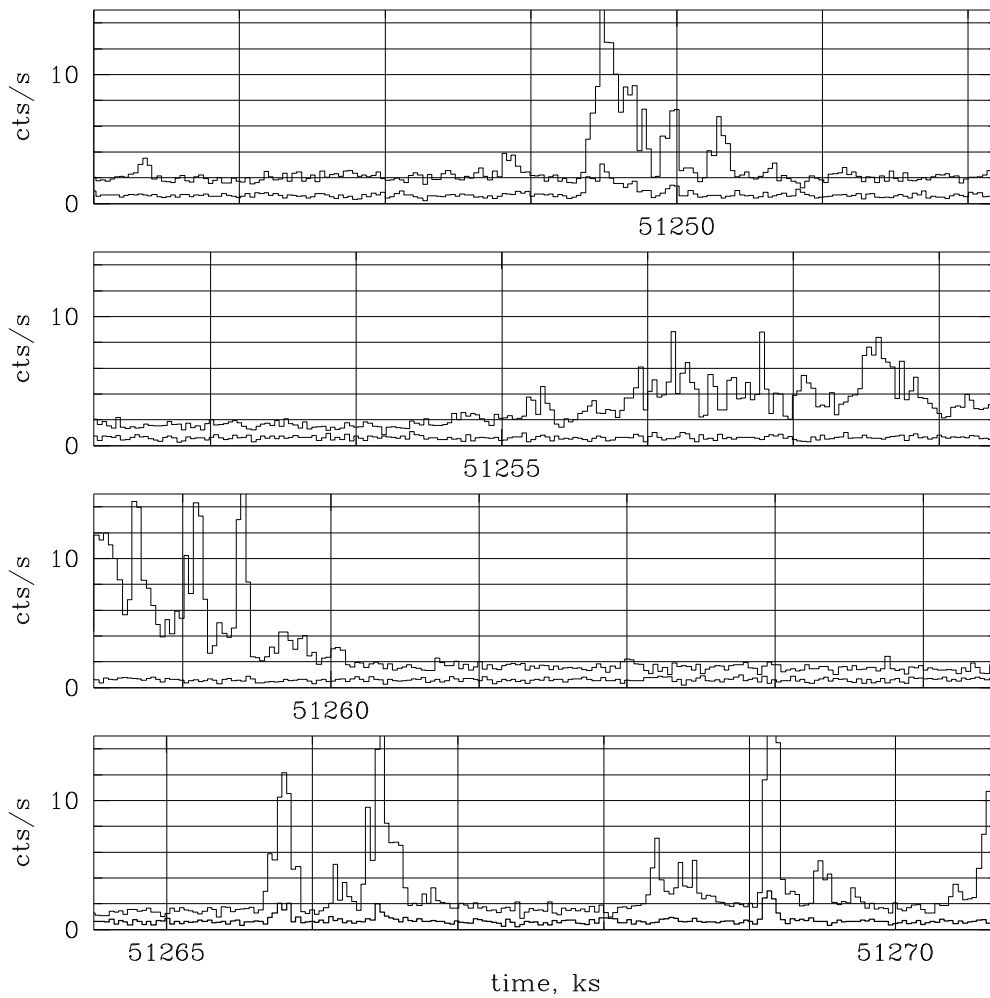


Figure 3.13: An example of the ACIS background counting rate versus time: S3 (the BI chip; top curve) and I2 (the FI chip; bottom curve). These are for the standard grades and the band from 0.3–10 keV. See <http://cxc.harvard.edu/proposer/POG/html/ACIS.html> for details.

Comparison of focal plane organisation of EPIC MOS and pn cameras

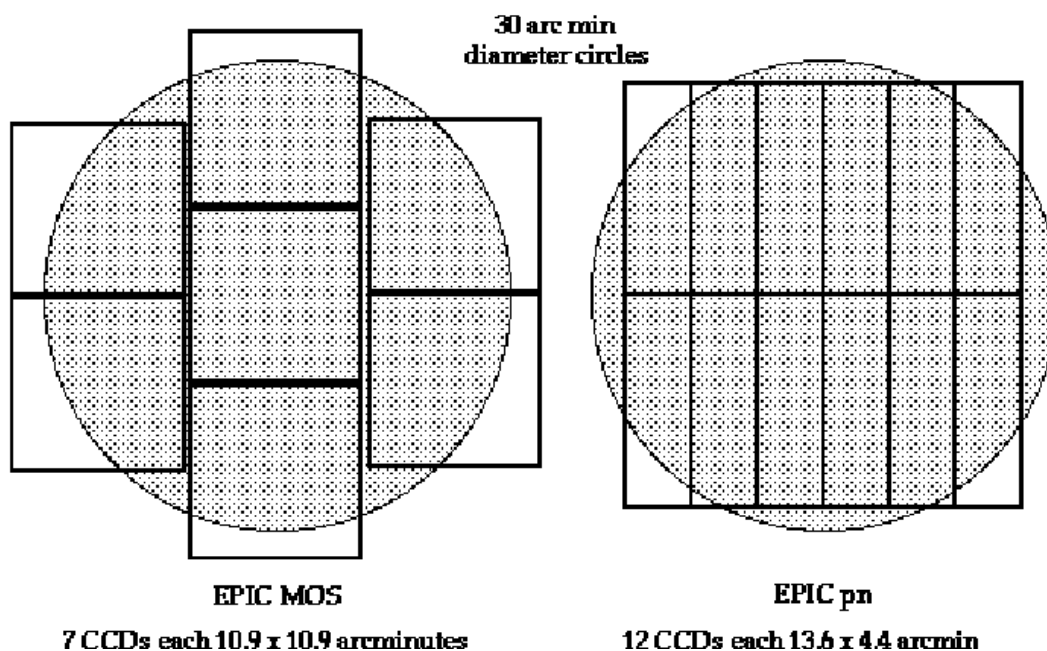


Figure 3.14: A sketch of the field of view of the two types of EPIC camera; MOS (left) and PN (right). The shaded circle depicts a 30 arcmin diameter area. For the alignment of the different cameras with respect to each other in the XMM-Newton focal plane refer to the text. See http://xmm.vilspa.esa.es/external/xmm_user_support/documentation/uhb_2.5/node24.html for details.

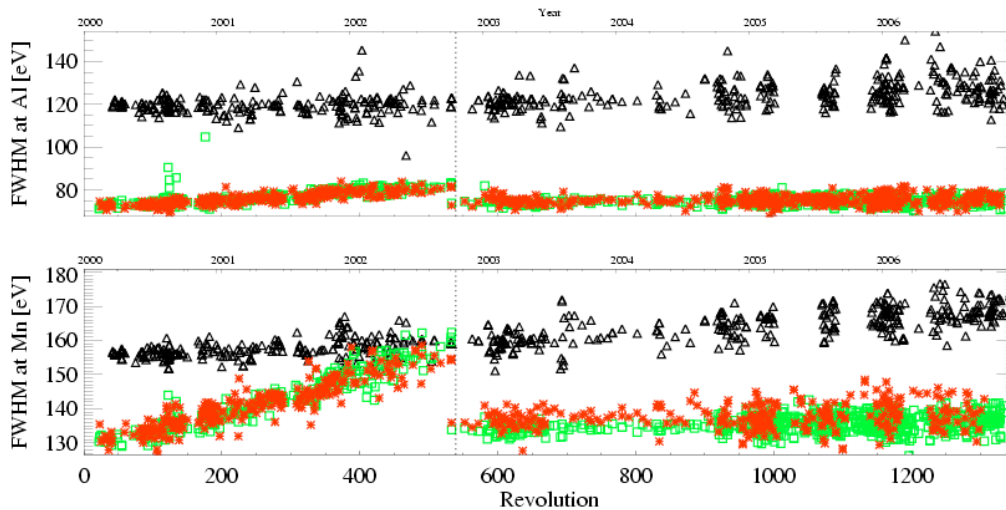


Figure 3.15: Energy resolution of MOS1-CCD1 (red asterisk), MOS2-CCD1 (green square) and PN-CCD4 (black triangle). The drop after rev. 532 is due to the cooling of the cameras. See <http://xmm.vilspa.esa.es/docs/documents/CAL-TN-0018.pdf> for details.

The transient component is thought to be induced by soft protons with energies less than a few hundred keV. Since the soft protons are scattered through the mirror system, they are vignettted. The spectra of soft proton flares are variable and no clear correlation has been found between intensity and spectral shape. Therefore, observation intervals affected by this component have to be screened off.

The quiescent component is induced by high-energy cosmic rays with energies larger than several hundred MeV which penetrate the satellite. The quiescent background consists of a continuum component and lines. While the continuum component is induced by high energy particles directly in the detector, the lines correspond to the fluorescent lines of the surrounding structures. Whereas the continuum component is spatially flat, the line component spatially changes depending on the detector structure. Figure 3.16 shows background spectra for the MOS and the PN cameras and images of the typical intrinsic lines. Further details are described in Carter & Read (2007).

3.2.4 XIS

The four Suzaku X-ray Imaging Spectrometers (XISs) are named XIS0, 1, 2 and 3, and each CCD is located in the focal plane of an X-ray Telescope; those telescopes are known respectively as XRT-I0, XRT-I1, XRT-I2, and XRT-I3 (figure 3.17). One

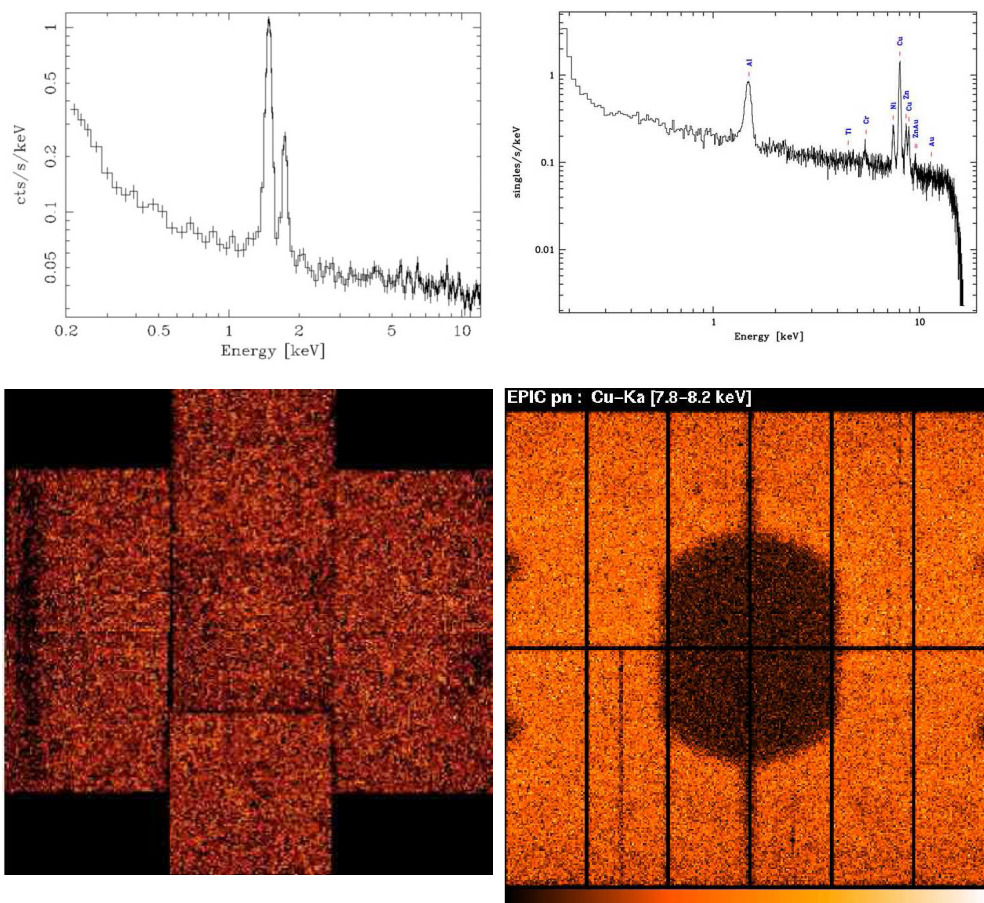


Figure 3.16: Upper: Background spectra for the MOS1 camera (left) and the PN camera (right) during an observation with the filter wheel in the closed position. Lower: Images of the MOS camera of Al K line at 1.48 keV (left) and the PN of Cu K at 8.04 keV (right) (Carter & Read 2007).

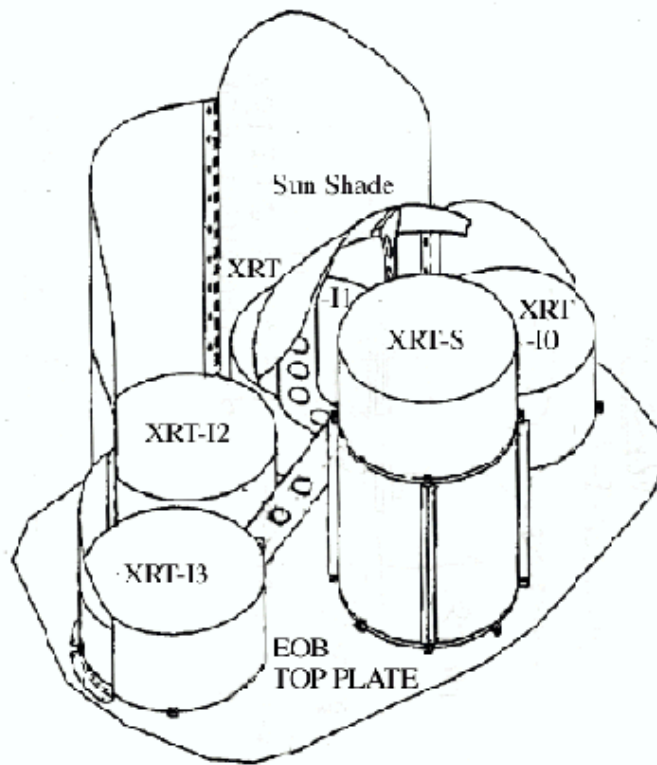


Figure 3.17: Layout of the XRTs on the Suzaku spacecraft.

of the XISs, XIS1, uses a back illuminated CCDs, while the other three use front illuminated CCDs.

A single XIS CCD chip consists of four segments (marked A, B, C and D in figure 3.18). The Analog Electronics (AE) drives the CCD and processes its data. Charge clouds produced in the exposure area in the CCD are transferred to the Frame Store Area (FSA) after the exposure according to the clocks supplied by the AE. To minimize the thermal noise, the sensors need to be kept at $\sim -90^{\circ}\text{C}$ during observations. This is accomplished by thermo-electric coolers (TECs), controlled by TEC Control Electronics, or TCE. The AE and TCE are located in the same housing. The digital electronics system for the XISs consists of two Pixel Processing Units (PPU) and one Main Processing Unit (MPU). The PPUs access the raw CCD data in the Pixel RAM, carry out event detection, and send event data to the MPU. The MPU edits and packets the event data, and sends them to the satellite's main digital processor.

To reduce contamination of the X-ray signal by optical and UV light, each XIS

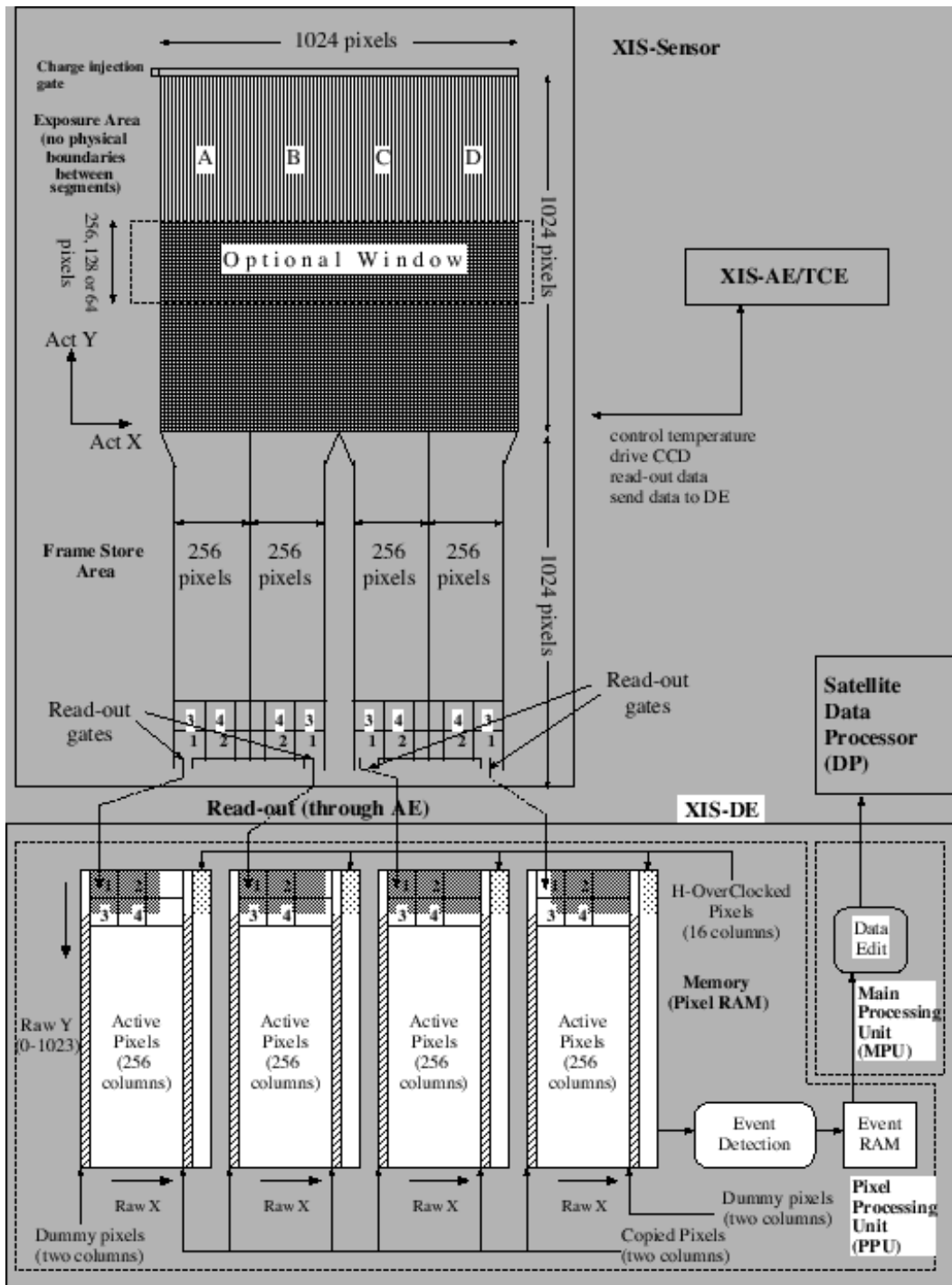


Figure 3.18: One XIS instrument.

has an Optical Blocking Filter (OBF) located in front of it. The OBF is made of polyimide with a thickness of 1000 Å, coated with a total of 1200 Å of aluminum (400 Å on one side and 800 Å on the other side). To facilitate the in-flight calibration of the XISs, each CCD sensor has two ^{55}Fe calibration sources. These sources are located on the side wall of the housing and are collimated in order to illuminate two corners of the CCD. They can easily be seen in two corners of each CCD. A small number of these X-rays scatter onto the entire CCD.

After the launch of Suzaku, the four XISs had been operated successfully for more than a year. However, a large amount of leaked charge suddenly appeared in one of the sensors, XIS2, in November 2006. Because the leak of charge was unable to be suppressed, we stopped using XIS2 for scientific observations.

Energy Resolution

Performance of the XIS is gradually degrading since the launch of Suzaku due to the radiation damage. Figure 3.19 shows the time history of the energy resolution for Mn $K\alpha$ from the ^{55}Fe calibration sources for XIS. Energy resolution at Sept. 2006 measured by the ^{55}Fe is about 200 eV (FWHM) at 5.9 keV, while it was ~ 130 – 135 eV just after the launch.

In principle, a precision charge injection capability can mitigate the effects of in-flight radiation damage (Bautz et al. 2004). A sufficient quantity of charge injected periodically during the array readout process (spaced-row charge injection; SCI) will tend to fill radiation-induced traps, and in so doing reduce the effects of these traps on the devices charge transfer efficiency (CTE). Because the traps need to be filled quite often, we inject charge every 54 rows in every exposure. The charge injected rows are not usable to detect X-ray photons, and become dead area.

With this SCI technique, XIS achieve to keep the high energy resolution (~ 140 – 150 eV at 5.9 keV) in a long period. However, Suzaku data used in this thesis are taken in an early time from the launch and not operated with SCI.

Background

All four XISs have low backgrounds, due to a combination of the Suzaku orbit and the instrumental design. In the XIS, the background originates from the cosmic X-ray background (CXB) combined with charged particles (NXB). Currently, flickering pixels are a negligible component of the background.

There are also fluorescence features arising from the calibration source as well as material in the XIS and the XRTs. In XIS0, the Mn line due to the scattered

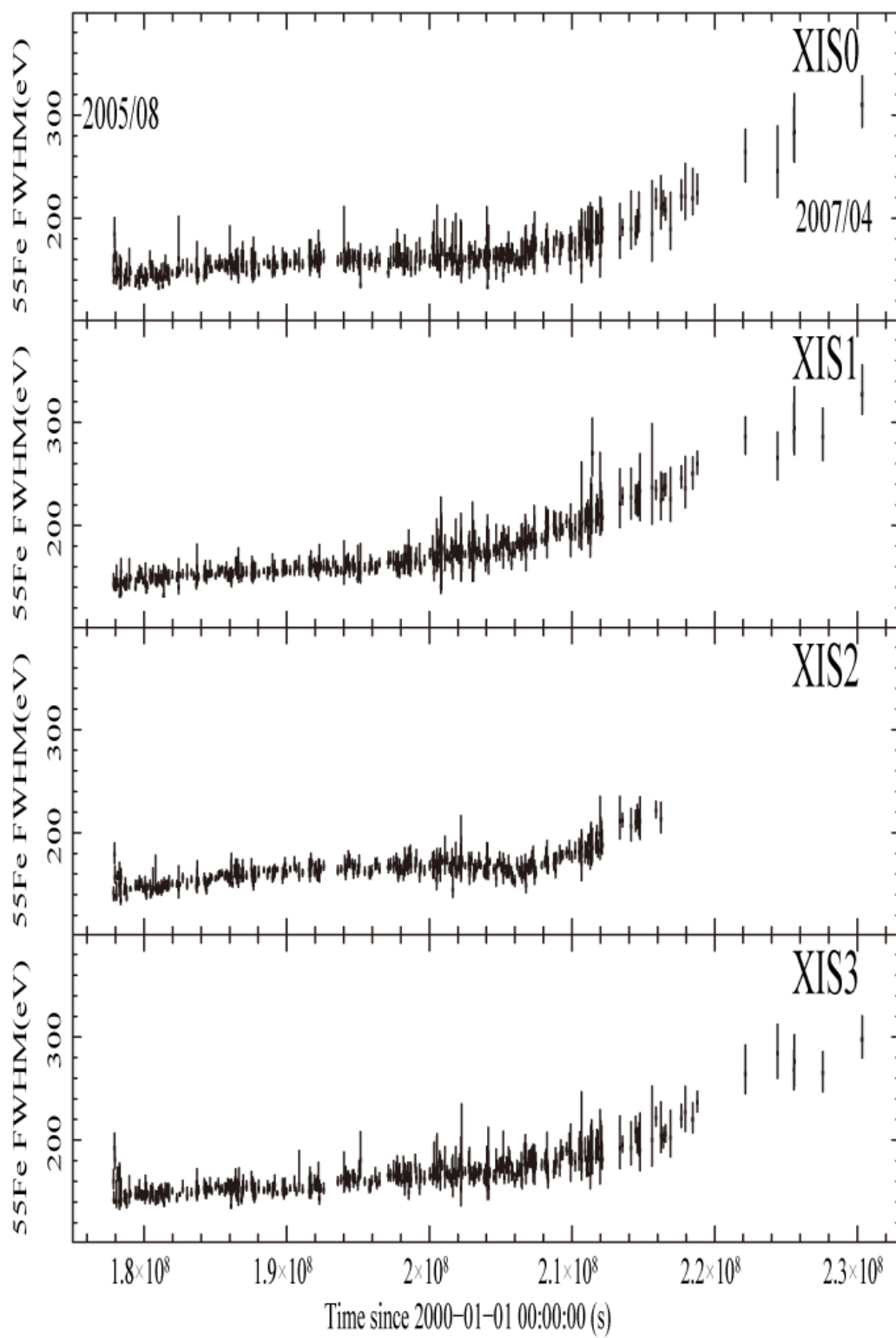


Figure 3.19: The time history of the energy resolution for Mn $K\alpha$ from the ^{55}Fe calibration sources for XIS.

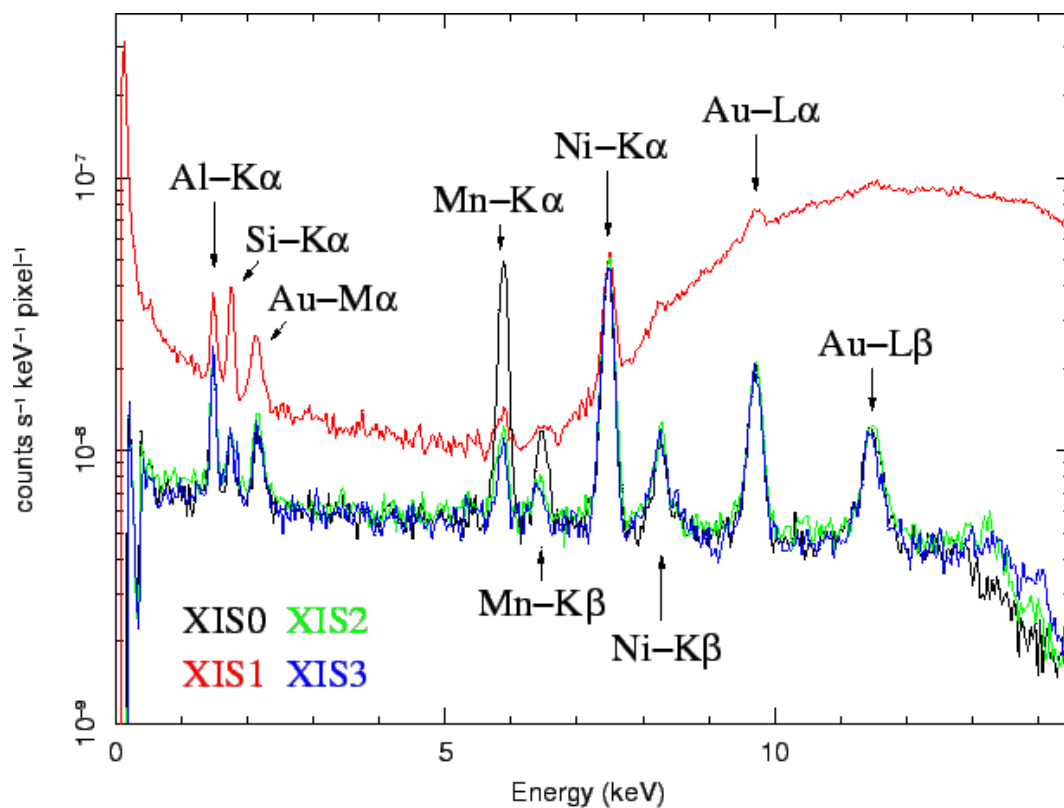


Figure 3.20: The XIS background rate for each of the four XIS detectors, with prominent fluorescent lines marked. These spectra are based on the observations of the dark Earth for ~ 800 ks.

X-rays from the calibration sources contaminates the whole chip. The other lines are fluorescent lines from the material used for the sensor. The NXB is not uniform over the chip. Its flux tends to be slightly higher at larger ACTY as shown in figure 3.21. This is because some fraction of the NXB is produced in the frame-store region. The fraction may be different between the fluorescent lines and the continuum. This causes slight difference in the ACTY dependence of the NXB.

The total flux of the NXB depends on the cut-off rigidity (COR) as shown in figure 3.22. This may be natural as the NXB is produced by the charged particles, whose flux is higher at lower COR. This means that, when we use the NXB database to subtract the background, we need to select the NXB with an appropriate range of the COR, which match with the COR distribution of the on-source observations. For this purpose, the NXB database available from the Suzaku web page is sorted with the COR.

The count rate of the PIN upper discriminator (PIN-UD) in the HXD also correlates the flux of the NXB. Recent studies show the PIN-UD provides slightly better reproducibility of the NXB. The reproducibility of the NXB in the 5–12 keV band is evaluated to be 3–4% of the NXB, when we use the PIN-UD as the NXB sorting parameter (Tawa et al. 2008).

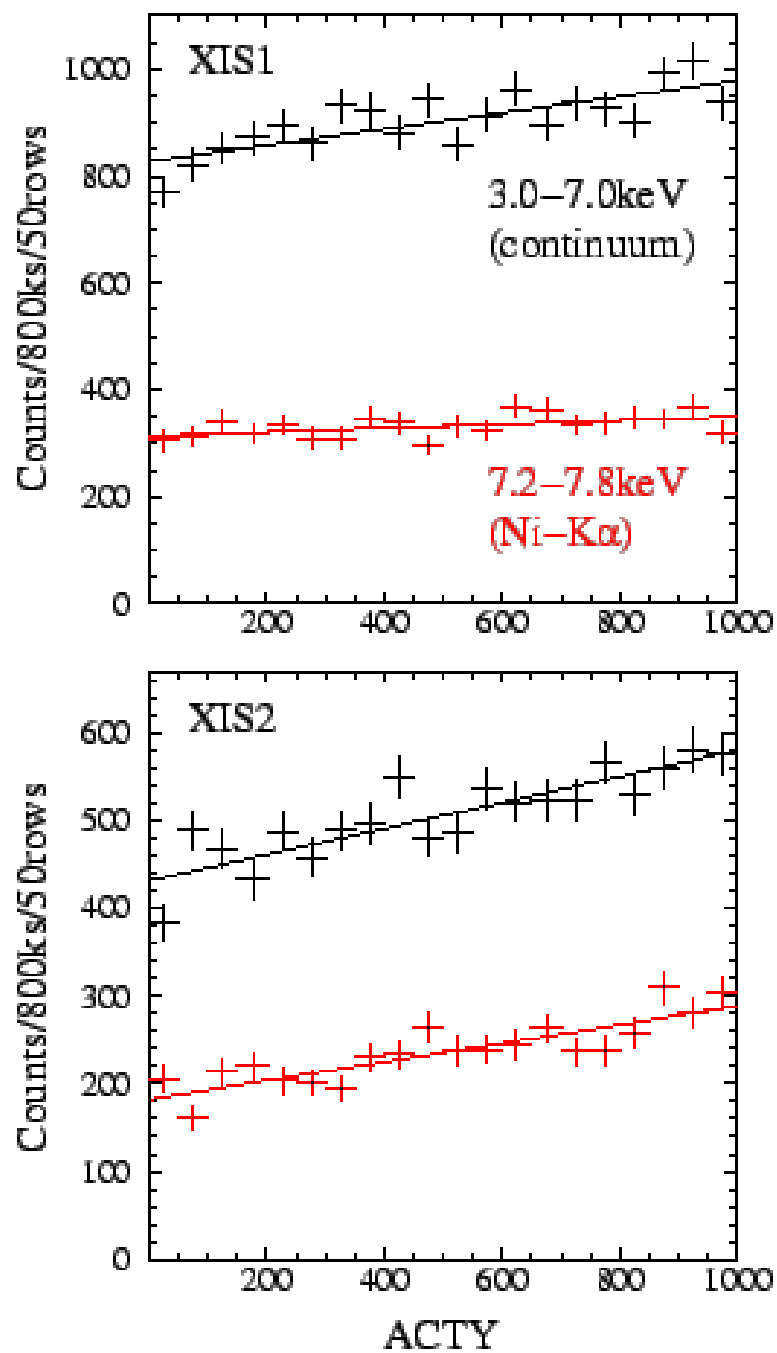


Figure 3.21: ACTY dependence of the NXB for XIS1 and XIS2.

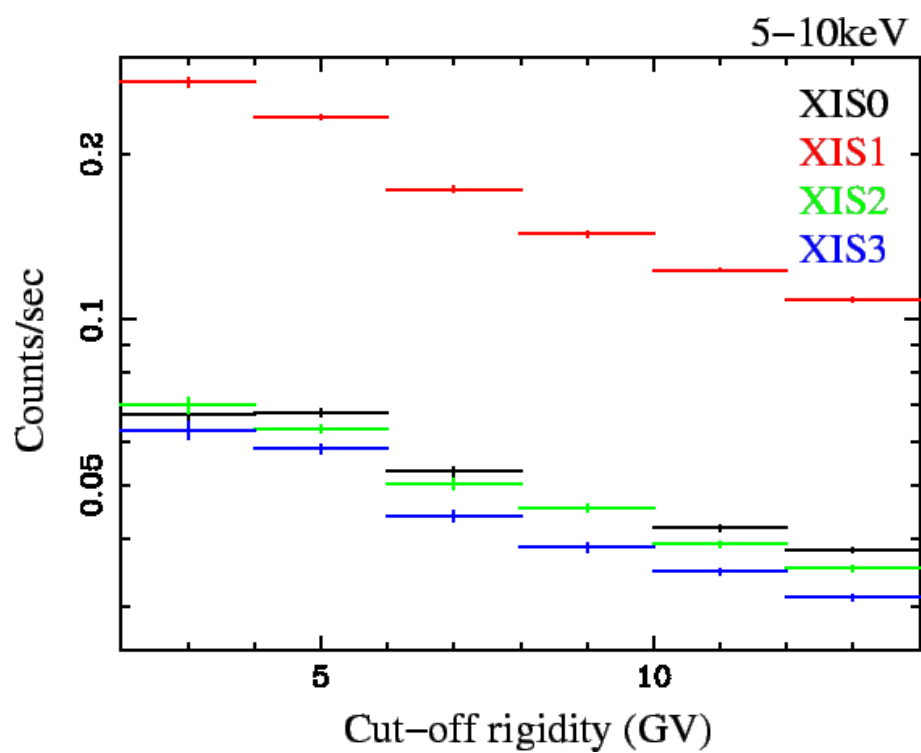


Figure 3.22: Cut-off rigidity dependence of the NXB (average intensity in 5–10 keV) for each sensor.

Chapter 4

Observations

We use four deep observations and two short surveys listed in table 4.1. For imaging analysis, we only use the deep observation data.

4.1 The Suzaku Observation

4.1.1 Data Collection

The Sgr B region was observed with the XIS on 10-12 October 2005. The XIS observation was made with the normal mode. The effective exposure time after removing the epoch of low Earth elevation angle ($ELV \leq 5^\circ$) and the South Atlantic Anomaly was about 89 ksec.

4.1.2 The Gain Tuning

In a quick look of the spectrum, we found strong lines at ~ 6.7 keV and ~ 6.4 keV, in the whole CCD imaging area (IA). These lines may be due to the largely extended

Table 4.1: Observation data list

Observatory	Obs. ID	Date (yyyy/mm/dd)	Exposure Time (sec)
ASCA	52006000	1994/09/22	58,395
ASCA	52006001	1994/09/24	21,500
Chandra	944	2000/03/29	98,629
XMM-Newton	0112971501	2001/04/01	12,649
Chandra	2280	2001/07/16	10,423
XMM-Newton	0203930101	2004/09/04	42,282
Suzaku	100037060	2005/10/10	89,072

Galactic center diffuse X-ray emission (GCDX). These lines are most likely $K\alpha$ lines of Fe XXV (6.67 keV) and Fe I (6.40 keV). Using the center energies of the two strong lines, we made fine correction of the CTI (Charge Transfer Inefficiency), and fine gain tuning in XIS-to-XIS and segment-to-segment levels (relative gain tuning). Then the absolute gain tuning is made using the ^{55}Fe calibration sources irradiating the CCD corners. Details of this procedure and its usefulness are demonstrated in Koyama et al. (2007d).

4.1.3 The Position Tuning

After the CTI correction and fine gain tuning, we added all the XIS data and made a composite image of the Sgr B region in the 2–10 keV band (figure 4.1). The diffuse enhancement in the northwest corresponds to the Sgr B2 complex. In addition, we found two point sources at the southeast edge of the XIS field of view (FOV). We made radial profiles of these two sources and determined the peak positions to be $(l, b) = (0^\circ 5762, -0^\circ 1736)$ and $(0^\circ 6626, -0^\circ 2225)$ in the nominal Suzaku coordinate. We searched for the Chandra Galactic center survey map, and found possible counterparts, CXO J174741–283213 and CXO J174804.8–282919 (Muno et al. 2003). The Galactic coordinates of these sources are $(l, b) = (0^\circ 5762, -0^\circ 1796)$ and $(0^\circ 6625, -0^\circ 2289)$. Therefore the Suzaku nominal coordinate is systematically shifted by $(\Delta l, \Delta b) = (0^\circ 0001, 0^\circ 0062)$ from the Chandra coordinate. Since the aspect solution of Chandra is very accurate, within sub-arcsec, we made fine-tuned of the Suzaku position by shifting $(-0^\circ 0001, -0^\circ 0062)$ in the (l, b) coordinate. Hereafter we use this re-registered coordinate.

4.2 The XMM-Newton Observations

4.2.1 Data Collection

The X-ray data have been obtained with the EPIC cameras onboard XMM-Newton on 1 April 2001 and 4 September 2004. The observations were operated in the extended full frame mode. The data have been analysed using the Science Analysis Software (sas 7.1.0). Event files for both the PN and the MOS detectors have been produced using the epproc and emproc tasks of sas, respectively. The event files were screened for the high particle background periods. The background light curves and the screening criteria are shown in figure 4.2.

In our analysis, we have dealt only with events corresponding to patterns 0–4 for the PN and 0–12 for the MOS instruments.

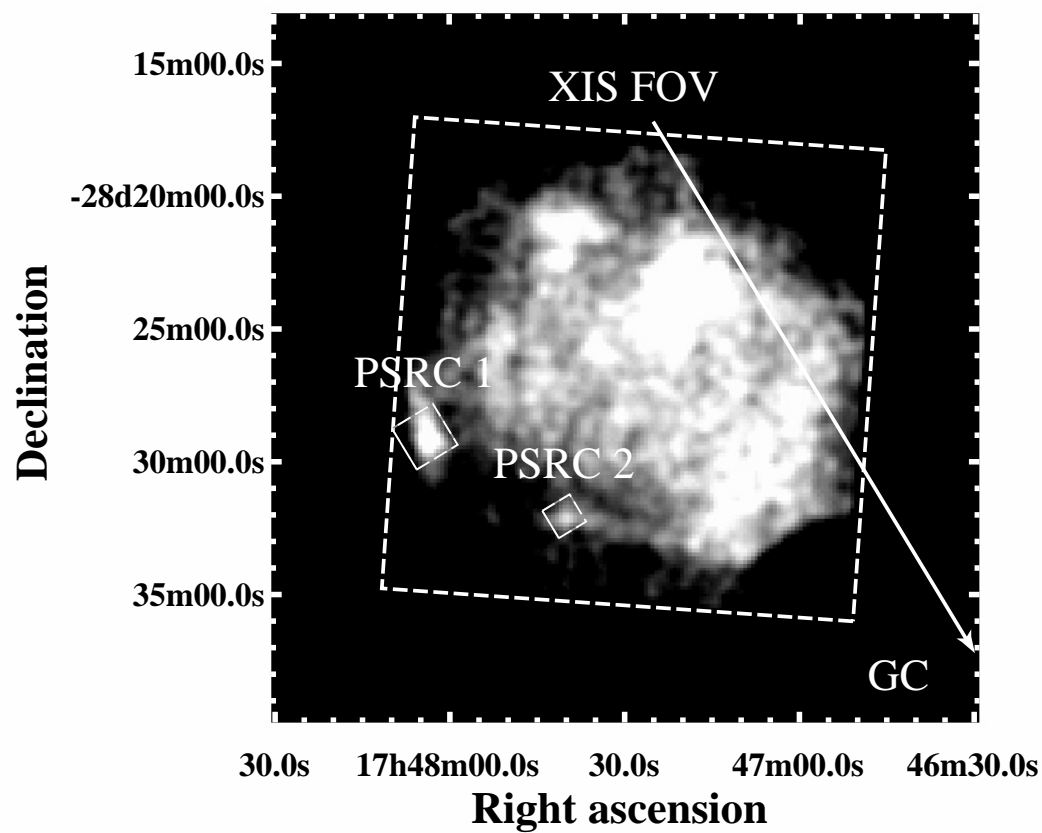


Figure 4.1: The Suzaku image of the Sgr B region in the 2–10 keV band. All the four XIS data are co-added. The dotted square is the XIS field of view (FOV).

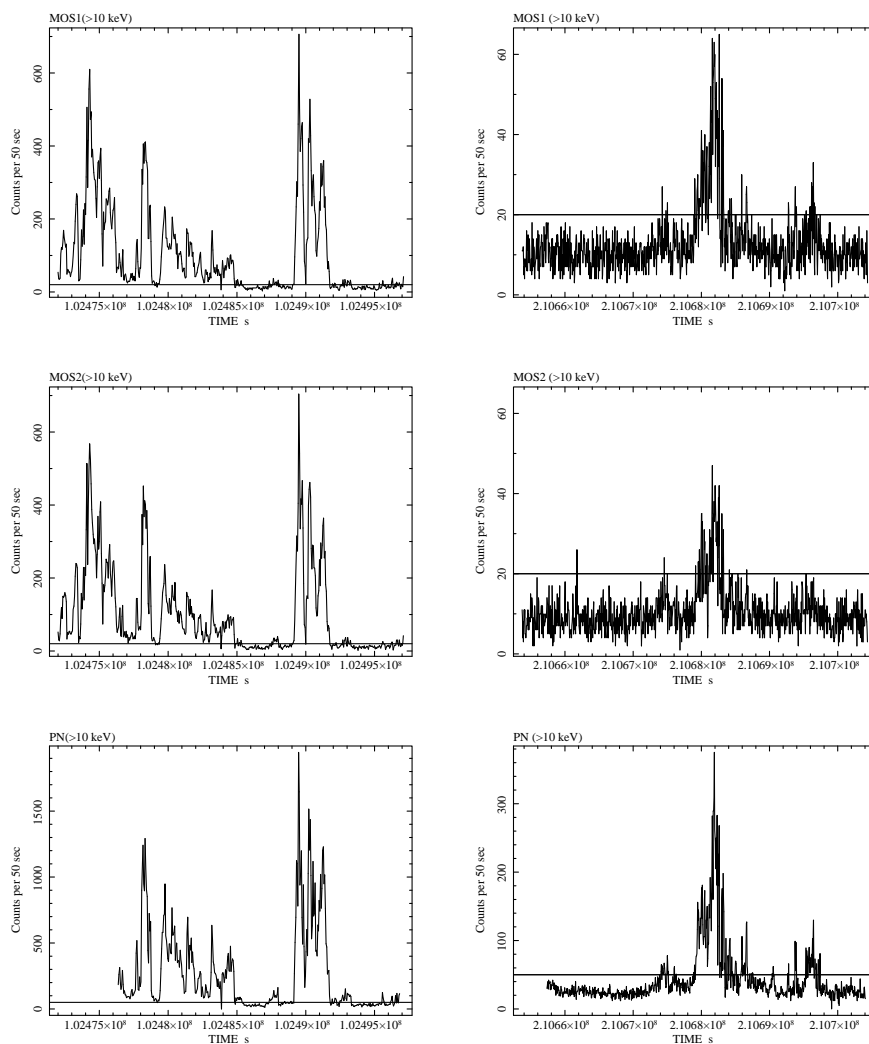


Figure 4.2: Background light curves of 2001 (left) and 2004 (right) observations with the MOS and the PN detectors. Events with over 10 keV and pattern 0 are accumulated. Horizontal lines indicate the screening criteria ($0.4 \text{ counts s}^{-1}$ for MOS and $1.0 \text{ counts s}^{-1}$ for PN).

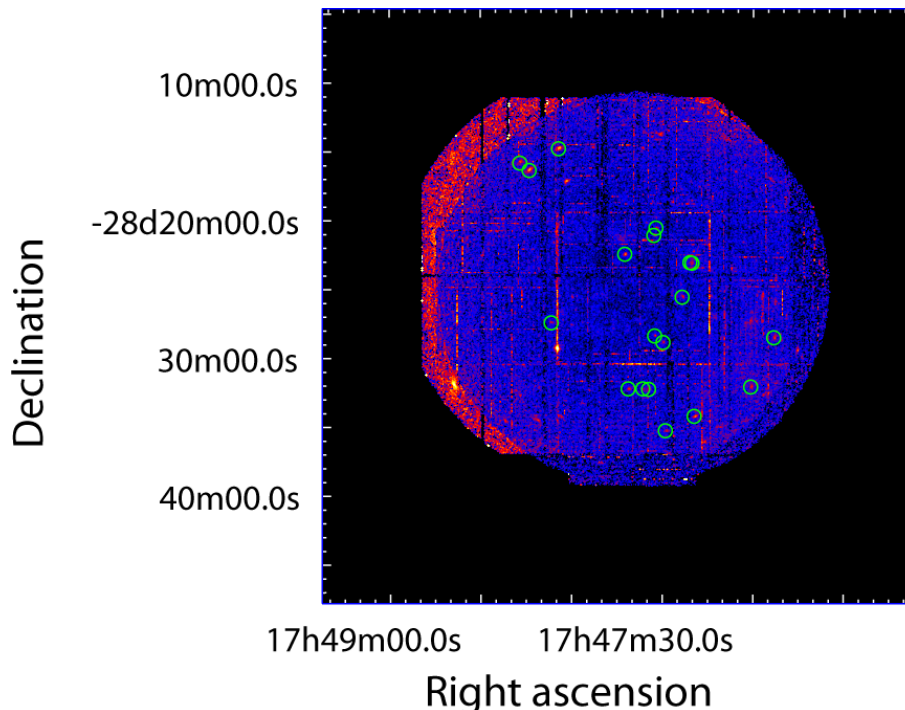


Figure 4.3: The XMM-Newton image of the Sgr B region in the 0.3–10 keV band. All MOS and PN data in 2004 are co-added. Circles indicate point sources identified with the Chandra point source catalogue (Muno et al. 2003).

4.2.2 The Position Tuning

For the observation in 2004, we make the total band images (0.3–10 keV) of each detector and detect point sources; 93 from MOS1, 97 from MOS2, 111 from PN. There are 27 sources detected with all the detectors within positional uncertainties of 10 arcsec which is comparable to the size of PSF of EPIC at 6 keV, and 19 sources have possible counterparts with the point sources catalogued with Chandra (Muno et al. 2003). The composite image and distribution of identified point sources are shown in figure 4.3. Since the mean of their differences against the Chandra positions is $(-0^{\circ}0006, 0^{\circ}0003)$ in the celestial coordinate, we tune the XMM-Newton frame by shifting $(\Delta RA, \Delta DEC) = (0^{\circ}0006, -0^{\circ}0003)$.

4.3 The Chandra Observations

4.3.1 Data Collection

Sgr B2 was observed using the ACIS-I onboard the Chandra observatory on 29 March 2000 and 16 July 2001. We use event files provided by the standard pipeline

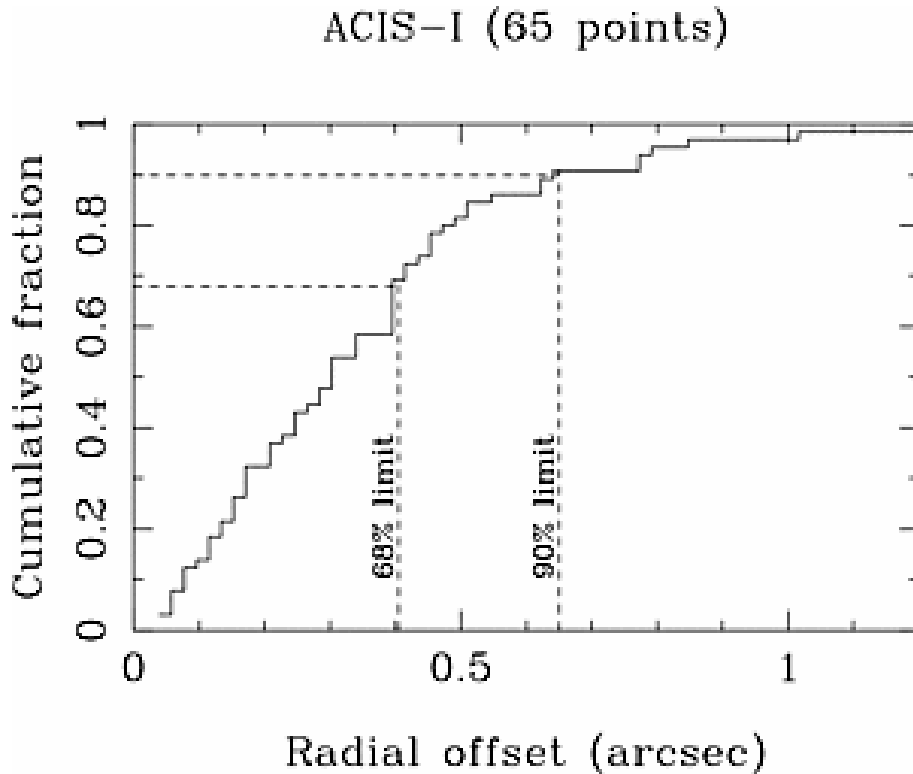


Figure 4.4: The distribution of the Chandra aspect offsets (Weisskopf et al. 2003).

processing. Only Grade 0, 2, 3, 4 and 6 events are used in the analysis. Each CCD chip subtends an 8.3-arcmin square on the sky while the pixel size is 0.5 arcsec. The on-axis spatial resolution is 0.5-arcsec with a full width at half-maximum (FWHM). Images, spectra, ancillary files and response matrices have been created using the *ciao* v3.4 software.

4.3.2 Position Accuracy

Taking the advantage of the highest positional resolution, the Chandra aspect offsets have been determined by numerous observations with X-ray sources having well-determined radio or optical/IR counterparts. Figure 4.4 shows the distribution of aspect offsets for Chandra. The absolute positional accuracy is determined to be 0.6 arcsec (Weisskopf et al. 2003), which is the best quality among the four observatories. In this thesis, we regard the Chandra frame as the standard astrometry.

4.4 The ASCA Observations

4.4.1 Data Collection

The ASCA observations of Sgr B2 were performed on 22 and 24 September 1994 in 4-CCD mode for ~ 80 ks in total. We use the event files provided by the standard pipeline processing. Since the observation dates and aim points are almost the same, we merge the two observation data. Since the GIS data do not have enough energy resolution (~ 470 eV at 5.9 keV) to separate the iron lines, we use the SIS data alone for the analysis. We use the software package HEASoft 6.2 in the analysis.

4.4.2 The Position Tuning

Since no available point sources for the absolute astrometry correction are found in the SIS field of view, the astrometric uncertainty of the SIS image remains about 40 arcsec¹.

¹See http://heasarc.gsfc.nasa.gov/docs/asca/cal_probs.html

Chapter 5

Result I — Suzaku Discoveries of New Diffuse Sources

5.1 Suzaku Overview of the Sgr B2 Region

The X-ray spectrum of all the Sgr B region is given in figure 5.1. The spectra of the four XISs (XIS0–XIS3) were co-added and the night earth spectrum (non X-ray background; here, NXB) was subtracted. With the excellent energy resolution of the XIS for diffuse sources, we can clearly resolve the 6.40 keV, 6.67 keV and 6.97 keV lines. These are $K\alpha$ lines from neutral FeI, He-like Fe XXV and hydrogenic Fe XXVI. The 6.97 keV line may contain a small fraction of $K\beta$ line of FeI (7.06 keV). Weak lines seen above 7 keV are $K\alpha$ of NiI (at ~ 7.5 keV), $K\alpha$ of Ni XXVII + $K\beta$ of Fe XXV (at ~ 7.8 – 7.9 keV) and $K\beta$ of Fe XXVI + $K\gamma$ of Fe XXV (at ~ 8.2 – 8.3 keV).

In order to study more quantitatively, we divided the XIS FOV into 16 (4×4) areas as is shown in figure 5.2 by the solid grids. For brevity, we assign coordinates for each square position such as (0, 0) and (3, 3), where the former and latter are lower-left and upper-right positions, respectively. Since the roll angle of the observation was nearly 0° , the north of this coordinate is also the north of the sky coordinate. We made X-ray spectra from the 16 squares. Since we already made fine adjustment among the four XISs, we added the four XIS data to make a composite spectrum. The NXB spectra were constructed from the night earth data in the same detector area of the 16-square regions. The NXB spectra from the four XIS were also co-added and were subtracted from the 16 squares of the Sgr B2 region. In these adding procedure, the four corners, (0, 0), (0, 3), (3, 0) and (3, 3) contain the MnI $K\alpha$ and $K\beta$ line from the built-in calibration sources, and we therefore excluded these areas in the following analysis. The NXB subtracted spectra were fitted with a thermal bremsstrahlung model, plus the Fe absorption edge at 7.1 keV and four

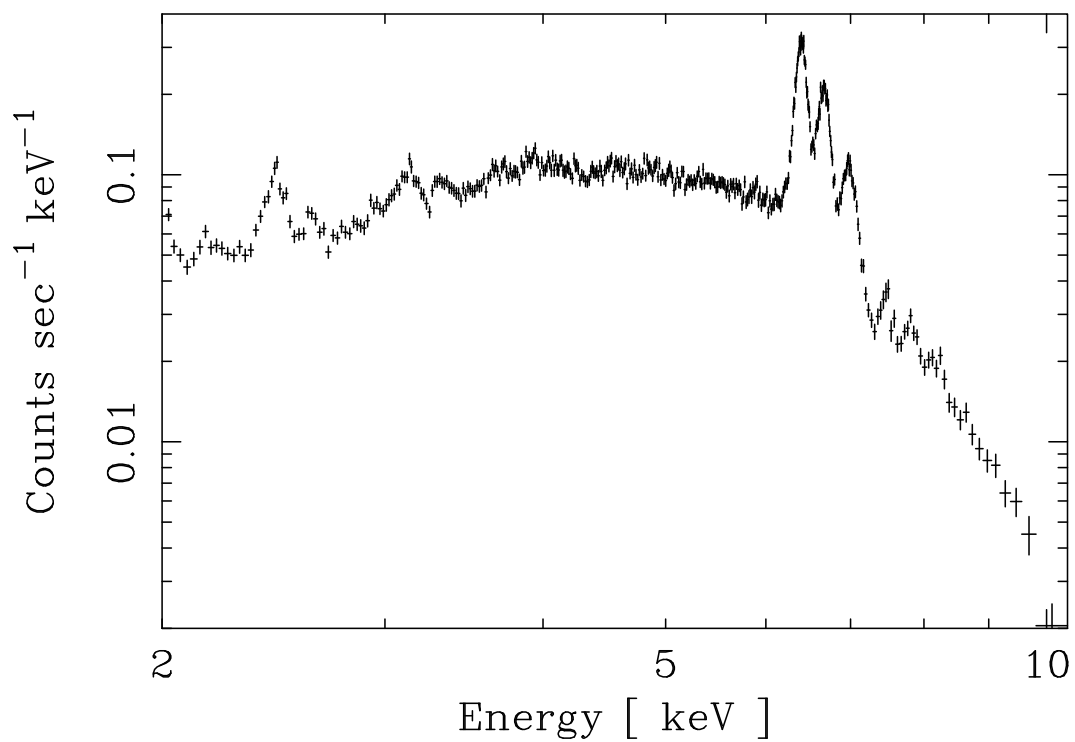


Figure 5.1: The X-ray spectra from the full FOV of the XIS, except the CCD corners irradiated by the build-in calibration sources. All four XIS data sets are co-added.

emission lines, which are the $K\alpha$ lines from Fe I (6.40 keV), Fe XXV (6.67 keV) and Fe XXVI (6.97 keV) and the $K\beta$ line from Fe I (7.06 keV). Since the energies of the latter two lines have a small separation of only about 90 eV, we constrain the center energy and flux such that the separation energy between the $K\alpha$ and $K\beta$ of Fe I is fixed to the theoretical value of 658 eV (7058 – 6400) and the flux of $K\beta$ is fixed to be 12.5% of that of $K\alpha$.

Since we find that the best-fit bremsstrahlung temperature is the same (7 keV) in all the regions within errors, we fix the temperature to be 7 keV, and extract the line and continuum fluxes from the 12 squares. Using the best-fit fluxes of the 6.40 keV, 6.67 keV, and 6.97 keV lines, we make color code maps (figure 5.2), which are the fluxes of the 6.40 keV (figure 5.2a) and the 6.67 keV lines (figure 5.2b) and the flux ratio of the 6.97 keV line to the 6.67 keV line (figure 5.2c). The continuum flux (normalization of the 7-keV bremsstrahlung) map is also given in figure 5.2d. Using the flat field simulation data provided by the XRT team, we corrected the telescope vignetting effect.

Both the 6.40 and 6.67 keV line maps show a large contrast in red and green colors, which means that the fluxes have large variation from position to position. On the other hand, the 6.97 keV/6.67 keV ratio is rather smooth (the contrast of colors is weak) except the position of (3, 2). If we exclude this position, the mean value of the other 11 squares is 0.39. Koyama et al. (2007d) reported that the bulk of the GC diffuse emission is due to hot plasma in nearly collisional ionization equilibrium (CIE) with temperature of about 6–7 keV. Since the mean value of the 6.97 keV/6.67 keV line ratio in the Sgr B2 region is almost identical to that of the GC, we safely assume that the origin of these lines is the same: hot plasma in the CIE with a temperature of 7 keV. The absolute surface brightness is about a half of the GC. The continuum flux is also smooth with a small but a systematic excess at the north position (2, 2). A significant excess of the 6.67 keV flux and deficit of the 6.97 keV/6.67 keV flux ratio at the position of (3, 2) indicates a presence of an extra component with a strong 6.67 keV line but no strong 6.97 keV line. The rather smooth distribution of the continuum X-ray fluxes (see figure 5.2d) also suggests that the excess emission is mainly due to the 6.67 keV line. Since the 6.67 keV line is most likely the $K\alpha$ of Fe XXV, the provable origin of the local 6.67 keV excess is due to hot plasma of the temperature lower than that of the large scale GC plasma. The 6.97 keV/6.67 keV flux ratio at the position (3, 2) is 0.14, which can be converted to the ionization temperature to be 4 keV. This temperature is typical to a young SNR like Sgr A East.

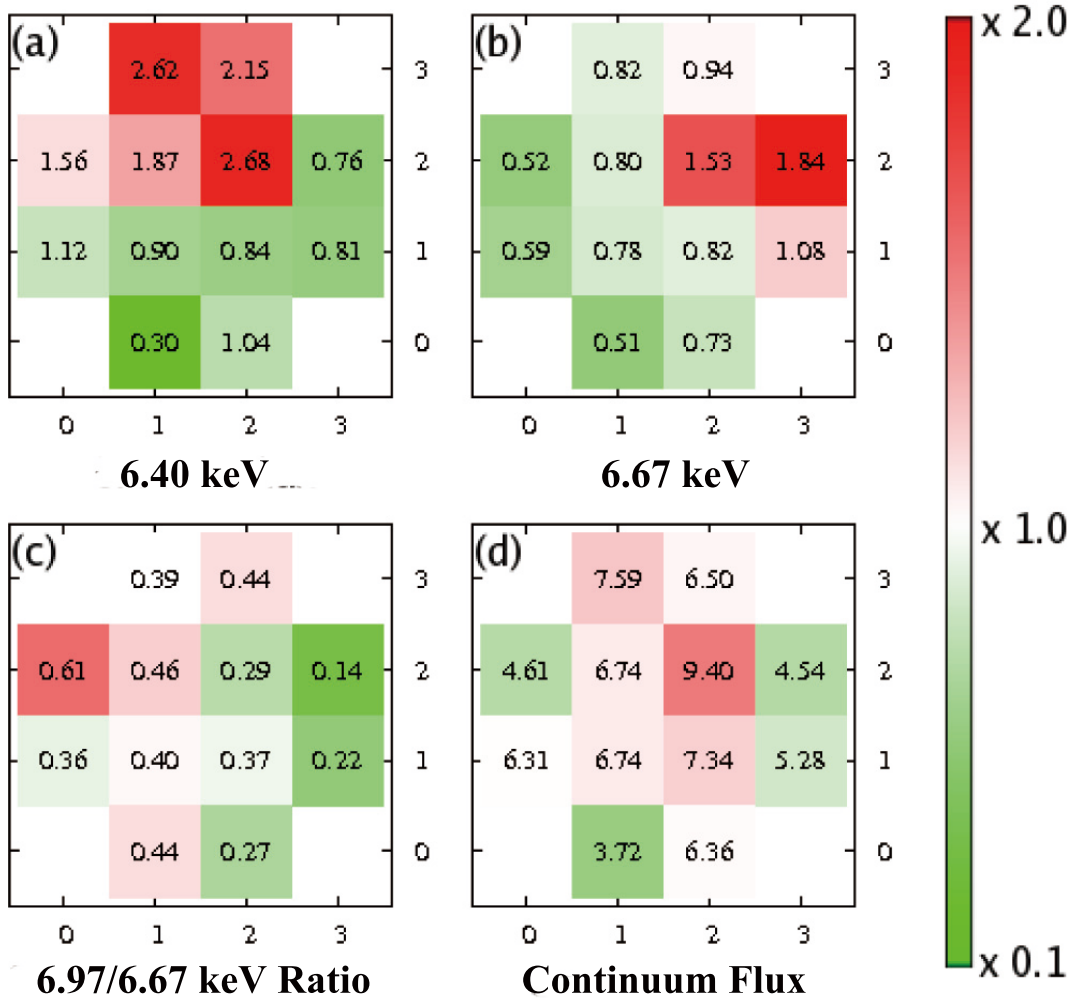


Figure 5.2: Fluxes of the 6.40 keV (a) and the 6.67 keV lines (b), the flux ratio of 6.97 keV/6.67 keV (c), and the continuum flux (normalization of the 7-keV bremsstrahlung) map (d). The embedded numbers are fluxes in units of 10^{-6} photons $\text{cm}^{-2} \text{s}^{-1} \text{arcmin}^{-2}$ or flux ratios. The color means that the average value is white, and the increasing (decreasing) excess above (below) the average is given with increasing deepness of red (green), where the maximum (minimum) is 2.0 (0.1) times of the average value.

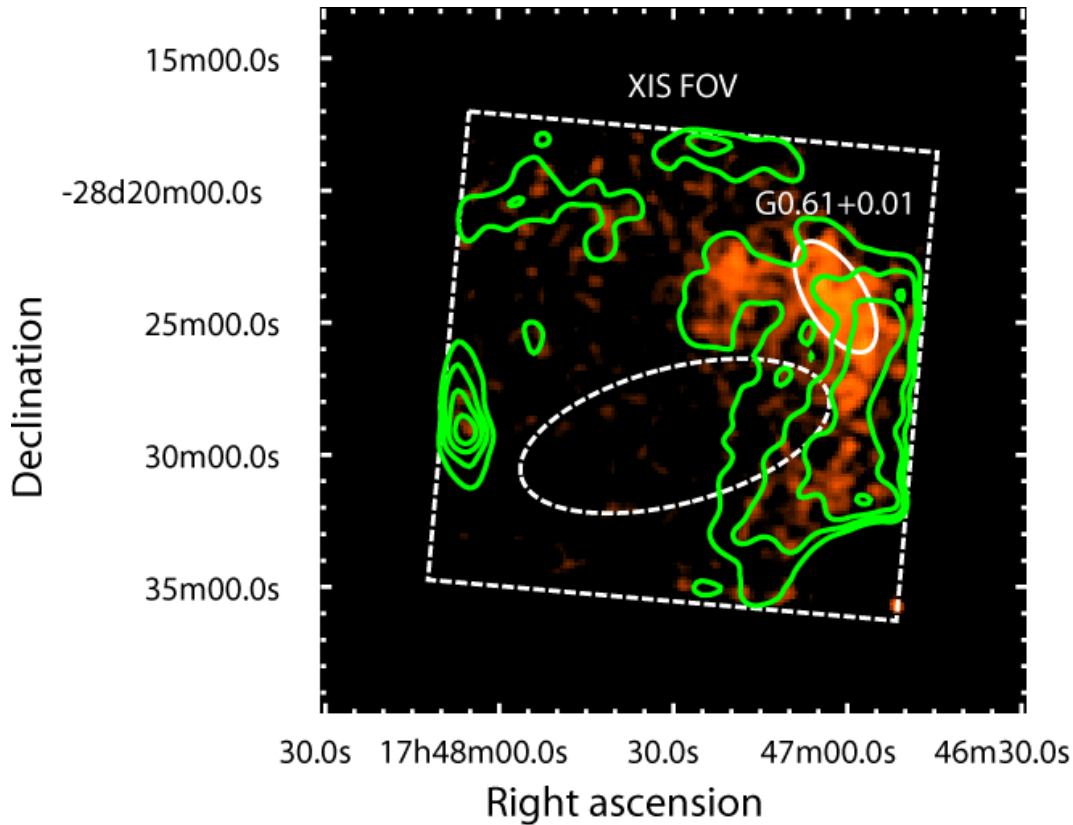


Figure 5.3: The 6.67 keV line map (the 6.58–6.74 keV band map) showing bright spot at the northwest corner with the 2–5 keV continuum map as green contours. The fluxes are normalized by the 6.7 keV flat-field image. The source and background regions are shown by the white solid and dotted ellipses, respectively.

The 6.40 keV fluxes (figure 5.2a) shows local excesses at the position of Sgr B2 (2, 2) and the east of Sgr B2 (1, 3). The presence of 6.40 keV is strong evidence for dense and cool molecular clouds.

5.2 New Diffuse Sources

5.2.1 SNR Candidate — G 0.61+0.01

We made a narrow band image of 6.67 keV (the 6.58–6.74 keV band) in figure 5.3. We see a clear 6.67 keV flux excess at the northwest corner. To confirm the 6.67 keV excess, we referred to the Chandra and XMM-Newton data with long exposure time (shown in figure 5.4). Since the energy resolution of the Chandra ACIS is limiting in the separation of the 6.40 and 6.67 keV lines, it is unclear whether the 6.67 keV source is present or not. The XMM image in the 6.67 keV band shows

a clear elongated structure near the same position. Accordingly the presence of the 6.67 keV line source is certain. On the other hand, the continuum band image (shown as green contours in figure 5.3) shows only a hint of enhancement, and shows no clear structure. This source is therefore very peculiar, being dominant only in the 6.67 keV line. Since the dominance of the 6.67 keV line suggests that the excess is a new SNR (see also the discussion below), we designate this source Suzaku J1747.0–2824.5 (G 0.61+0.01) from its center position.

We made the NXB-subtracted spectra of the SNR from the region indicated by the solid ellipse in figure 5.3 for both the three FI CCDs (XIS0, XIS2 and XIS3 are co-added) and one BI CCD (XIS1). In these spectra, the cosmic X-ray background (CXB) and GCDX are still included. We therefore made the NXB-subtracted spectra for the region indicated by the dotted ellipse, and subtracted this local background (CXB + GCDX) from the source spectrum. All the spectra have been corrected for the vignetting at 6.67 keV. The results are given in figure 5.5, for the FIs and BI, separately. We see a pronounced peak at 6.67 keV, but not at 6.97 keV. The 6.67 keV line shape is asymmetric with a tail at lower energy. In order to verify the line structure, we derive fluxes of the 6.40, 6.67 and 6.97 keV lines ($K\alpha$ line of FeI, XXV and XXVI) in the source and the background regions, by applying a phenomenological model (a bremsstrahlung continuum and many Gaussian lines) in the raw data (no background subtraction). The resulting 6.40, 6.67 and 6.97 keV line fluxes are 2.22 ± 0.22 , 5.17 ± 0.52 and 0.48 ± 0.05 for the G0.61+0.01 (source) region, and 0.61 ± 0.06 , 0.68 ± 0.07 and 0.30 ± 0.03 for the background region, where the flux unit is 10^{-6} photons cm^{-2} s^{-1} arcmin^{-2} . In contrast to the 6.67 keV line, we see no significant excess in the 6.97 keV line from the source region compared to the background region. Thus we confirm that G 0.61+0.01 emits strong 6.67 keV line, but very weak 6.97 keV line. The small excess of the 6.40 keV line makes the low energy tail in the 6.67 keV line.

The FI and BI spectra are simultaneously fitted with a plane parallel shock model (VPSHOCK in the XSPEC package) adding two Gaussian lines at 6.40 keV and 7.06 keV. These two lines represent the $K\alpha$ and $K\beta$ lines of FeI, where the flux of latter line is fixed at 12.5% of the flux of the former line (Kaastra & Mewe 1993). The best-fit results and parameters are shown in figure 5.5 and table 5.1. Although we detected the 6.40 keV line from G 0.61+0.01, it is very difficult to judge whether this line is really attributable to G 0.61+0.01, due to spilled-over flux from the adjacent source Sgr B2, or due to a fluctuation of a larger scale structure in the 6.40 keV line. As for the last possibility, we see a large scale 6.40 keV enhancement

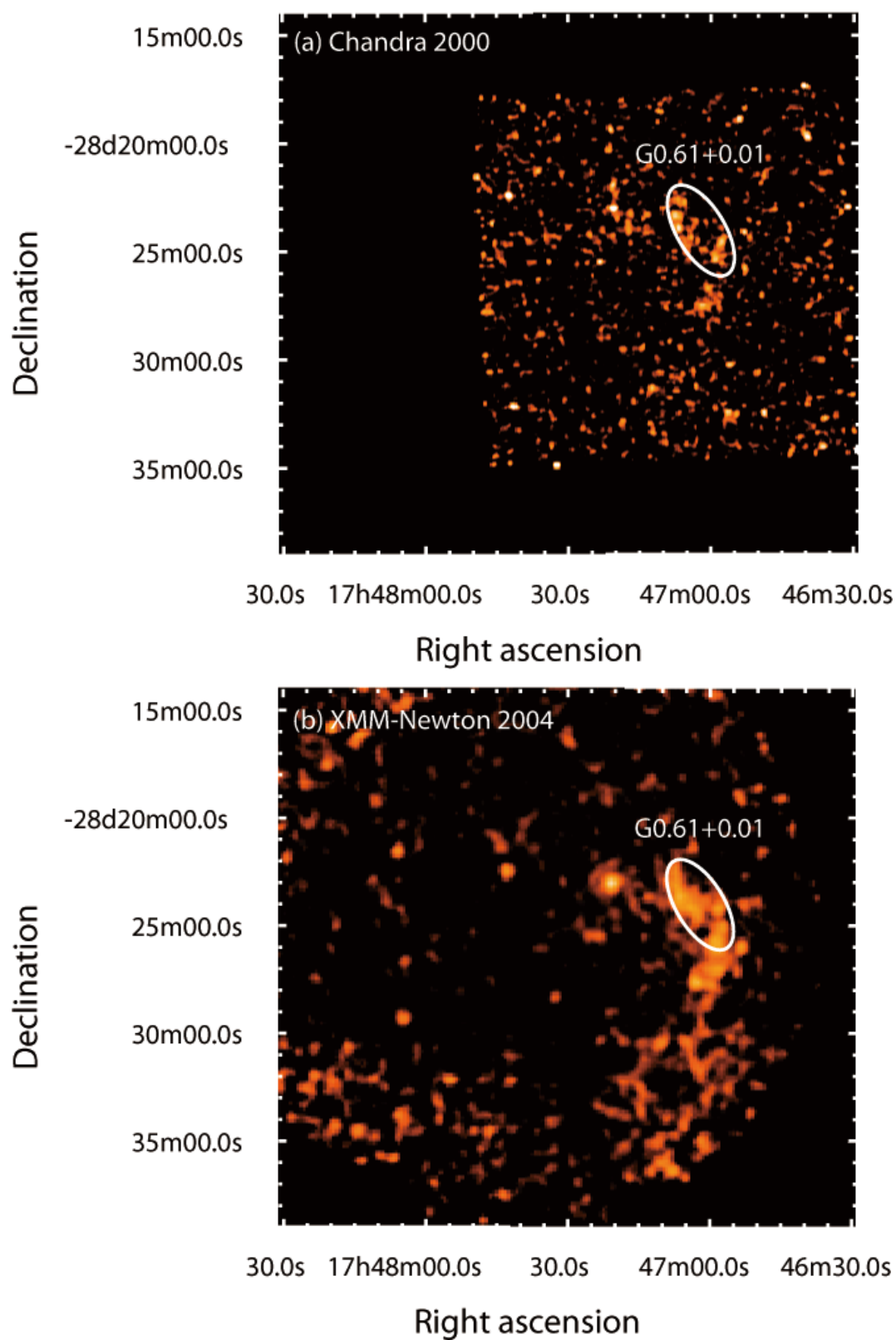


Figure 5.4: The exposure corrected 6.67 keV line maps of (a) Chandra 2000 and (b) XMM-Newton 2004. The source regions are shown by the solid circles.

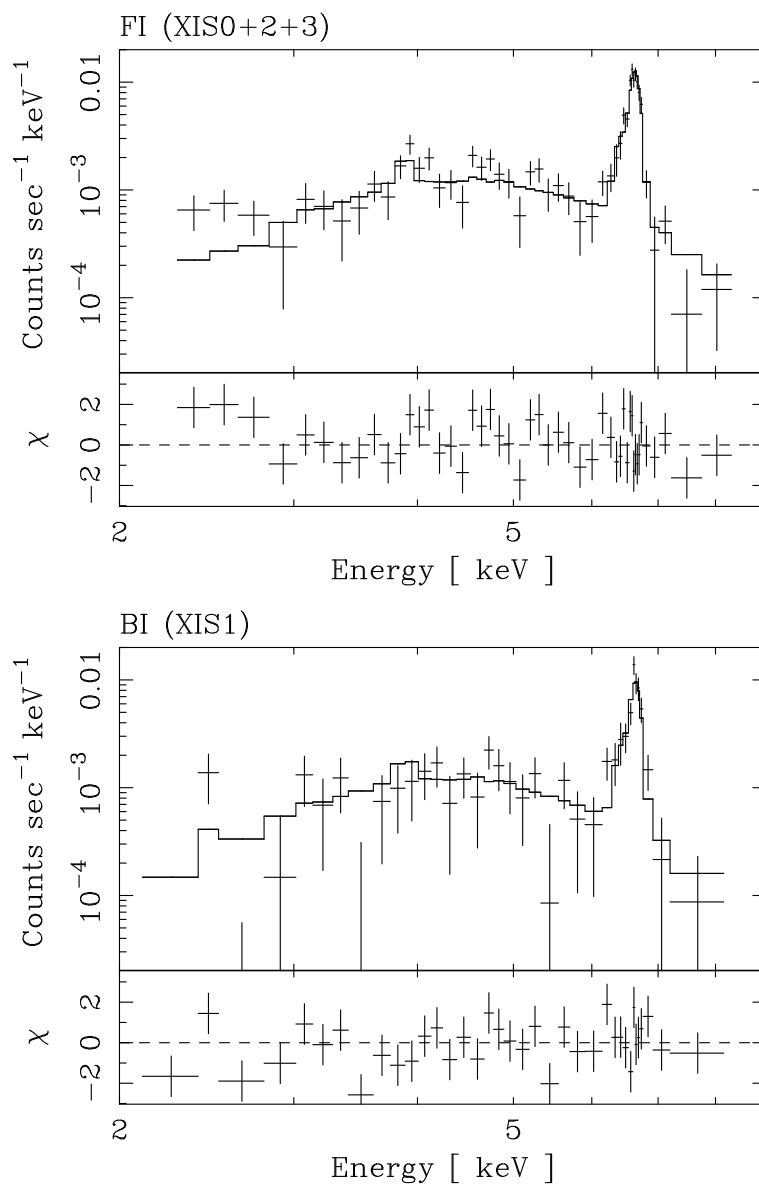


Figure 5.5: Top: the X-ray spectrum of the sum of 3 FI CCDs (XIS0, 2 and 3) for the new SNR (G 0.61+0.01) with the best-fit VPSHOCK model. Bottom: same as the top, but of the BI CCD (XIS1).

Table 5.1: The best-fit parameters for G 0.61+0.01 with the VPSHOCK model plus two emission lines

Parameter	Value
N_{H} (10^{23} H cm $^{-2}$)	$1.6^{+0.7}_{-0.4}$
kT (keV)	$3.2^{+2.3}_{-0.9}$
$n_e t$ (10^{11} cm $^{-3}$ s)	$1.9^{+4.7}_{-0.8}$
Abundances*	
Ca	$3.5^{+3.1}_{-2.4}$
Fe	$5.1^{+1.2}_{-1.1}$
Neutral iron lines ^a	
$I_{6.40}$ (10^{-6} photons cm $^{-2}$ s $^{-1}$)	$5.1^{+2.4}_{-2.5}$
$I_{7.06}$ (10^{-6} photons cm $^{-2}$ s $^{-1}$)	0.6
Flux and Luminosity	
F_{2-10}^{\dagger} (10^{-13} ergs cm $^{-2}$ s $^{-1}$)	$7.5^{+1.1}_{-2.2}$
L_{2-10}^{\ddagger} (10^{34} ergs s $^{-1}$)	$1.5^{+0.1}_{-0.2}$
χ^2/dof	99.0/78

Note—The uncertainties indicate the 90% confidence limit.

* The elements which are not listed are fixed at 1.0 (solar ratio).

^a The line energy of $K\alpha$ and $K\beta$ is fixed at the theoretical value (6.40 and 7.06 keV, respectively; Kaastra and Mewe 1993) and the intensity of $K\beta$ is fixed at 12.5% (Kaastra and Mewe 1993) of that of $K\alpha$.

[†] Observed flux in the 2.0–10.0 keV band.

[‡] Absorption corrected luminosity in the 2.0–10.0 keV band.

in the northwest compared to the background region in the southeast (see figure 5.6). In any case, we ignore this line in the discussion of G 0.61+0.01 because the 6.40 keV line flux is only 3% of that in Sgr B2 (see tables 5.1 and 5.3). Since the Suzaku spatial resolution is not good enough, there may be possible contamination of unresolved point sources. To check this problem, we searched for point sources using the Chandra archival data and found no point source in the source region. On the other hand, in the background region, there are 48 point sources. The total flux in the 2–10 keV band is 5×10^{-13} ergs cm^{-2} s^{-1} , which is only $\sim 2\%$ of the CXB + GCDX flux of 2.6×10^{-11} ergs cm^{-2} s^{-1} , and hence can be ignored in the present data analysis and discussion.

The best-fit temperature of ~ 3 keV and the over-abundance of Fe are consistent with an ejecta of a SNR and are similar to those found in the central region of Sgr A East, a young SNR near the GC. The high temperature component of Sgr A East is $kT \sim 4\text{--}6$ keV (Sakano et al. 2004; Park et al. 2005; Koyama et al. 2007c), and iron is over-abundant by a factor of 4–5 (Maeda et al. 2002; Sakano et al. 2004; Park et al. 2005; Koyama et al. 2007c). Thus G 0.61+0.01 is likely an ejecta dominant central region of an SNR. We note that Sgr A East has a low-temperature component of about 1 keV, while G 0.61+0.01 has not. The absence of the low-temperature plasma may be due to the large absorption. The N_{H} value of 1.6×10^{23} H cm^{-2} is larger than that of the typical value to the GC (6×10^{22} H cm^{-2}) (Sakano et al. 2002). Therefore, G 0.61+0.01 could be located behind or at the rim of the Sgr B2 cloud. Since G 0.61+0.01 is located in the south of an expanding radio shell (Oka et al. 1998), which is probably interacting with the Sgr B2 cloud rim, we regard that the distance of G 0.61+0.01 is the same as that of Sgr B2 and is assumed to be 8.5 kpc (Reid et al. 1988). Then the 2–10 keV band luminosity is estimated to be 1.5×10^{34} ergs s^{-1} , which is typical for an ejecta plasma of an SNR. The size of G 0.61+0.01 (the solid ellipse in figure 5.3) is $2.2' \times 4.8'$, which corresponds to $5.5 \text{ pc} \times 12 \text{ pc}$ at a distance of 8.5 kpc. Assuming the plasma emission is due to a uniform density ellipsoid with the 3-axis radii of 2.7 pc, 2.7 pc and 6 pc, we estimate physical parameters of G 0.61+0.01 (table 5.2). Although the iron abundance is 3–4 times the solar value, the total mass of protons are much larger than those of irons. We therefore assume that electron density (n_e) is equal to the proton density (n_p), and that protons carry most of the plasma mass (m_p). Dividing the radius of the major axis (6 pc) by the sound velocity of the 3.2 keV plasma ($v = 1.4 \times 10^8$ cm s^{-1}), we obtain the dynamical time scale (t_{dyn}) of $\sim 4 \times 10^3$ years. If, instead, we use the ionization parameter ($n_e t$) and electron density (n_e), then the ionization time

Table 5.2: The physical parameters of G 0.61+0.01

Parameter	Value
Emission measure (EM) ^a (cm ⁻³)	1.4×10^{57}
The electron density n_e ^b (cm ⁻³)	0.9
Total mass M ^c (M_\odot)	1.3
Thermal energy E ^d (ergs)	2.4×10^{49}
The dynamical time scale t_{dyn} ^e (s)	1.3×10^{11}
The ionization time scale t_{ioni} ^f (s)	2.1×10^{11}

Note—The plasma is assumed to be a uniform density ellipsoid with the 3-axis radii of 2.7 pc, 2.7 pc and 6 pc (see text).

^a $\text{EM} = n_e n_H V$, where n_e and n_H are the electron and hydrogen density.

^b derived from EM assuming that n_e and n_H are equal.

^c $M = n_e m_p V$, where m_p is the proton mass and V is the plasma volume.

^d $E = 3n_e kTV$.

^e derived from the radius of the major axis of the plasma ellipsoid divided by the sound velocity of the ~ 3 keV plasma.

^f derived from the ionization parameter (see table 5.1) divided by the electron density.

scale (t_{ioni}) is estimated to be $\sim 7 \times 10^3$ years. Since the source size of $2.2' \times 4.8'$ is comparable to the half power diameter ($\sim 2'$), the real size of G 0.61+0.01 must be smaller. Therefore the quoted value of $t_{\text{dyn}} \sim 4 \times 10^3$ years should be an upper limit. That of $t_{\text{ioni}} \sim 7 \times 10^3$ years is also an upper limit, because n_e is inversely proportional to the square root of the plasma volume. Thus the age of G 0.61+0.01 is probably younger than 7×10^3 years.

Another possibility is that G 0.61+0.01 is a part of a larger SNR. Since G 0.61+0.01 is found at the edge of the XIS field, other parts of a candidate SNR may be out of the XIS field. In this scenario, G 0.61+0.01 may be a part of the expanding radio shell discovered by Oka et al. (1998). The kinetic energy of the radio shell is a few times 10^{52} erg s⁻¹, which is within the range of a single or multiple supernova explosions. Thus follow-up X-ray observations including this expanding radio shell is highly required.

5.2.2 XRN Candidate — M 0.79–0.09

We have made a narrow band image at 6.40 keV (the 6.33–6.46 keV band) in figure 5.6. We see two bright spots in the north. One is the “Sgr B2 cloud” which has been already found as a strong 6.40 keV source (Koyama et al. 1996), and the other

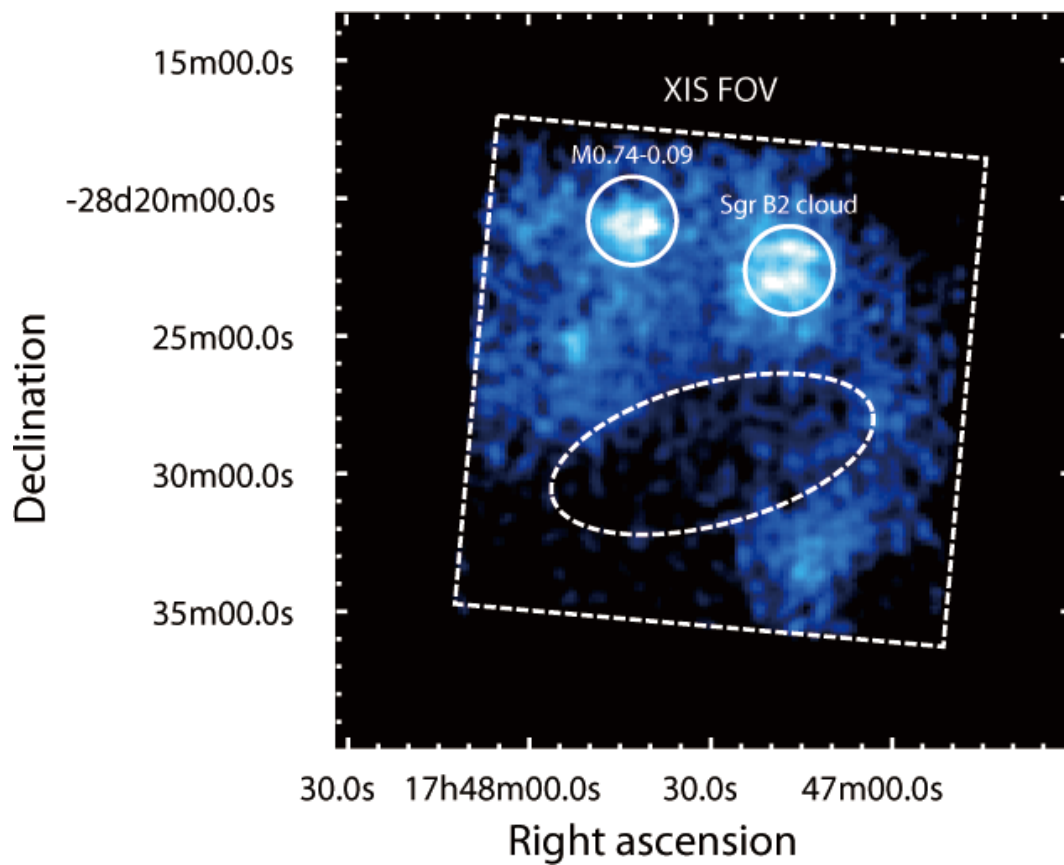


Figure 5.6: The 6.40 keV line map (the 6.33–6.46 keV band map) showing bright spots at the Sgr B2 cloud and M 0.74-0.09. The fluxes are normalized by the 6.40 keV flat-field image. The sources and background regions are shown by the solid circles and dotted ellipse, respectively.

is a newly discovered source. We again referred to the same data of Chandra and XMM as in the case of G 0.61+0.01 (shown in figure 5.7). In the Chandra data, this excess is found near the edge of the ACIS FOV. The XMM data show a clear excess near this source. The presence of the 6.40 keV line supports the presence of cool and dense gas clouds. We therefore designate this new source as Suzaku J1747.7–2821.2 (M 0.74–0.09) from its peak position. We also rename Sgr B2 cloud to M 0.66–0.02 to avoid the confusion between the whole area and the individual molecular cloud. We made X-ray spectra of M 0.66–0.02 and M 0.74–0.09 from the circles given in figure 5.6, for comparison. The background spectrum is made from the dotted ellipse and subtracted in the same procedure as in the case of G 0.61+0.01.

The background-subtracted spectra are shown in figures 5.8 and 5.9. We simultaneously fit the FIs and BI spectra with a model of absorbed power-law plus two Gaussians near 6.40 and 7.06 keV, which are for the $K\alpha$ and $K\beta$ lines of Fe I. The best-fit parameters are shown in table 5.3. This model nicely fits the data except for an excess near the 6.67 keV line in the M 0.66–0.02 spectra. In fact, the 6.67 keV line map (figure 5.3) shows a weak enhancement at the position of M 0.66–0.02. One possibility is that the 6.67 keV enhancement is a part of the new SNR candidate G 0.61+0.01, because it is located in the close vicinity of M 0.66–0.02. The other possibility is that the 6.67 keV enhancement is due to the young stellar objects (YSOs) embedded in the center of M 0.66–0.02. In fact, this region is relatively crowded with the Chandra point sources (13 point sources), and at least some of them are YSOs with a hint of the 6.67 keV line emission (Takagi et al. 2002). The total flux (in the 2–10 keV band) of the point sources is $\sim 10^{-13}$ ergs cm^{-2} s^{-1} , which is $\sim 6\%$ of the M 0.66–0.02 flux (see table 5.3).

The M 0.66–0.02 (Sgr B2 cloud) has been studied extensively with ASCA and Chandra. Koyama et al. (1996) and Murakami et al. (2001) concluded that the 6.40 keV emission is due to fluorescence by strong X-rays coming from Sgr A*, hence named the X-ray reflection nebula (XRN). In this paper, we found a clear $K\beta$ line at 7.06 keV with consistent flux ratio to the $K\alpha$ line (6.40 keV) in the fluorescent X-ray origin and a deep Fe edge at 7.1 keV. These discoveries provide additional supports for the XRN scenario of Sgr B2.

For the M 0.74–0.09 region, Miyazaki & Tsuboi (2000) reported flux peaks of the CS ($J=1-0$) line emission at $(l, b) = (0^\circ 761, -0^\circ 117)$ and $(0^\circ 764, -0^\circ 064)$, which is clear evidence for the presence of a molecular cloud. The XIS spectrum of this region exhibits a strong 6.40 keV line with an equivalent width of 1.6 keV, a 7.06 keV line and an Fe edge structure at 7.1 keV (see table 5.3). All these features are consistent

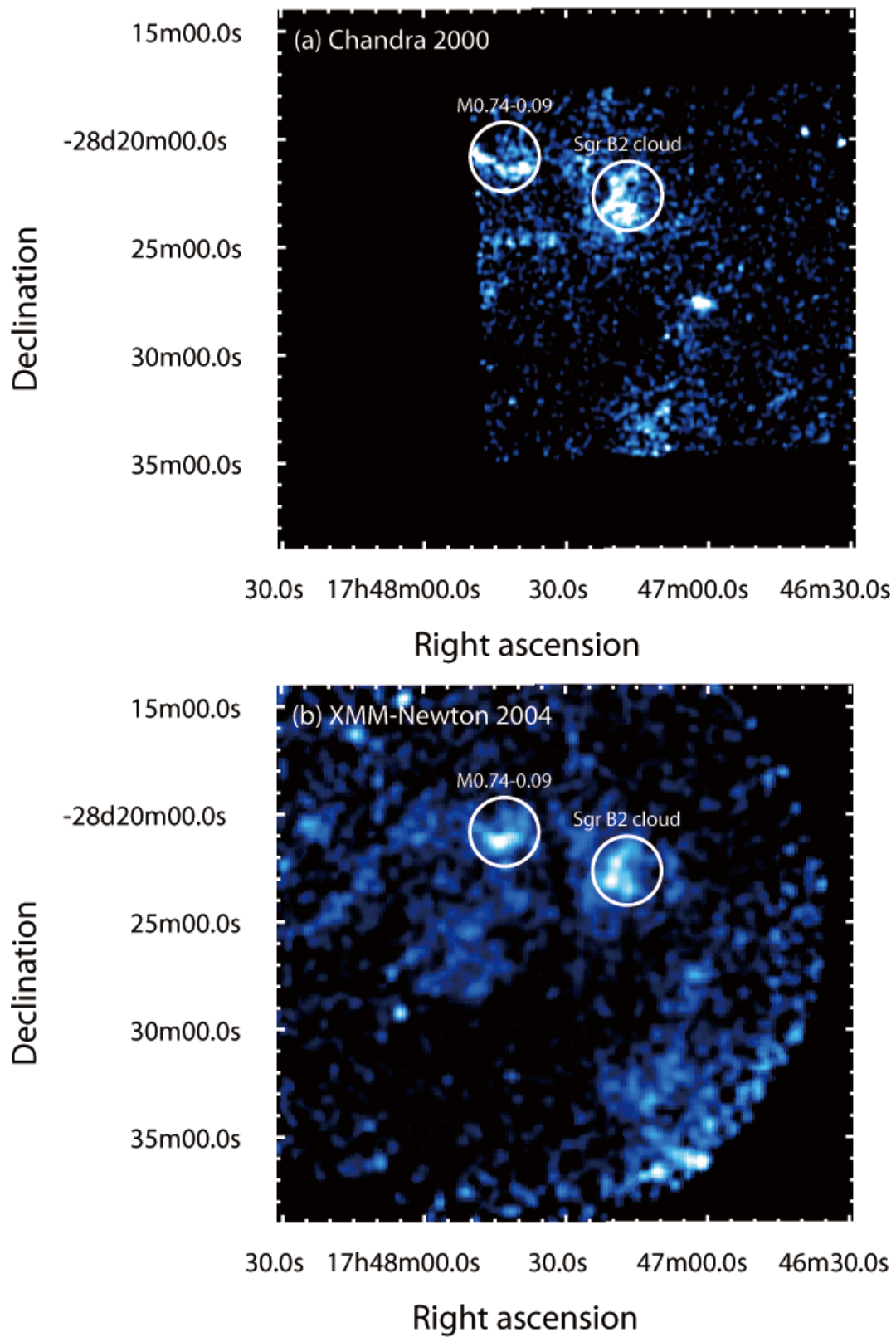


Figure 5.7: The exposure corrected 6.40 keV line maps of (a) Chandra in 2000 and (b) XMM-Newton in 2004. The source regions are shown by the solid circles.

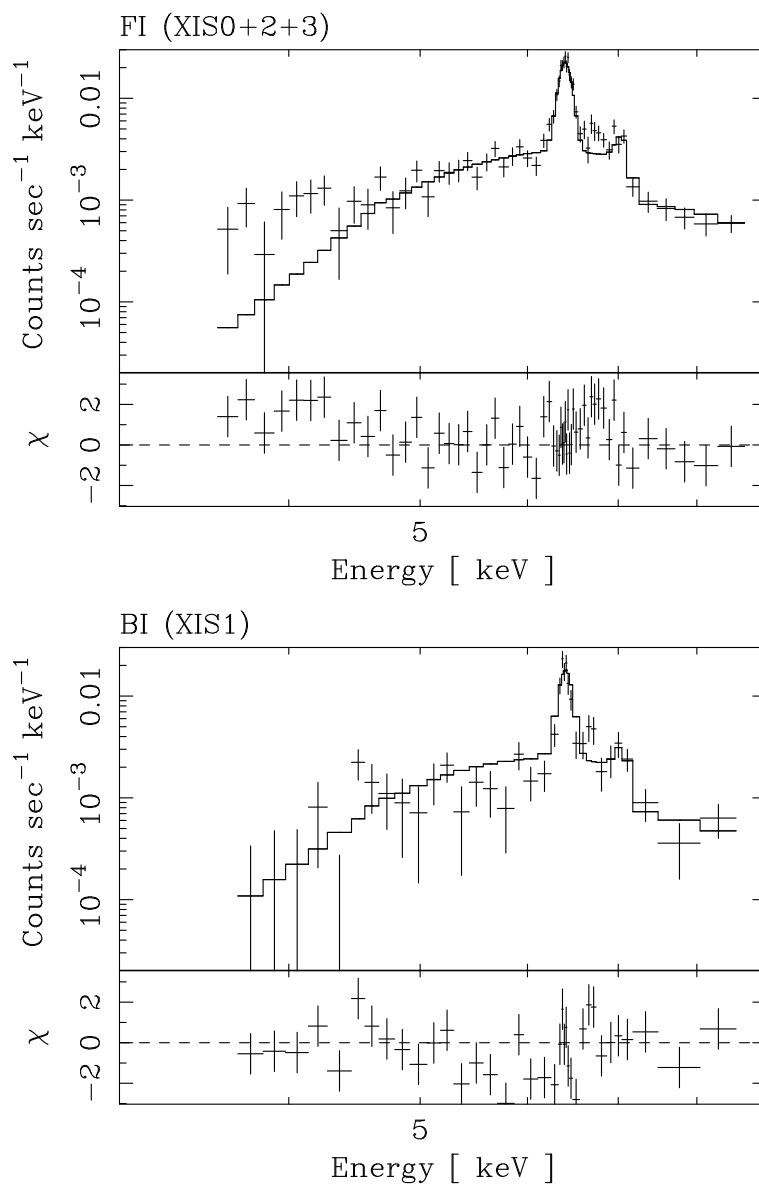


Figure 5.8: Top: the X-ray spectrum of the sum of the 3 FI CCDs (XIS0, 2 and 3) for M0.66–0.02 (Sgr B2 cloud) with an absorbed power-law model and two Gaussian lines. Bottom: same as the top but of the BI CCD (XIS1).

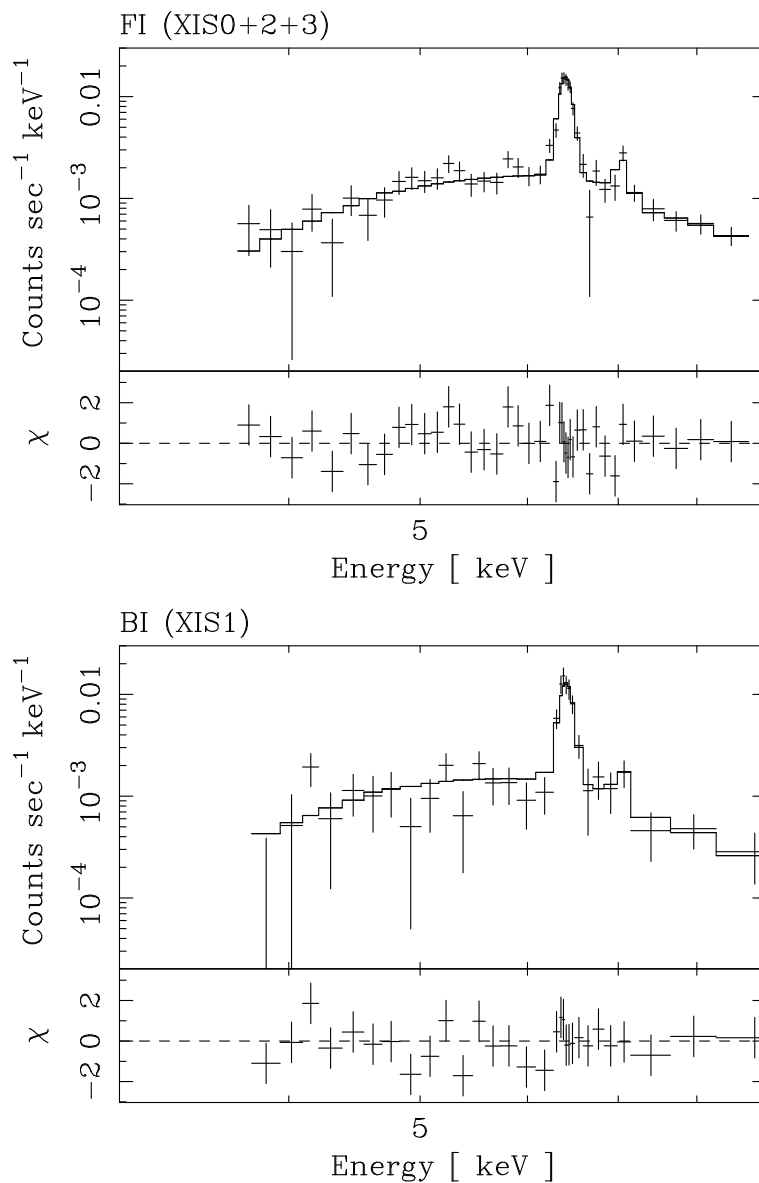


Figure 5.9: Same as figure 5.8, but for a new source M0.74-0.09.

with being from $K\alpha$, $K\beta$ and K-edge from FeI. The flux of the 7.06 keV line is about 10% of that of the 6.40 keV line, which is also consistent with the fluorescent X-ray origin (Kaastra & Mewe 1993). We note here that the background region is the same as in the case of G 0.61+0.01. With the same argument in section 5.2.1, possible point source contribution can be ignored.

Unlike M 0.66–0.02, no hint of YSOs is found so far. No bright point source is found in the Chandra image. Therefore, the X-rays cannot be the scattering and fluorescence by embedded YSOs. If the X-rays from M 0.66–0.02 and M 0.74–0.09 are due to the Thomson scattering and fluorescence of the same irradiating external source like Sgr A*, then the N_{H} ratio between M 0.66–0.02 and M 0.74–0.09 should be similar to their 6.40 keV line flux ratio. The observed N_{H} ratio is 0.42, while that of the 6.40 keV line flux is 0.36, in good agreement of the fluorescence scenario by a single irradiation source. Therefore the XRN scenario by past activity of Sgr A*, which was successfully applied to M 0.66–0.02, may also be applied to M 0.74–0.09.

A different scenario than the XRN is that the 6.40 keV line emission is produced by the collision of electrons. As we reviewed in section 2.3, the cross section of iron K-shell ionization is maximum at the electron energy of a few times 10 keV. Thus the most probable source is from low energy electrons (LEE) as proposed for the origin of the Galactic Ridge iron K-shell emission (Valinia et al. 2000). Since a few 10 keV electrons are absorbed in less than 10^{22} H cm⁻² of depth, the produced X-ray spectrum should have no significant absorption edge. Our observation, however, shows a clear absorption of $(4.0\text{--}9.6) \times 10^{23}$ H cm⁻², in far excess of the Galactic interstellar absorption (Sakano et al. 2002). Thus the LEE origin is unlikely, unless we assume a special geometry such that the 6.40 keV source is deep in or behind the dense cloud.

Table 5.3: The result of spectral fittings of M0.66–0.02 (Sgr B2 cloud) and M0.74–0.09 with a power-law and two Gaussian models.

Parameter	M0.66–0.02 (Sgr B2 cloud)	M0.74–0.09
Absorbed power-law model:		
Column density N_{H} (10^{23} cm $^{-2}$)	$9.6^{+2.5}_{-0.8}$	$4.0^{+1.4}_{-1.1}$
Photon index Γ	$3.2^{+0.9}_{-0.6}$	$1.4^{+0.4}_{-0.7}$
Gaussian 1 (FeI K α):		
Line energy (eV)	6399^{+5}_{-5}	6406^{+6}_{-6}
Intensity (10^{-5} photons cm $^{-2}$ s $^{-1}$)	$16.5^{+0.8}_{-0.3}$	$5.9^{+1.4}_{-1.0}$
Equivalent Width (keV)	1.13	1.55
Gaussian 2 (FeI K β):		
Line energy (eV) ^a	7057	7064
Intensity (10^{-5} photons cm $^{-2}$ s $^{-1}$)	$1.4^{+0.5}_{-0.5}$	$0.6^{+0.3}_{-0.3}$
Equivalent Width (keV)	0.13	0.18
Observed flux [†] (10^{-12} ergs cm $^{-2}$ s $^{-1}$)	$1.5^{+0.1}_{-0.9}$	$1.3^{+0.2}_{-0.8}$
Luminosity [‡] (10^{34} ergs s $^{-1}$)	$9.7^{+0.1}_{-5.1}$	$2.6^{+0.4}_{-0.9}$
χ^2/dof	154.7/89	54.4/66

Note—The uncertainties indicate the 90% confidence limit.

^a The energy gap between K α and K β is fixed at the theoretical value (+658 eV) (Kaastra and Mewe 1993).

[†] Observed flux in the 4.0–10.0 keV band.

[‡] Absorption corrected luminosity in the 4.0–10.0 keV band.

Chapter 6

Result II — Time Variabilities of Neutral Iron Line

6.1 Spectral Analysis and Error Estimation

The determination of the iron line fluxes is influenced by a continuum model and a background. In order to estimate the flux errors caused by models and backgrounds, we make a comparison analysis for the whole Sgr B2 region. Figure 6.1 shows relevant diffuse sources in the Sgr B2 complex overlaid on the XMM-Newton 6–7 keV image. Since the FOVs and pointing positions of the Suzaku, Chandra, XMM-Newton and ASCA observations are slightly different from each other, we selected a region in which all the observed areas overlapped (referred to hereafter as the Sgr B2 region). The Sgr B2 region (the overlapping region) is indicated by the solid squares in figure 6.1. The subsequent data analysis and discussion are based on the sources in the Sgr B2 region. Hereafter, we refer to the Sgr B2 cloud as M0.66–0.02. G0.61+0.01 is a new source with a strong 6.67 keV line, hence possibly a new young SNR (Koyama et al. 2007b). G0.570–0.0018 is an unusual diffuse source discovered by Senda et al. 2002. M0.74–0.09 is also a new 6.40 keV source, but it is not discussed in this paper, because it is outside of the Sgr B2 region.

We extracted X-ray spectra from the Sgr B2 region and subtracted the off-plane blank-sky regions. Thus, the CXB and NXB were subtracted but the GCDX were not subtracted. As the off-plane blank-sky, we selected the north ecliptic pole data for XIS, distributed blank-sky databases for MOS and ACIS, and Lockman hole data for PN and SIS.

The blank-sky-subtracted spectra are shown in figure 6.2. These spectra exhibit continuum emissions and pronounced peaks due to Fe I $K\alpha$ (6.40 keV), Fe XXV $K\alpha$

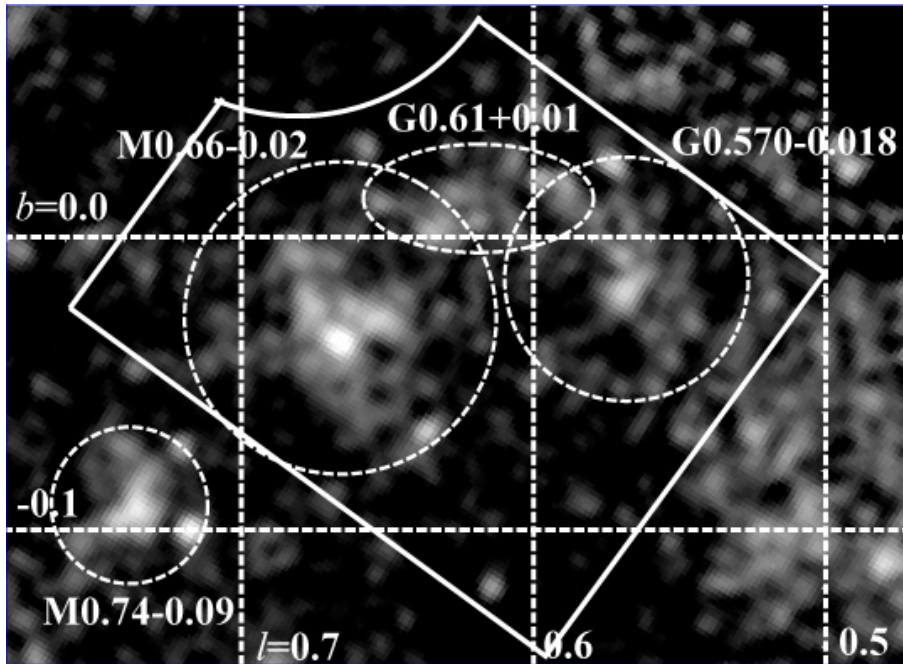


Figure 6.1: The XMM-Newton image in 6–7 keV band. The source region for the Sgr B2 region is described in a solid line. Dashed line circles are individual sources discovered in this region.

(6.67 keV), and the composite of Fe XXVI $K\alpha$ (6.96 keV) and Fe I $K\beta$ (7.06 keV). The continuum emission is composed of: 1) the continuum of the GCDX (Koyama et al. 2007d), 2) the continuum (thermal bremsstrahlung) from G 0.61+0.01, a new SNR in this region (Koyama et al. 2007b), and 3) a non-thermal power-law continuum with a deep iron K-edge related to the 6.40 keV line (Koyama et al. 1996).

It is practically impossible to resolve these three continuums; we therefore represented these three continuum by a single power-law continuum with absorption (the `wabs*power-law` model in the `xspec` code). We then added four K-shell lines by Gaussian functions. These are the Fe XXV $K\alpha$ (~ 6.67 keV) and Fe XXVI $K\alpha$ (~ 6.96 keV) lines due to the GCDX, and Fe I $K\alpha$ (6.40 keV) and Fe I $K\beta$ (7.06 keV) lines due mainly to the Sgr B2 region. Thus, the model spectrum in the `xspec` code is given as;

`wabs*power-law + 4 Gaussians.`

6.1.1 Suzaku

The spectra of the Sgr B2 region and background subtractions of the blank sky for XIS0, 1, 2 and 3 were performed separately, however all the FI-CCD spectra (XIS0,

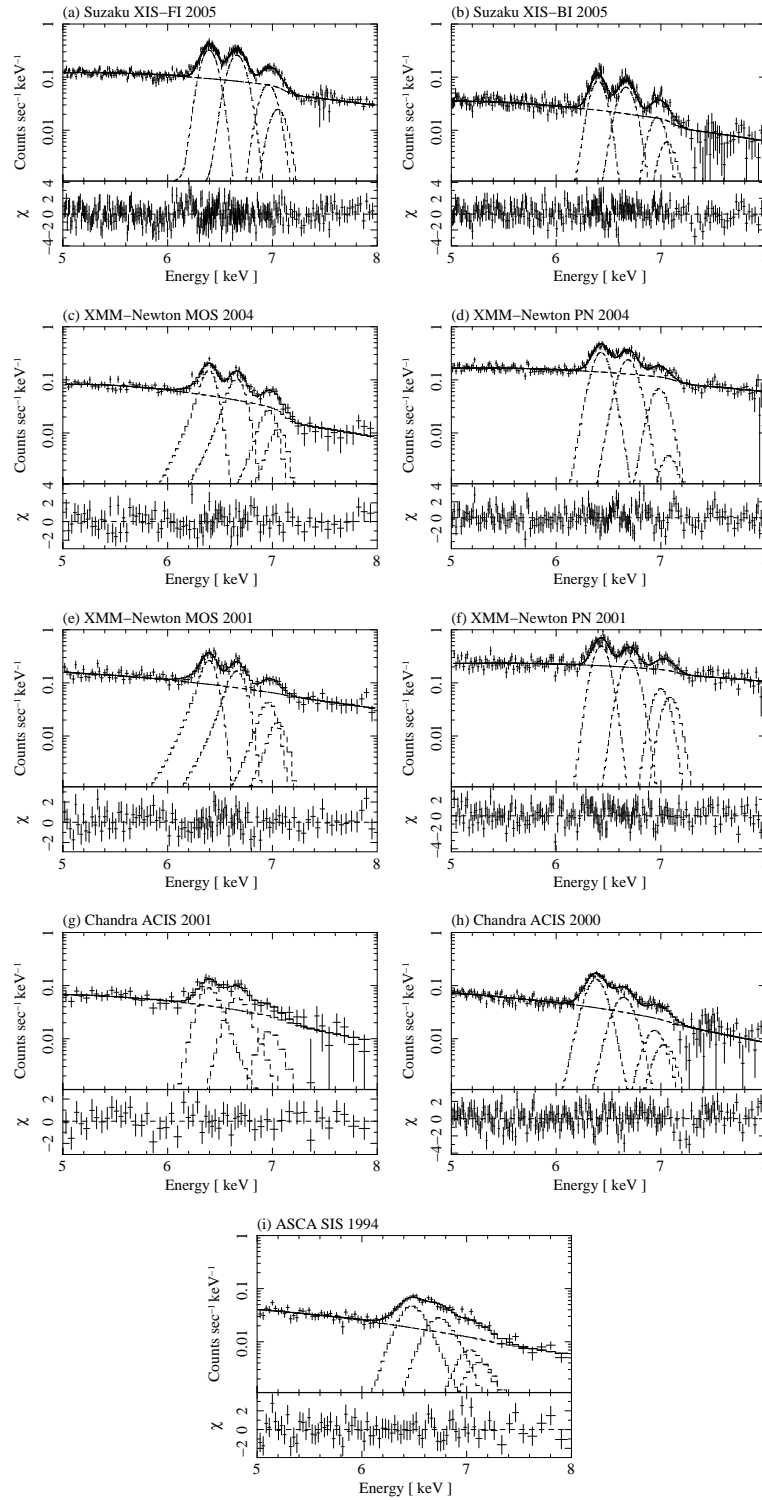


Figure 6.2: The blank-sky-subtracted spectra of the Sgr B2 region, with the Suzaku XIS FI sensors (a) and BI sensor (b) in 2005, XMM-Newton MOS (c) and PN (d) in 2004, (e) and (f) in 2001, Chandra ACIS-I (g) in 2001 and (h) in 2000, and ASCA SIS (i) in 1994. The solid lines indicate the best-fit models (see text).

1 and 3) were combined, because their response functions are almost identical with each other. We fitted the FI-CCD and BI-CCD spectra simultaneously in the energy band of 5–8 keV with the model given by equation (1). All the parameters were free under the following constraints: the line widths were fixed to be 0 eV except that of the Fe XXV $K\alpha$ line (Koyama et al. 2007d), and the energy interval between Fe I $K\alpha$ (6400 eV) and $K\beta$ (7058 eV) was fixed at the theoretical value of 658 eV (Kaastra & Mewe 1993). The best-fit spectra for the FI and BI are shown in figures 2(a) and 2(b) respectively, while the best-fit parameters are listed in table 6.1.

Although the K-shell lines from highly ionized iron, the Fe XXVI $K\alpha$ and Fe XXV $K\alpha$ lines are due to the largely extended GCDX, the best-fit center energy of the Fe XXVI $K\alpha$ line (6665 eV) and the flux ratio of Fe XXVI $K\alpha$ to Fe XXV $K\alpha$ (0.30) are slightly smaller than those (6680 eV and 0.34, respectively) found in the GC region (Koyama et al. 2007d). This may be due to the contamination of a strong Fe XXV $K\alpha$ line of a new SNR G 0.61+0.01 (Koyama et al. 2007b).

When fitting the XMM-Newton, Chandra and ASCA spectra, we fixed the line centroids and the $K\alpha$ flux ratio of Fe XXVI and Fe XXV to the best-fit Suzaku values given in table 6.1, because the statistics and energy response of these satellites were limited compared to Suzaku.

Then we defined four types of powerlaw continuum models as follows,

Model I Absorption column density N_{H} and powerlaw index Γ are left free.

Model II N_{H} is a free parameter but Γ is fixed at the Suzaku value.

Model III N_{H} is fixed at the Suzaku value and Γ is free.

Model IV N_{H} and Γ are fixed at the Suzaku values.

With these four continuum models, we operated line flux estimations on the other spectra.

6.1.2 XMM-Newton

At first, we fitted the MOS and the PN spectra independently with all parameters free (predefined as Model I). Since the lines and edge structure cannot be fitted well for the PN spectra, we therefore added some systematic gain offsets.

Then we used Model II–IV and fit the spectra. The best-fit parameters are shown in table 6.2 and 6.3. The line fluxes are consistent within 10% among the models, which is comparable with statistical errors.

Table 6.1: The Suzaku result of spectral fitting for the Sgr B2 region

Suzaku 2005 XIS	
—Continuum—	
(1) N_{H} (10^{23} H cm $^{-2}$)	$3.0^{+0.3}_{-0.5}$
(2) Γ	$2.6^{+0.2}_{-0.2}$
(3) F_{pow} (10^{-4} photons cm $^{-2}$ s $^{-1}$)	$5.2^{+0.4}_{-0.4}$
—Neutral iron lines—	
Gaussian 1	
(4) E_{640} (eV)	6400^{+4}_{-1}
(5) σ_{640} (eV)	0 (fix)
(6) F_{640} (10^{-4} photons cm $^{-2}$ s $^{-1}$)	$1.14^{+0.04}_{-0.03}$
Gaussian 2	
(7) E_{706} (eV)	7058^b
(8) σ_{706} (eV)	0 (fix)
(9) F_{706} (10^{-4} photons cm $^{-2}$ s $^{-1}$)	$0.11^{+0.05}_{-0.07}$
—Ionized iron lines—	
Gaussian 3	
(10) E_{667} (eV)	6665^{+4}_{-3}
(11) σ_{667} (eV)	27^{+7}_{-9}
(12) F_{667} (10^{-4} photons cm $^{-2}$ s $^{-1}$)	$1.07^{+0.04}_{-0.05}$
Gaussian 4	
(13) E_{697} (eV)	6966^{+14}_{-13}
(14) σ_{697} (eV)	0 (fix)
(15) F_{697} (10^{-4} photons cm $^{-2}$ s $^{-1}$)	$0.32^{+0.05}_{-0.04}$
(16) δ_{Gain} (eV)	0(fix)
χ^2/dof	574.43/514

Note—Parentheses indicate the 90% confidence limit. (1): Absorption column density. (2): Photon index. (3): Observed flux of a power-law continuum in the 5–8 keV band. (4),(7),(10),(13): Line centroid. (5),(8),(11),(14): Line width in the Gaussian sigma. (6),(9),(12),(15): Observed line flux. (16): Additional gain offset.

^b The energy gap between K α (6400 eV) and K β (7058 eV) is fixed at the theoretical value (+658 eV) (Kaastra & Mewe 1993).

Table 6.2: The XMM-Newton 2004 result of spectral fitting for the Sgr B2 region

Model	N_{H}	Γ	F_{pow}	F_{640}	F_{706}	F_{667}	F_{697}	δ_{Gain}	χ^2/dof
	(1)	(2)	(3)	(4)	(5)	(6)	(7)	(8)	(9)
XMM-Newton 2004 MOS									
I	$5.3^{+1.4}_{-1.3}$	$3.6^{+0.7}_{-0.7}$	$4.8^{+0.2}_{-0.2}$	$1.03^{+0.08}_{-0.08}$	$0.13^{+0.07}_{-0.07}$	$0.91^{+0.04}_{-0.08}$	0.27 ^c	0(fix)	88.85/93
II	$3.6^{+0.7}_{-0.7}$	2.6 ^a	$4.9^{+0.2}_{-0.2}$	$1.04^{+0.08}_{-0.08}$	$0.10^{+0.07}_{-0.07}$	$0.92^{+0.08}_{-0.04}$	0.27 ^c	0(fix)	95.10/94
III	3.0 ^a	$2.6^{+0.3}_{-0.3}$	$4.8^{+0.2}_{-0.2}$	$1.07^{+0.07}_{-0.07}$	$0.12^{+0.07}_{-0.07}$	$0.95^{+0.07}_{-0.07}$	0.28 ^c	0(fix)	97.19/94
IV	3.0 ^a	2.6 ^a	$4.8^{+0.2}_{-0.2}$	$1.07^{+0.07}_{-0.07}$	$0.12^{+0.07}_{-0.07}$	$0.95^{+0.07}_{-0.07}$	0.28 ^c	0(fix)	97.20/95
XMM-Newton 2004 PN									
I	$2.1^{+0.4}_{-0.4}$	$1.6^{+0.2}_{-0.1}$	$7.0^{+0.2}_{-0.2}$	$1.06^{+0.05}_{-0.07}$	$0.15^{+0.05}_{-0.15}$	$0.89^{+0.06}_{-0.06}$	0.27 ^c	21^{+3}_{-3}	185.62/169
II	$3.7^{+0.7}_{-0.1}$	2.6 ^a	$6.8^{+0.2}_{-0.2}$	$1.02^{+0.08}_{-0.05}$	$0.06^{+0.05}_{-0.06}$	$0.88^{+0.05}_{-0.09}$	0.26 ^c	23^{+4}_{-3}	209.71/170
III	3.0 ^a	$1.9^{+0.2}_{-0.2}$	$7.1^{+0.2}_{-0.2}$	$1.01^{+0.07}_{-0.05}$	$0.10^{+0.05}_{-0.10}$	$0.85^{+0.05}_{-0.06}$	0.27 ^c	21^{+4}_{-3}	188.47/170
IV	3.0 ^a	2.6 ^a	$6.6^{+0.2}_{-0.2}$	$1.07^{+0.06}_{-0.06}$	$0.08^{+0.04}_{-0.05}$	$0.92^{+0.05}_{-0.05}$	0.27 ^c	21^{+6}_{-3}	223.78/171

Note—Parentheses indicate the 90% confidence limit. (1): Absorption column density (10^{23} H cm⁻²). (2): Photon index. (3): Observed flux of a powerlaw continuum in the 5–8 keV band (10^{-4} photons cm⁻² s⁻¹). (4),(5),(6),(7): Observed line flux of 6.40, 7.06, 6.67, 6.97 keV line (10^{-4} photons cm⁻² s⁻¹). (8): Additional gain offset (eV). (9): χ^2 value per Degree of Freedom.

^a Fixed at the value obtained with Suzaku fit.

^c The intensity of Fe XXVI K α is fixed at 30% of that of Fe XXV K α determined by the Suzaku fit.

Table 6.3: The XMM-Newton 2001 result of spectral fitting for the Sgr B2 region

Model	N_{H}	Γ	F_{pow}	F_{640}	F_{706}	F_{667}	F_{697}	δ_{Gain}	χ^2/dof
	(1)	(2)	(3)	(4)	(5)	(6)	(7)	(8)	(9)
XMM-Newton 2001 MOS									
I	$0.5^{+1.3}_{-0.5}$	$0.4^{+0.6}_{-0.5}$	$8.8^{+0.4}_{-0.4}$	$1.52^{+0.15}_{-0.16}$	$0.16^{+0.16}_{-0.14}$	$1.22^{+0.15}_{-0.16}$	0.36 ^c	0(fix)	88.51/101
II	$4.2^{+1.0}_{-0.9}$	2.6 ^a	$8.2^{+0.3}_{-0.3}$	$1.53^{+0.12}_{-0.26}$	$0.31^{+0.12}_{-0.22}$	$1.16^{+0.17}_{-0.19}$	0.34 ^c	0(fix)	119.45/102
III	3.0 ^a	$1.3^{+0.4}_{-0.4}$	$8.9^{+0.4}_{-0.4}$	$1.43^{+0.15}_{-0.16}$	$0.16^{+0.14}_{-0.16}$	$1.10^{+0.15}_{-0.15}$	0.32 ^c	0(fix)	98.09/102
IV	3.0 ^a	2.6 ^a	$7.7^{+0.3}_{-0.3}$	$1.55^{+0.14}_{-0.16}$	$0.32^{+0.14}_{-0.14}$	$1.28^{+0.14}_{-0.14}$	0.38 ^c	0(fix)	124.30/103
XMM-Newton 2001 PN									
I	$1.5^{+1.0}_{-0.9}$	$0.9^{+0.4}_{-0.4}$	$9.4^{+0.3}_{-0.3}$	$1.27^{+0.11}_{-0.12}$	$0.17^{+0.09}_{-0.09}$	$0.81^{+0.11}_{-0.11}$	0.24 ^c	35^{+4}_{-11}	188.08/164
II	$4.7^{+0.3}_{-0.4}$	2.6 ^a	$9.2^{+0.3}_{-0.3}$	$1.19^{+0.11}_{-0.11}$	$0.19^{+0.09}_{-0.08}$	$0.72^{+0.10}_{-0.10}$	0.27 ^c	35^{+3}_{-11}	230.89/165
III	3.0 ^a	$1.4^{+0.2}_{-0.2}$	$9.6^{+0.3}_{-0.3}$	$1.21^{+0.11}_{-0.11}$	$0.14^{+0.10}_{-0.08}$	$0.73^{+0.10}_{-0.10}$	0.27 ^c	32^{+4}_{-9}	194.13/165
IV	3.0 ^a	2.6 ^a	$8.6^{+0.3}_{-0.3}$	$1.29^{+0.11}_{-0.10}$	$0.28^{+0.09}_{-0.08}$	$0.88^{+0.09}_{-0.10}$	0.27 ^c	36^{+4}_{-10}	248.33/166

Note—Parentheses indicate the 90% confidence limit. (1): Absorption column density (10^{23} H cm⁻²). (2): Photon index. (3): Observed flux of a powerlaw continuum in the 5–8 keV band (10^{-4} photons cm⁻² s⁻¹). (4),(5),(6),(7): Observed line flux of 6.40, 7.06, 6.67, 6.97 keV line (10^{-4} photons cm⁻² s⁻¹). (8): Additional gain offset (eV). (9): χ^2 value per Degree of Freedom.

^a Fixed at the value obtained with Suzaku fit.

^c The intensity of Fe XXVI K α is fixed at 30% of that of Fe XXV K α determined by the Suzaku fit.

Table 6.4: The XMM-Newton 2004 results of spectral fitting for the Sgr B2 region with multiplied blank-sky backgrounds

Model	N_{H}	Γ	F_{pow}	F_{640}	F_{706}	F_{667}	F_{697}	δ_{Gain}	χ^2/dof
	(1)	(2)	(3)	(4)	(5)	(6)	(7)	(8)	(9)
XMM-Newton 2004 MOS [†]									
I
II
III
IV
XMM-Newton 2004 PN									
I	$4.4^{+0.2}_{-0.9}$	$3.1^{+0.2}_{-0.2}$	$5.5^{+0.2}_{-0.2}$	$1.05^{+0.06}_{-0.06}$	$0.06^{+0.05}_{-0.05}$	$0.90^{+0.05}_{-0.06}$	0.27^c	20^{+4}_{-3}	238.40/169
II	$3.2^{+0.3}_{-0.2}$	2.6^a	$5.6^{+0.2}_{-0.2}$	$1.07^{+0.06}_{-0.06}$	$0.06^{+0.06}_{-0.05}$	$0.91^{+0.06}_{-0.06}$	0.27^c	24^{+4}_{-4}	240.94/170
III	3.0^a	$2.6^{+0.3}_{-0.2}$	$5.5^{+0.2}_{-0.2}$	$1.08^{+0.06}_{-0.06}$	$0.07^{+0.05}_{-0.05}$	$0.92^{+0.06}_{-0.06}$	0.27^c	23^{+1}_{-4}	240.73/170
IV	3.0^a	2.6^a	$5.5^{+0.2}_{-0.2}$	$1.08^{+0.06}_{-0.06}$	$0.07^{+0.04}_{-0.06}$	$0.92^{+0.06}_{-0.06}$	0.27^c	23^{+1}_{-4}	241.10/171

Note—Parentheses indicate the 90% confidence limit. (1): Absorption column density (10^{23} H cm⁻²). (2): Photon index. (3): Observed flux of a powerlaw continuum in the 5–8 keV band (10^{-4} photos cm⁻² s⁻¹). (4),(5),(6),(7): Observed line flux of 6.40, 7.06, 6.67, 6.97 keV line (10^{-4} photons cm⁻² s⁻¹). (8): Additional gain offset (eV). (9): χ^2 value per Degree of Freedom.

[†] No correction is needed.

^a Fixed at the value obtained with Suzaku fit.

^c The intensity of Fe XXVI K α is fixed at 30% of that of Fe XXV K α determined by the Suzaku fit.

We must note that the intensities of the XMM-Newton NXB are time dependent (Carter & Read 2007). The residual of the NXB lines may affect the estimates of the iron line fluxes. We checked each count rate of MOS and PN over 10 keV, where the NXB is dominant, and multiplied the background spectra to match the count rates with those of the source. The background correction factors for the data in 2004 are relatively small (1.0 for MOS, and 1.4 for PN), while those for the data in 2001 are 2.1 for MOS, and 2.6 for PN. We re-fitted the spectra with these new backgrounds. The results are shown in table 6.4 and 6.5. The derived line fluxes are almost consistent within the statistical errors, while the inconsistency of the continuum fluxes between MOS and PN is improved. We also mention that in this method we overestimate the CXB component. The CXB surface brightness with a typical Galactic absorption of 1×10^{23} cm⁻² is about 1×10^{-15} ergs cm⁻² s⁻¹ arcmin⁻². The CXB flux in the Sgr B2 region, the size of which is 106 arcmin², is expected to be 1×10^{-13} ergs cm⁻² s⁻¹ arcmin⁻², which is just a few percent of the continuum flux.

Table 6.5: The XMM-Newton 2001 results of spectral fitting for the Sgr B2 region with multiplied blank-sky backgrounds

Model	N_{H}	Γ	F_{pow}	F_{640}	F_{706}	F_{667}	F_{697}	δ_{Gain}	χ^2/dof
	(1)	(2)	(3)	(4)	(5)	(6)	(7)	(8)	(9)
XMM-Newton 2001 MOS									
I	$7.2^{+5.5}_{-3.6}$	$6.0^{+3.7}_{-2.4}$	$3.9^{+0.3}_{-0.3}$	$1.49^{+0.16}_{-0.16}$	$0.21^{+0.15}_{-0.15}$	$1.23^{+0.16}_{-0.16}$	0.36^c	0(fix)	84.18/101
II	$1.8^{+1.3}_{-1.3}$	2.6^a	$4.4^{+0.3}_{-0.3}$	$1.51^{+0.16}_{-0.16}$	$0.14^{+0.14}_{-0.14}$	$1.23^{+0.15}_{-0.16}$	0.34^c	0(fix)	92.55/102
III	3.0^a	$3.7^{+0.8}_{-0.7}$	$4.1^{+0.3}_{-0.3}$	$1.52^{+0.16}_{-0.15}$	$0.17^{+0.15}_{-0.14}$	$1.25^{+0.15}_{-0.15}$	0.32^c	0(fix)	88.01/102
IV	3.0^a	2.6^a	$4.6^{+0.3}_{-0.3}$	$1.46^{+0.15}_{-0.15}$	$0.10^{+0.14}_{-0.10}$	$1.17^{+0.15}_{-0.15}$	0.35^c	0(fix)	94.70/103
XMM-Newton 2001 PN									
I	$6.2^{+1.8}_{-1.4}$	$4.1^{+0.7}_{-0.9}$	$5.0^{+0.3}_{-0.3}$	$1.28^{+0.12}_{-0.11}$	$0.24^{+0.09}_{-0.10}$	$0.84^{+0.11}_{-0.11}$	0.25^c	33^{+4}_{-10}	260.40/164
II	$3.5^{+1.1}_{-0.9}$	2.6^a	$5.1^{+0.3}_{-0.3}$	$1.32^{+0.11}_{-0.12}$	$0.21^{+0.10}_{-0.09}$	$0.87^{+0.11}_{-0.05}$	0.27^c	32^{+4}_{-9}	267.51/165
III	3.0^a	$2.8^{+0.1}_{-0.3}$	$4.9^{+0.3}_{-0.3}$	$1.35^{+0.03}_{-0.06}$	$0.24^{+0.05}_{-0.03}$	$0.92^{+0.04}_{-0.03}$	0.27^c	35^{+1}_{-12}	267.11/165
IV	3.0^a	2.6^a	$5.0^{+0.3}_{-0.3}$	$1.34^{+0.11}_{-0.11}$	$0.23^{+0.10}_{-0.09}$	$0.90^{+0.09}_{-0.10}$	0.27^c	34^{+4}_{-11}	267.94/166

Note—Parentheses indicate the 90% confidence limit. (1): Absorption column density (10^{23} H cm $^{-2}$). (2): Photon index. (3): Observed flux of a powerlaw continuum in the 5–8 keV band (10^{-4} photons cm $^{-2}$ s $^{-1}$). (4),(5),(6),(7): Observed line flux of 6.40, 7.06, 6.67, 6.97 keV line (10^{-4} photons cm $^{-2}$ s $^{-1}$). (8): Additional gain offset (eV). (9): χ^2 value per Degree of Freedom.

^a Fixed at the value obtained with Suzaku fit.

^c The intensity of Fe XXVI K α is fixed at 30% of that of Fe XXV K α determined by the Suzaku fit.

6.1.3 Chandra

With the same method as the previous section, we fitted the Chandra spectra with Model I. The spectrum in 2000 needs a systematic offset of ~ -20 eV to match the spectral shape. The spectrum in 2001 required too strange photon index ($\Gamma \sim -2.2$) and made large residuals over 7 keV when we fixed a photon index at 2.6. We checked the count rates in the 10.0–12.5 keV band between the source and the blank-sky spectra, then we found that no correction is needed for the data in 2000 while we must multiply the background by a factor of 2.4 to match the count rate for the data in 2001. The best-fit values are derived from the spectral fit with this new corrected background. Obtained values are shown in table 6.6. The flux of each line is determined within 10% error among the four continuum models.

6.1.4 ASCA

The ASCA spectrum needs large systematic gain offset about 80 eV to adjust iron line centroids. This large offset is caused by the chip-to-chip variation of the gain¹.

¹See <http://heasarc.gsfc.nasa.gov/docs/asca/4ccd.html>

Table 6.6: The Chandra 2000 and 2001 results of spectral fitting for the Sgr B2 region

Model	N_{H}	Γ	F_{pow}	F_{640}	F_{706}	F_{667}	F_{697}	δ_{Gain}	χ^2/dof
	(1)	(2)	(3)	(4)	(5)	(6)	(7)	(8)	(9)
Chandra 2001 ACIS									
I	$2.4^{+3.4}_{-2.4}$	$1.0^{+1.7}_{-1.5}$	$7.2^{+0.5}_{-0.5}$	$1.37^{+0.26}_{-0.26}$	$0.10^{+0.32}_{-0.10}$	$1.14^{+0.27}_{-0.27}$	0.34 ^c	0(fix)	37.51/50
II	$4.6^{+1.4}_{-1.4}$	2.6 ^a	$6.6^{+0.5}_{-0.5}$	$1.36^{+0.27}_{-0.25}$	$0.12^{+0.28}_{-0.12}$	$1.16^{+0.27}_{-0.27}$	0.34 ^c	0(fix)	39.02/51
III	3.0 ^a	$1.3^{+0.9}_{-0.7}$	$7.1^{+0.5}_{-0.5}$	$1.33^{+0.27}_{-0.24}$	$0.12^{+0.32}_{-0.12}$	$1.13^{+0.14}_{-0.41}$	0.34 ^c	0(fix)	37.67/51
IV	3.0 ^a	2.6 ^a	$6.0^{+0.4}_{-0.4}$	$1.48^{+0.24}_{-0.24}$	$0.20^{+0.28}_{-0.20}$	$1.30^{+0.24}_{-0.24}$	0.39 ^c	0(fix)	42.33/52
Chandra 2000 ACIS									
I	$1.0^{+0.5}_{-0.4}$	$0.7^{+0.4}_{-0.5}$	$6.7^{+0.2}_{-0.2}$	$1.71^{+0.08}_{-0.08}$	$0.17^{+0.09}_{-0.04}$	$1.00^{+0.08}_{-0.07}$	0.30 ^c	-20^{+4}_{-3}	195.97/169
II	$3.8^{+0.4}_{-0.3}$	2.6 ^a	$6.0^{+0.2}_{-0.2}$	$1.72^{+0.07}_{-0.10}$	$0.26^{+0.12}_{-0.08}$	$1.02^{+0.09}_{-0.08}$	0.30 ^c	-17^{+6}_{-3}	218.89/170
III	3.0 ^a	$1.7^{+0.3}_{-0.2}$	$6.5^{+0.2}_{-0.2}$	$1.67^{+0.08}_{-0.08}$	$0.21^{+0.08}_{-0.09}$	$0.97^{+0.08}_{-0.07}$	0.29 ^c	-18^{+8}_{-3}	205.41/170
IV	3.0 ^a	2.6 ^a	$5.7^{+0.2}_{-0.2}$	$1.76^{+0.08}_{-0.08}$	$0.31^{+0.09}_{-0.09}$	$1.08^{+0.07}_{-0.08}$	0.32 ^c	-19^{+8}_{-1}	224.15/171

Note—Parentheses indicate the 90% confidence limit. (1): Absorption column density (10^{23} H cm⁻²). (2): Photon index. (3): Observed flux of a powerlaw continuum in the 5–8 keV band (10^{-4} photons cm⁻² s⁻¹). (4),(5),(6),(7): Observed line flux of 6.40, 7.06, 6.67, 6.97 keV line (10^{-4} photons cm⁻² s⁻¹). (8): Additional gain offset (eV). (9): χ^2 value per Degree of Freedom.

^a Fixed at the value obtained with Suzaku fit.

^c The intensity of Fe XXVI K α is fixed at 30% of that of Fe XXV K α determined by the Suzaku fit.

We fit the SIS spectrum with the four continuum models used in the previous sections. The best-fit parameters are shown in table 6.7. Model dependent fluctuation on the line fluxes are far small compared to the statistical errors.

6.1.5 Comparison Analysis

Model Dependence

The 6.67 keV fluxes obtained by fittings with Model I–IV in a unit of surface brightness by dividing the size of the source region (106 arcmin²) are shown in figure 6.3. While the values with Model III are systematically low and those with Model IV are high, the fluctuations are entirely within the statistical errors. Then we use the value with Model I as the result of each observation.

Systematic Errors

The 6.67 keV line emission is due to the GCDX and a strong 6.67 keV source, G0.61+0.01, which contributes about 30% of the total 6.67 keV line emission. These emissions can be considered to be constant in time. However, a constant model on the 6.67 keV flux is rejected by the χ^2 statistics ($\chi^2/\text{dof}=56.32/8$).

Table 6.7: The ASCA 1994 result of spectral fitting for the Sgr B2 region

Model	N_{H}	Γ	F_{pow}	F_{640}	F_{706}	F_{667}	F_{697}	δ_{Gain}	χ^2/dof
	(1)	(2)	(3)	(4)	(5)	(6)	(7)	(8)	(9)
ASCA 1994 SIS									
I	$0.7^{+1.0}_{-0.7}$	$1.1^{+0.7}_{-0.5}$	$5.8^{+0.2}_{-0.2}$	$1.63^{+0.18}_{-0.17}$	$0.22^{+0.15}_{-0.13}$	$1.20^{+0.18}_{-0.18}$	0.35^c	71^{+21}_{-13}	81.81/76
II	$3.1^{+0.7}_{-0.3}$	2.6^a	$5.5^{+0.2}_{-0.2}$	$1.65^{+0.16}_{-0.18}$	$0.30^{+0.17}_{-0.15}$	$1.14^{+0.16}_{-0.18}$	0.33^c	81^{+18}_{-20}	92.69/77
III	3.0^a	$2.1^{+0.3}_{-0.3}$	$5.8^{+0.2}_{-0.2}$	$1.62^{+0.14}_{-0.19}$	$0.24^{+0.13}_{-0.15}$	$1.07^{+0.18}_{-0.13}$	0.32^c	81^{+19}_{-19}	89.00/77
IV	3.0^a	2.6^a	$5.4^{+0.2}_{-0.2}$	$1.65^{+0.17}_{-0.10}$	$0.30^{+0.17}_{-0.14}$	$1.15^{+0.15}_{-0.16}$	0.33^c	81^{+18}_{-5}	92.87/78

Note—Parentheses indicate the 90% confidence limit. (1): Absorption column density (10^{23} H cm $^{-2}$). (2): Photon index. (3): Observed flux of a powerlaw continuum in the 5–8 keV band (10^{-4} photons cm $^{-2}$ s $^{-1}$). (4),(5),(6),(7): Observed line flux of 6.40, 7.06, 6.67, 6.97 keV line (10^{-4} photons cm $^{-2}$ s $^{-1}$). (8): Additional gain offset (eV). (9): χ^2 value per Degree of Freedom.

^a Fixed at the value obtained with Suzaku fit.

^c The intensity of Fe XXVI K α is fixed at 30% of that of Fe XXV K α determined by the Suzaku fit.

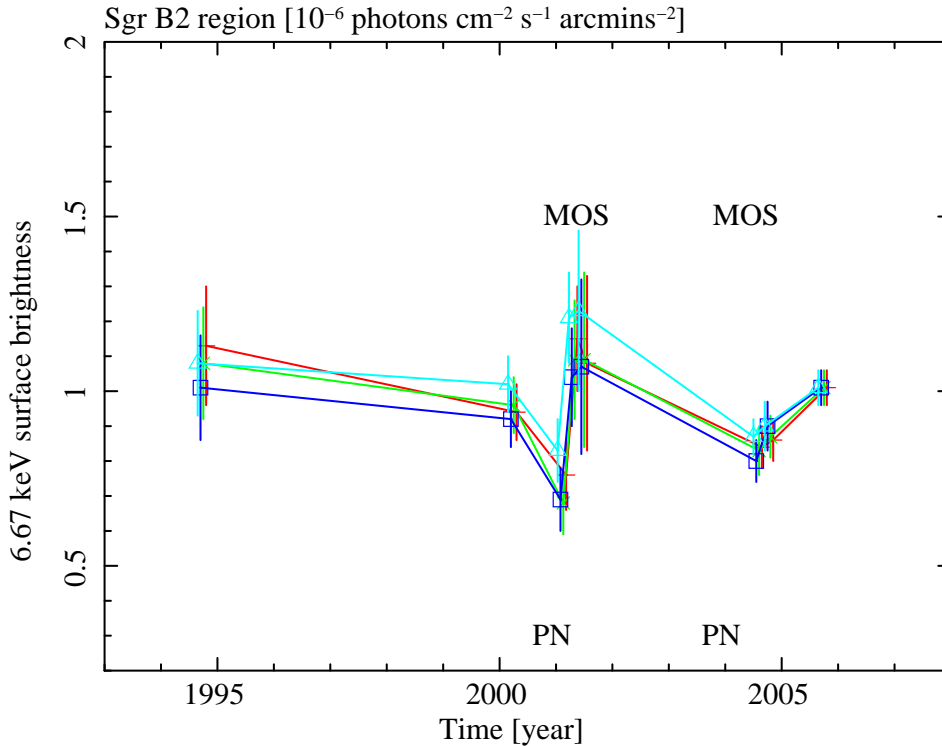


Figure 6.3: The 6.67 keV line surface brightness obtained with each observation in the Sgr B2 region. In this plot, each error bar indicates the 90% confidence. The values are marked with red circles for Model I, green x marks for Model II, blue squares for Model III and aqua triangles for Model IV.

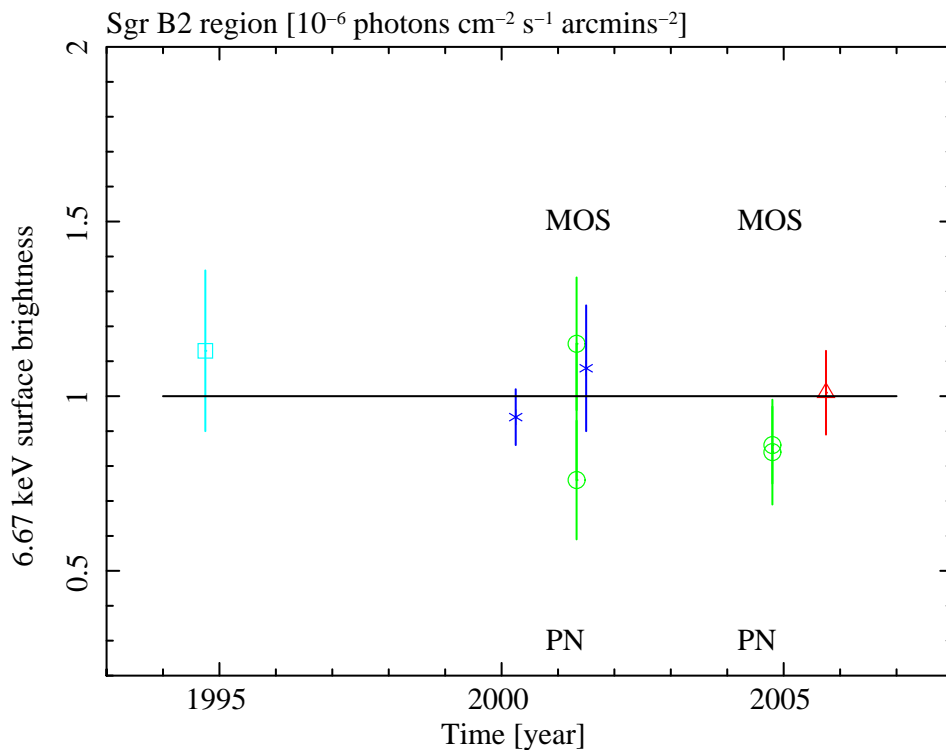


Figure 6.4: The 6.67 keV line surface brightness with Model I but each error bar in this plot indicates one sigma statistical error plus the systematic error of the detector. The data are marked with a triangle mark for Suzaku, a circle for XMM-Newton, an asterisk for Chandra and a square for ASCA. The average flux is shown in a solid horizontal line.

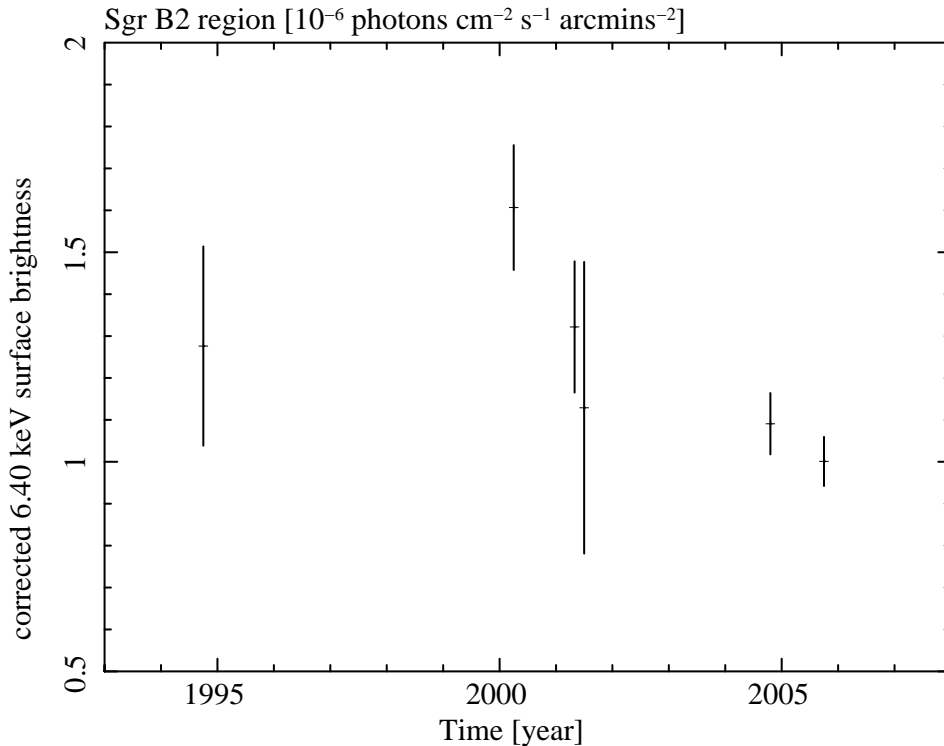


Figure 6.5: The light curve of the corrected 6.40 keV line surface brightness in the Sgr B2 region. The XMM-Newton values are the average of MOS and PN. In this plot, each error bar indicates the 90% confidence limit.

Then we considered systematic response errors of the efficiencies. The absolute response uncertainty of EPIC is 10% and the MOS flux is 10–15% higher than the PN (Carter & Read 2007). The systematic errors of the other detectors are 10% for Suzaku (Serlemitsos et al. 2007), 5% for Chandra (Schwartz et al. 2000), and 13% for ASCA SIS². The 6.67 keV flux considering these systematic error in each observation period is plotted in figure 6.4. The χ^2/dof value with a constant model on this plot is 4.848/8, which is acceptable in 70% confidence. Therefore we conclude that the obtained line fluxes are fluctuated by the systematic errors of mirror responses. Then we calculate the flux correction factor to normalize the 6.67 keV flux of each observation to the average value, and correct each 6.40 keV flux with the factor.

Figure 6.5 shows the corrected 6.40 keV line surface brightness in each observation period. In this figure, the XMM-Newton values are the averaged fluxes of MOS and PN. The 6.40 keV line flux is significantly variable with $\chi^2/\text{dof} = 28.9/6$, shows

²See <http://heasarc.gsfc.nasa.gov/listserv/ascanews/msg00143.html>

a decline in 2001, and finally drops into 60% from 2000 to 2005.

6.2 Variability Verifications on Individual Sources

6.2.1 Surface Brightness Mapping

In order to examine the 6.40 keV line flux in morphology, we make the surface brightness map of iron lines in each observation. Since the energy resolution of Chandra or ASCA are not good enough to separate the 6.40 keV line from the 6.67 keV line, we make images in the 6–7 keV band. The surface brightness maps of 6–7 keV band are made by the raw images by dividing the exposure maps with effective areas. To eliminate the component of the powerlaw continuum, we make the surface brightness maps in the 5–6 keV band in the same method. We subtract 65% of the 5–6 keV maps from the 6–7 keV maps as a continuum emission assuming the photon index is 2.6. Finally we rebin all the maps to make each pixel size about 50-arcsec square, about a size of the PSF of ASCA.

Figure 6.6(a)–(d) show the surface brightness maps of iron lines. The Suzaku and the XMM-Newton images are relatively dim in the whole area compared to those of Chandra and ASCA, which is consistent with the result of the spectral fitting. In the Chandra image, brighter point is found in the west where G 0.570–0.018 is located (Senda et al. 2002).

We select the brightest point M 0.66–0.02 (Sgr B2 cloud, shown as a solid circle in figure 6.6) and G 0.570–0.018 (shown as a dashed circle in figure 6.6). Then we examine the variations of the 6.40 keV flux from these regions. Hereafter we exclude Chandra data in 2001 because they do not have enough statistics for the analysis.

6.2.2 M 0.66–0.02

We extract the spectra of M 0.66–0.02 (Sgr B2 cloud) from the solid circle with a radius of 3.2 arcmin in figure 6.6 and the blank-sky background spectra in the same detector position. In the ASCA image, the peak point of M 0.66–0.02 is seems to be different from the others. The difference is ~ 1 arcmin, which is similar to the SIS astrometry uncertainty. It is not clear whether this shift is due to a relatively large error of the ASCA astrometry (no fine-tuning of the ASCA astrometry was performed) or due to a real shift in the variable 6.40 keV line. Therefore, in the ASCA analysis, we selected two circles for M 0.66–0.02, at the same as the position in the original coordinate of Suzaku, XMM-Newton, and Chandra (P) and at the center on the peak of the SIS image (Q).

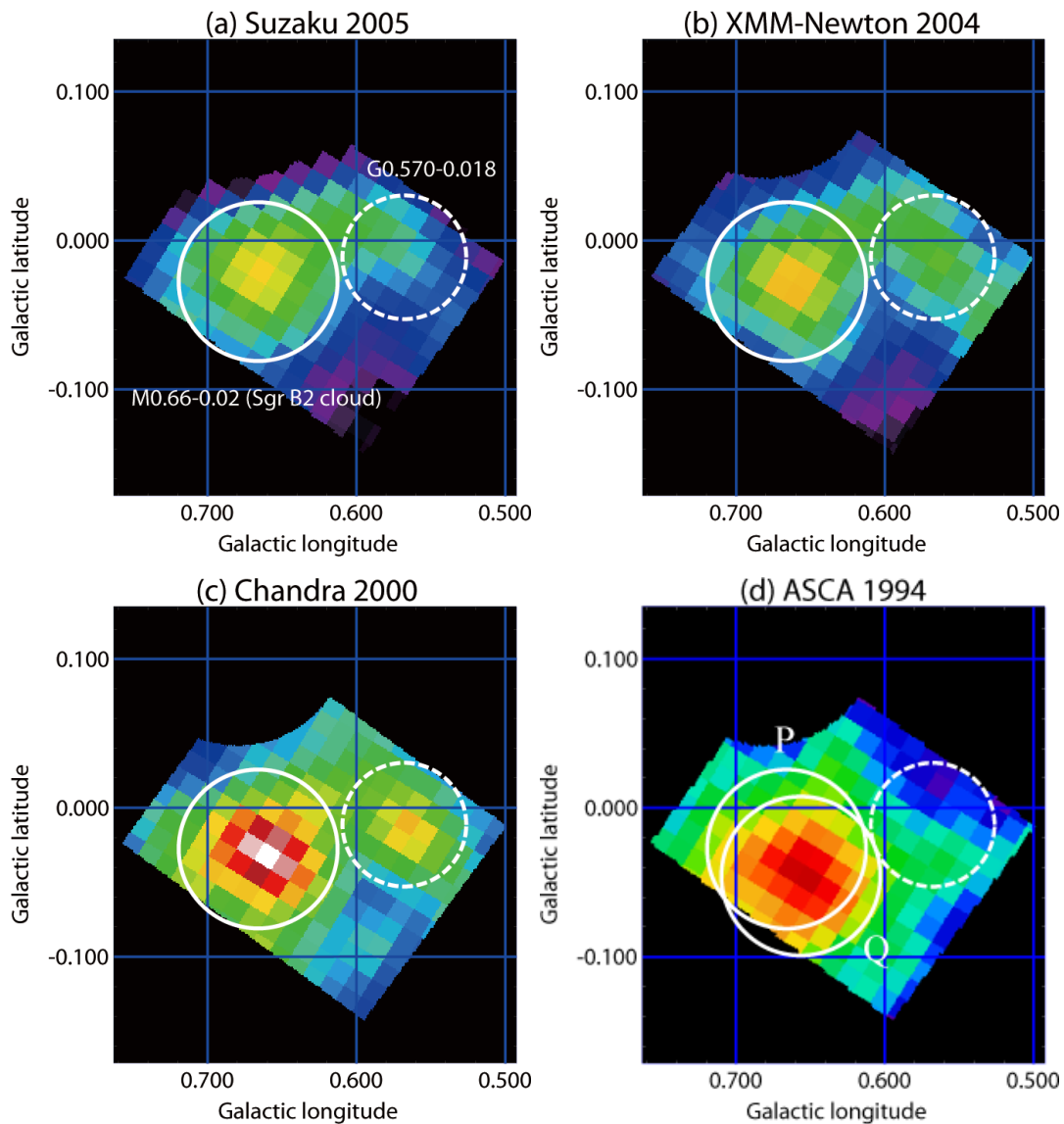


Figure 6.6: The surface brightness maps of iron lines obtained with (a) Suzaku XIS 2005, (b) XMM-Newton MOS and PN 2004, (c) Chandra ACIS-I 2000, and (d) ASCA SIS 1994. Each pixel size is $50'' \times 50''$

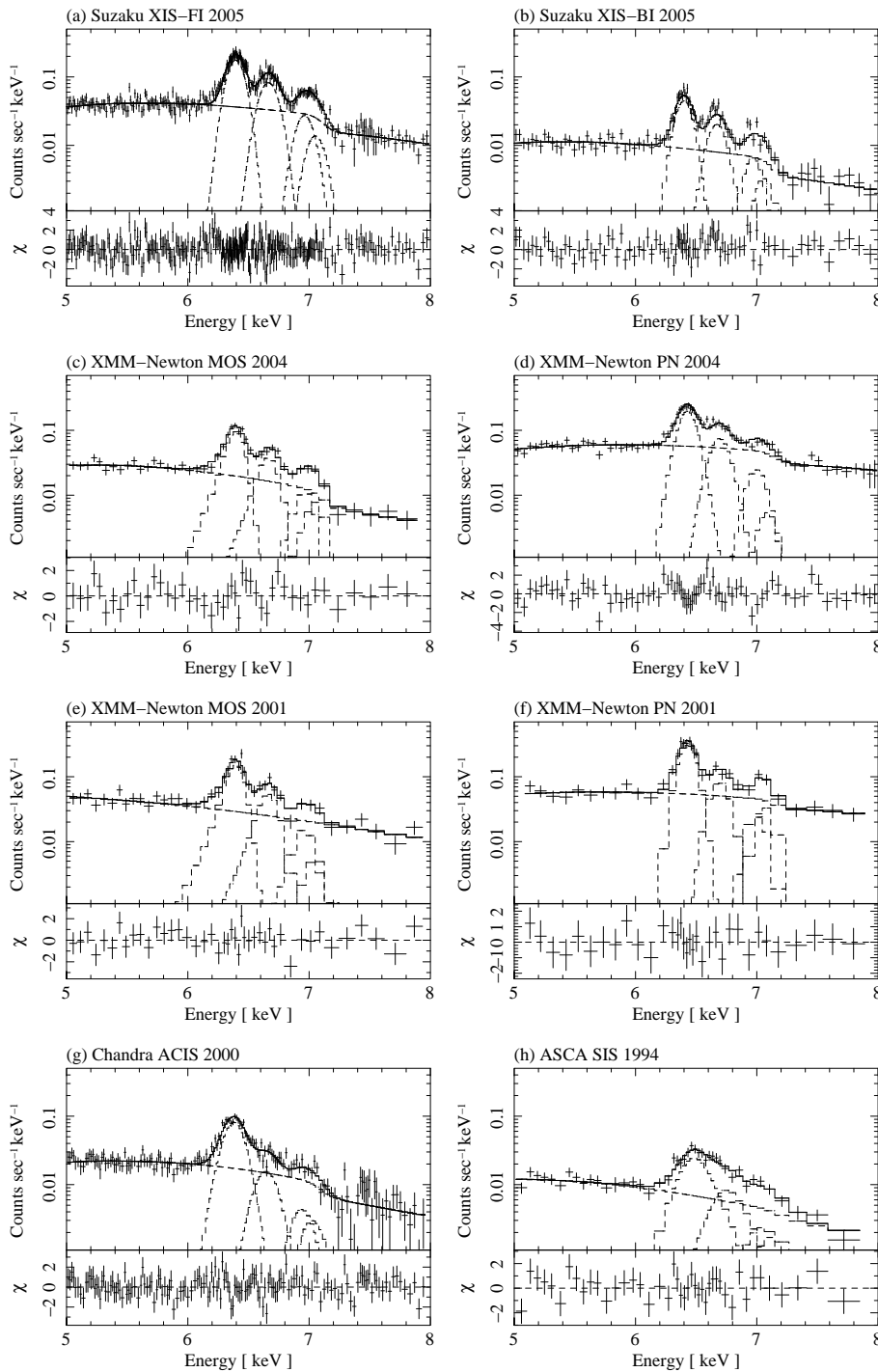


Figure 6.7: The spectra for M0.66–0.02 obtained with Suzaku XIS FI sensors (a) and BI sensor (b) in 2005, XMM-Newton MOS (c) and PN (d) in 2004, (e) and (f) in 2001, Chandra ACIS-I (g) in 2000, and ASCA SIS (h) in 1994. The solid lines indicate the best-fit models with Model I.

Table 6.8: The result of spectral fitting for M 0.66–0.02 with Model I

Observatory	Suzaku	XMM-Newton		XMM-Newton		Chandra	ASCA
Detector	XIS	MOS	PN	MOS	PN	ACIS	SIS [†]
(1) N_{H}	$5.0^{+0.5}_{-0.3}$	$5.4^{+2.1}_{-2.0}$	$3.7^{+1.1}_{-1.1}$	$0.2^{+2.4}_{-0.2}$	$2.5^{+2.8}_{-2.5}$	$4.3^{+1.1}_{-1.6}$	$3.0^{+2.9}_{-1.4}$
(2) Γ	$3.0^{+0.3}_{-0.3}$	$3.2^{+0.5}_{-1.0}$	$1.7^{+0.2}_{-0.3}$	$0.1^{+1.0}_{-0.5}$	$1.2^{+1.1}_{-1.1}$	$1.2^{+0.5}_{-0.9}$	$1.7^{+1.9}_{-1.4}$
(3) F_{pow}	$2.0^{+0.1}_{-0.1}$	$1.6^{+0.1}_{-0.1}$	$2.4^{+0.1}_{-0.1}$	$3.0^{+0.2}_{-0.2}$	$2.4^{+0.2}_{-0.2}$	$2.7^{+0.1}_{-0.1}$	$2.3^{+0.2}_{-0.2}$
—Neutral iron lines—							
(4) E_{640}	6399^{+4}_{-3}	6399^a					
(5) F_{640}	$0.66^{+0.02}_{-0.02}$	$0.58^{+0.04}_{-0.04}$	$0.57^{+0.04}_{-0.04}$	$0.92^{+0.11}_{-0.11}$	$0.82^{+0.10}_{-0.09}$	$1.00^{+0.05}_{-0.06}$	$0.99^{+0.13}_{-0.14}$
(6) E_{706}	7057^b						
(7) F_{706}	$0.06^{+0.04}_{-0.04}$	$0.08^{+0.04}_{-0.04}$	$0.02^{+0.03}_{-0.02}$	$0.05^{+0.09}_{-0.05}$	$0.11^{+0.08}_{-0.07}$	$0.06^{+0.06}_{-0.04}$	$0.12^{+0.13}_{-0.11}$
—Ionized iron lines—							
(8) E_{667}	6670^{+5}_{-5}	6670^a					
(9) σ_{667}	29^{+12}_{-16}	29^a					
(10) F_{667}	$0.36^{+0.02}_{-0.02}$	$0.29^{+0.04}_{-0.04}$	$0.25^{+0.03}_{-0.03}$	$0.42^{+0.09}_{-0.09}$	$0.26^{+0.08}_{-0.07}$	$0.25^{+0.04}_{-0.04}$	$0.42^{+0.13}_{-0.14}$
(11) E_{697}	6967^{+21}_{-21}	6967^a					
(12) F_{697}	$0.12^{+0.03}_{-0.02}$	0.10^c	0.08^c	0.14^c	0.09^c	0.08^c	0.14^c
(13) δ_{Gain}	0(fix)	0(fix)	23^{+6}_{-4}	0(fix)	23^{+13}_{-17}	-19^{+8}_{-3}	81^{+21}_{-11}
χ^2/dof	348.41/354	36.92/40	71.27/68	35.29/38	16.64/27	142.13/144	36.14/37

Note—Parentheses indicate the 90% confidence limit. (1): Absorption column density (10^{23} H cm⁻²). (2): Photon index. (3): Observed flux of a powerlaw continuum in the 5–8 keV band (10^{-4} photons cm⁻² s⁻¹). (4),(6),(8),(11): Line centroid (eV). (5),(7),(10),(12): Observed line flux (10^{-4} photons cm⁻² s⁻¹). (9): Line width in gaussian sigma (eV). The other line widths are fixed at zero. (13): Additional gain offset (eV).

[†] Values are obtained from region 'P'.

^a Fixed at the value obtained with Suzaku fit.

^b The energy gap between K α (6400 eV) and K β (7058 eV) is fixed at the theoretical value (+658 eV) (Kaastra & Mewe 1993).

^c The intensity of Fe XXVI K α is fixed at 34% of that of Fe XXV K α obtained with Suzaku.

With the same method in section 6.1, we fit the Suzaku spectra and determine the line centroids and flux ratio of the ionized lines. Then we fix the line centroids and the ionized line ratio to the Suzaku values, we fit the other spectra with Model I. The best-fit spectra and parameters are shown in figure 6.7 and table 6.8, respectively.

We also operated the spectral fittings with Model II–IV. The fitting results of the 6.67 keV fluxes in a unit of surface brightness are shown in figure 6.8 (more details are shown in tables A.1–A.3 in the appendix). The model dependence of the line fluxes is comparable to the statistical error. For the spectra of XMM-Newton, we checked the dependence of the NXB with the same method in section 6.1.2, resulting little influence on the line fluxes (shown in table A.4,A.5). Therefore we estimated line fluxes with Model I.

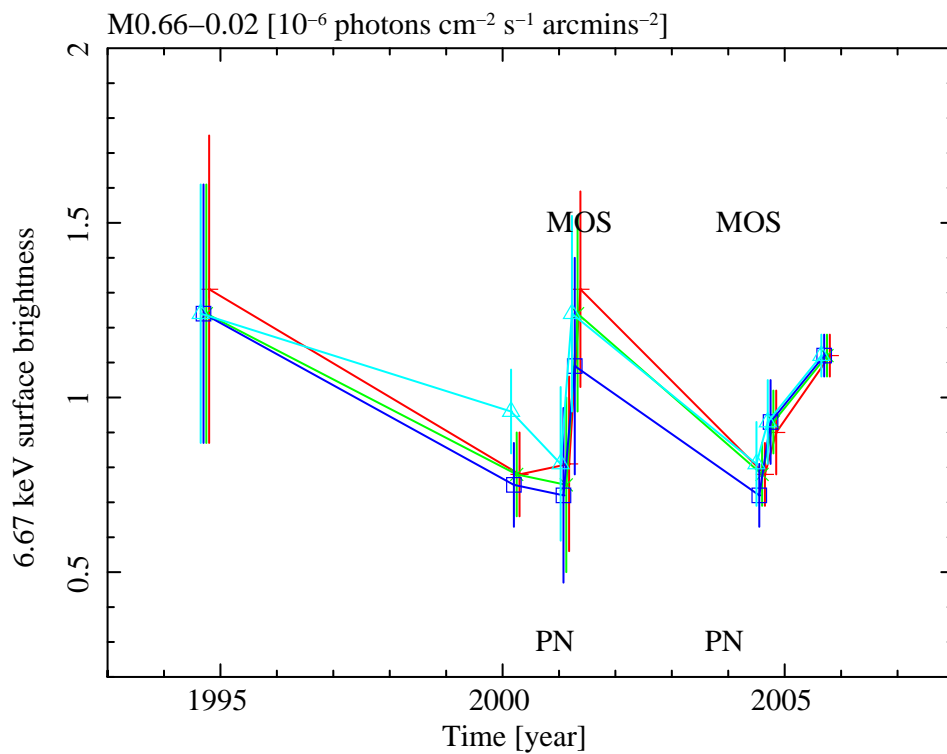


Figure 6.8: The 6.67 keV line surface brightness obtained with each observation in M0.66-0.02. In this plot, each error bar indicates the 90% confidence. The values are marked with red circles for Model I, green x marks for Model II, blue squares for Model III and aqua triangles for Model IV.

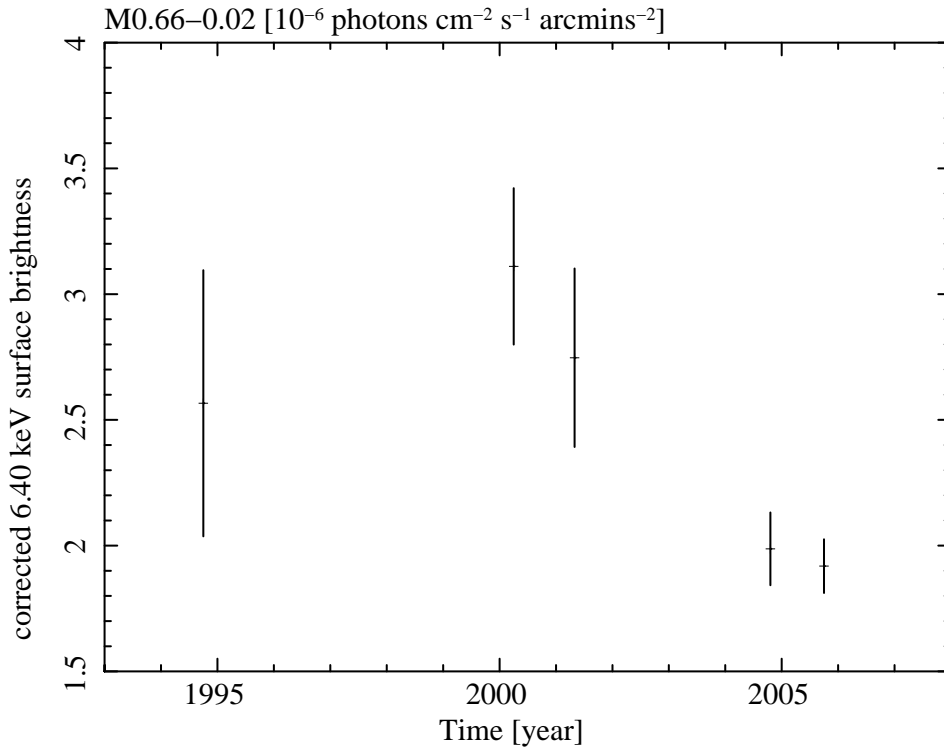


Figure 6.9: The light curve of the 6.40 keV line surface brightness from M0.66–0.02 (Sgr B2 cloud). In this plot, each error bar indicates the 90% confidence limit.

The derived SIS fluxes of the 6.40 keV line are $0.99^{+0.13}_{-0.14}$ for the spectrum of region 'P', and $0.93^{+0.11}_{-0.15} 10^{-4}$ photons $\text{cm}^{-2} \text{s}^{-1}$ for that of region 'Q'. These fluxes are consistent within the statistical error. Then we used the result of region 'P' as the SIS value.

Since the variation of the 6.67 keV fluxes is quite similar to that obtained with the whole Sgr B2 region shown in figure 6.4, it is also caused by the systematic error of each mirror response. In order to minimize the statistical errors of the correction factors, we used the values derived in section 6.1.5 to correct the 6.40 keV fluxes. The surface brightness of the 6.40 keV line is plotted in figure 6.9. The MOS and the PN values were averaged for each XMM observation. The time trend is quite similar to that of the whole region (figure 6.5) and the constant flux hypothesis is rejected with $\chi^2/\text{dof}=30.7/6$. The flux in 2000 is 1.5 times higher than that in 2004 and 2005, and also shows a decline in 2001.

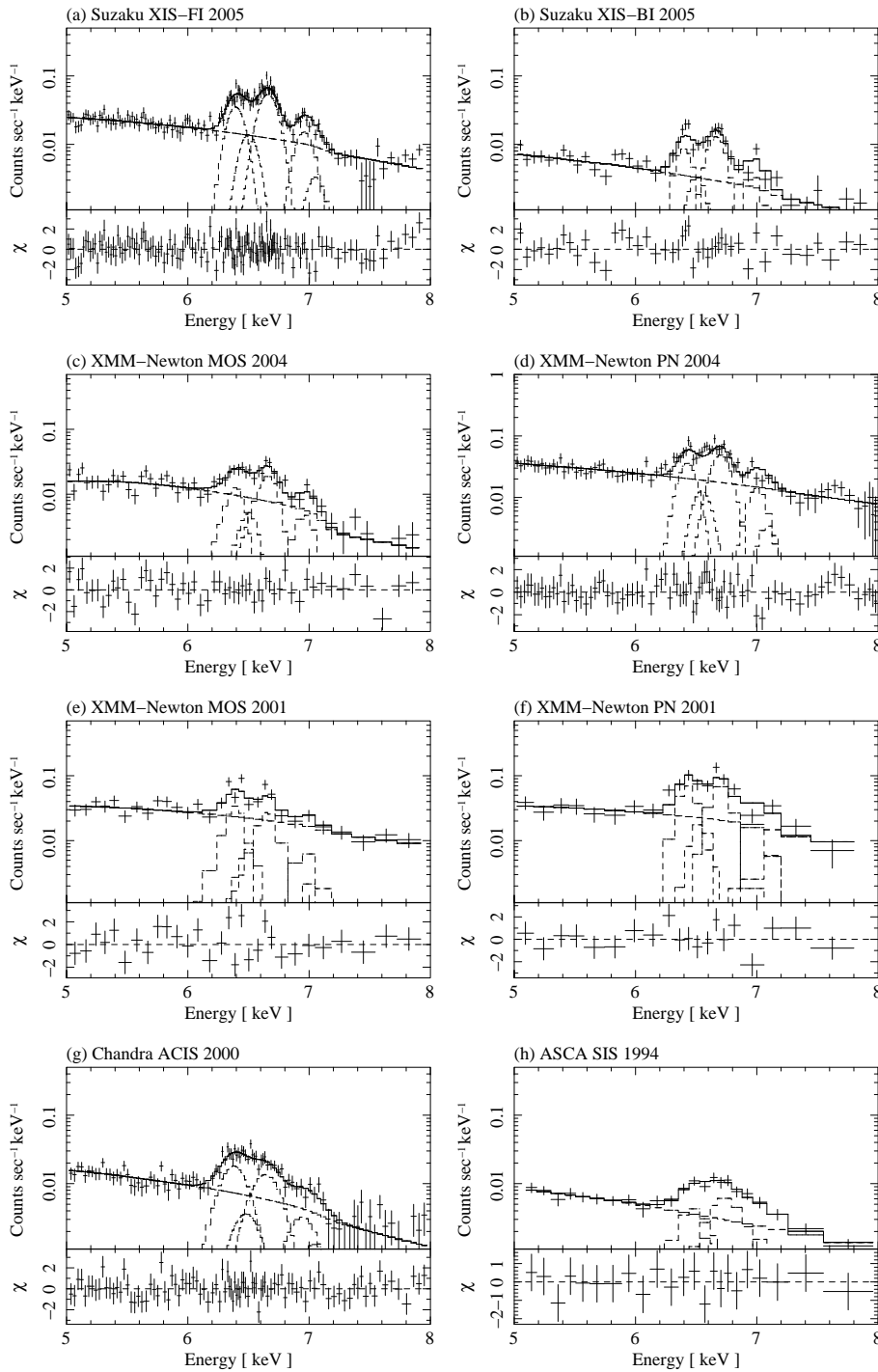


Figure 6.10: The spectra for G0.570–0.018 obtained with Suzaku XIS FI sensors (a) and BI sensor (b) in 2005, XMM-Newton MOS (c) and PN (d) in 2004, (e) and (f) in 2001, Chandra ACIS-I (g) in 2000, and ASCA SIS (h) in 1994. The solid lines indicate the best-fit models.

6.2.3 G0.570–0.018

G 0.570–0.018 is a diffuse source extending to about 10 arcmins (Senda et al. 2002). We extracted the 6.40 keV flux from G 0.570–0.018 (the dashed circle with a radius of 2.5 arcmin in figure 6.6) with the same way as M 0.66–0.02. Since the spectra do not have enough statistics to derive the Fe I $K\beta$ (7.06 keV) line, the intensity of $K\beta$ is fixed at 12.5% of that of $K\alpha$ (Kaastra & Mewe 1993). With the same method as M 0.66–0.02, we firstly fit the Suzaku spectra with Model I. Then we obtained 6415 eV as a line centroid of the 6.40 keV line, which is slightly higher than the values obtained in the other region, and 35 eV as a line width of the 6.67 keV line, which is also a little wider value. We re-fitted them with the line centroids fixed at the values of the Sgr B2 region (table 6.1) and we found some residuals between 6.4–6.6 keV. We added one Gaussian function in this energy band, and obtained an acceptable fit. The centroid of the additional line is 6505 eV, which is consistent with the Fe XX line. This line energy is consistent with the result of Senda et al. (2002), which determined G 0.570–0.018 as a SNR candidate.

Since the flux of the 6.51 keV line is also constant in time, the flux ratio among the ionized iron lines was fixed at the following analysis. Then we fitted the other spectra with this model (Model I + one Gaussian line). Table 6.9 shows the best-fit parameters for G 0.570–0.018. The continuum models and the XMM-Newton backgrounds have little impact on determining the line fluxes (the results are shown tables B.1–B.3, B.4 and B.5 in the appendix). Therefore we used the values obtained with Model I as the results.

We corrected the 6.40 keV fluxes using the correction factors as we did for M 0.66–0.02. Figure 6.11 shows the time trend of the 6.40 keV line from G 0.570–0.018, which indicates a clear variability in the 6.40 keV line emission. A constant flux hypothesis is marginally rejected with $\chi^2/\text{dof} = 13.2/6$.

Senda et al. (2002) mentioned that G 0.570–0.018 is a simple SNR candidate, but the 6.40 keV variability suggests that G 0.570–0.018 includes an XRN (see Discussion). In fact, Miyazaki & Tsuboi (2000) reported a flux peak of the CS ($J=1-0$) line emission at $(l, b) = (0^\circ601, -0^\circ025)$, which indicates the presence of a molecular cloud. The light curve of G 0.570–0.018 is similar to that of M 0.66–0.02. Hence the distances of the two clouds from Sgr A* are the same. G 0.570–0.018 may be located in front of M 0.66–0.02 with some off-sets of the line of sight.

Table 6.9: The result of spectral fitting for G 0.570–0.018 with Model I plus one Gaussian function

Observatory	Suzaku	XMM-Newton		XMM-Newton		Chandra	ASCA
Detector	XIS	MOS	PN	MOS	PN	ACIS	SIS
(1) N_{H}	$1.5^{+1.3}_{-1.0}$	$6.2^{+1.6}_{-2.5}$	$0.4^{+1.7}_{-0.4}$	$1.3^{+1.4}_{-1.3}$	$1.5^{+3.6}_{-1.5}$	$2.0^{+2.7}_{-2.0}$	$0.2^{+3.4}_{-0.2}$
(2) Γ	$2.6^{+0.6}_{-0.5}$	$4.1^{+1.9}_{-1.6}$	$1.8^{+0.8}_{-0.6}$	$0.5^{+1.2}_{-0.9}$	$2.0^{+1.6}_{-1.2}$	$2.0^{+1.4}_{-0.6}$	$1.2^{+1.5}_{-0.8}$
(3) F_{pow}	$1.1^{+0.1}_{-0.1}$	$1.1^{+0.1}_{-0.1}$	$1.3^{+0.1}_{-0.1}$	$1.9^{+0.1}_{-0.1}$	$1.2^{+0.1}_{-0.1}$	$1.2^{+0.1}_{-0.1}$	$0.9^{+0.1}_{-0.1}$
—Neutral iron lines—							
(4) E_{640}	6400^a						
(5) F_{640}	$0.16^{+0.03}_{-0.05}$	$0.11^{+0.04}_{-0.04}$	$0.14^{+0.03}_{-0.03}$	$0.18^{+0.06}_{-0.06}$	$0.19^{+0.06}_{-0.06}$	$0.26^{+0.04}_{-0.04}$	$0.12^{+0.05}_{-0.05}$
(6) E_{706}	7058^a						
(7) F_{706}	0.02^b	0.01^b	0.02^b	0.02^b	0.02^b	0.03^b	0.01^b
—Ionized iron lines—							
(8) E_{667}	6665^a						
(9) σ_{667}	27^a						
(10) F_{667}	$0.29^{+0.02}_{-0.02}$	$0.20^{+0.04}_{-0.04}$	$0.22^{+0.03}_{-0.03}$	$0.18^{+0.06}_{-0.06}$	$0.23^{+0.06}_{-0.06}$	$0.25^{+0.03}_{-0.03}$	$0.20^{+0.04}_{-0.02}$
(11) E_{697}	6966^a						
(12) F_{697}	0.09^c	0.07^c	0.07^c	0.05^c	0.07^c	0.08^c	0.06^c
(13) E_{651}	6505^{+25}_{-31}	6505^d					
(14) F_{651}	$0.07^{+0.03}_{-0.02}$	0.05^d	0.06^d	0.04^d	0.05^d	0.06^d	0.05^d
(15) δ_{Gain}	0(fix)	0(fix)	35(fix)	0(fix)	33(fix)	-18(fix)	71(fix)
χ^2/dof	192.33/181	56.06/51	70.76/78	40.89/25	21.01/15	82.35/93	6.81/18

Note—Parentheses indicate the 90% confidence limit. (1): Absorption column density (10^{23} H cm $^{-2}$). (2): Photon index. (3): Observed flux of a powerlaw continuum in the 5–8 keV band (10^{-4} photons cm $^{-2}$ s $^{-1}$). (4),(6),(8),(11),(13): Line centroid (eV). (5),(7),(10),(12),(14): Observed line flux (10^{-4} photons cm $^{-2}$ s $^{-1}$). (9): Line width in gaussian sigma (eV). The other line widths are fixed at zero. (15): Additional gain offset (eV).

^a Fixed at the value obtained in section 6.1.1.

^b The intensity of K β is fixed at 12.5% of that of K α (Kaastra & Mewe 1993).

^c The intensity of Fe XXVI K α is fixed at 30% of that of Fe XXV K α .

^d Fixed at the value and flux ratio against Fe XXV K α line obtained with Suzaku.

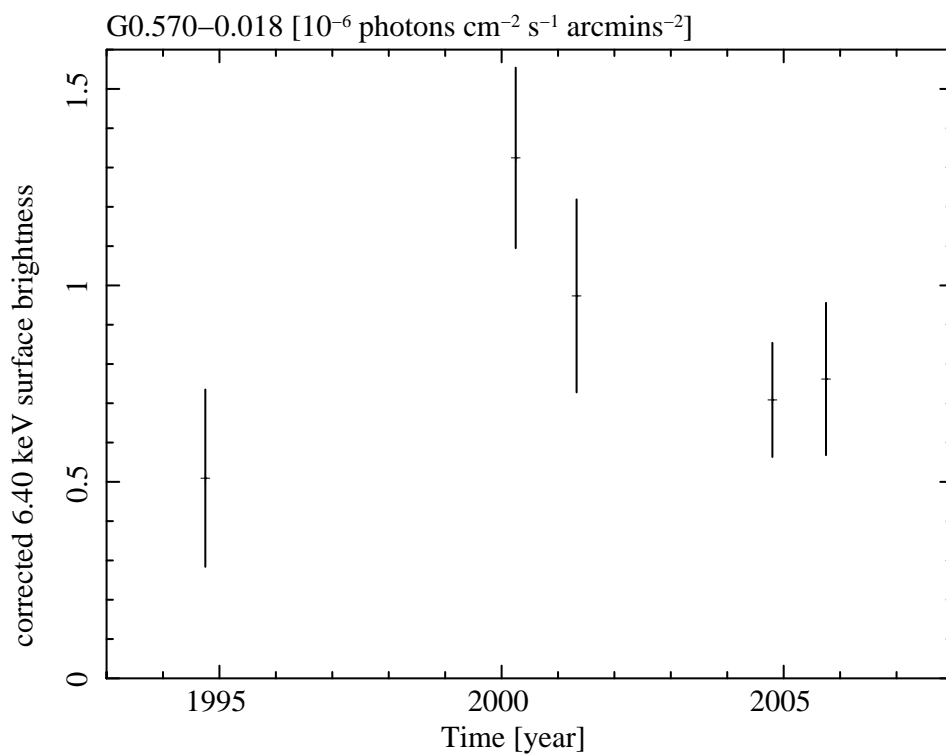


Figure 6.11: The light curve of the 6.40 keV line surface brightness from G 0.570–0.018. In this plot, each error bar indicates the 90% confidence limit.

Chapter 7

Summary and Discussion

7.1 Ionized Iron Line Sources

7.1.1 Galactic Center Diffuse X-ray Emission

With the Suzaku deep observation, we confirm that the Sgr B2 region is embedded in a thin hot plasma. The line ratio of 6.97/6.67 keV is 0.39 all over the Sgr B region except for G 0.61+0.01, which is quite consistent with that of the Galactic Center (Koyama et al. 2007d). Thus we conclude that this largely diffuse emission is the GCDX extending to this region. The intensity is about a half of the Sgr A region on the Galactic plane, decreasing to the Galactic latitude. This result can constrain the distribution of the GCDX against the Galactic longitude more strictly than that derived by Ginga, 1° – 2° .

7.1.2 Supernova Remnants

In addition to the distribution of the GCDX, we discover a clear excess in the 6.67 keV narrow band image. The source named as G 0.61+0.01 is a SNR candidate which is characterized by a strong 6.67 keV line emission. The high temperature and overabundance of iron are similar to those of Sgr A East (Koyama et al. 2007c). On the other hand, there is no low-temperature component which exists in Sgr A East. The lack of the low-temperature component may be explained by the tail-like structure below 6.67 keV line of G 0.61+0.01.

We found the iron line of low-ionization at 6.5 keV in G 0.570–0.018, which is consistent with the result of Senda et al. (2002). However, since the enhancement at the position of G 0.570–0.018 in the iron line map (shown in figure 6.6) faded away in the time span from 2000 to 2004, the image structure is mostly due to the 6.40 keV emission. The 6.5 keV line is located between the strong lines of

6.40 and 6.67 keV, we cannot distinguish the source with the narrow band imaging technique of Suzaku. Thus this low ionization line may be originated to a nearby source G 0.61+0.01. We, however, cannot exclude the origin is G 0.570–0.018 itself as a SNR source proposed in (Senda et al. 2002).

7.2 Neutral Iron Line Sources

7.2.1 The Origin

We measure the intensities of the 6.40 and the 7.06 keV line independently and confirm the flux ratio ($K\alpha/K\beta$) is consistent with 0.1. The ratio indicates the iron atom is nearly neutral (Kaastra & Mewe 1993). Then we discuss whether X-ray photons or energetic particles make the inner-shell ionization and illuminate the neutral molecular clouds.

The equivalent width of FeI $K\alpha$ is 1–2 keV by the X-ray irradiation, while the equivalent width is 300 eV by the collisional excitation by electrons assuming a molecular cloud with the solar abundance, which is reviewed in section 2.3. The observed equivalent width prefers the X-ray origin. However, since the metal abundance of GC is typically high, we cannot exclude the electron origin if the metallicity of the Sgr B2 region is 4 times a solar. Discussed in section 5.2.2, the deep absorption edge of Fe K also prefers the X-ray origin, but the electron origin cannot be excluded when electron bombardment takes place at the rear sides of the clouds. These spectral features strongly support the X-ray origin but cannot exclude the electron origin.

The time variability of the 6.40 keV line emission is the most decisive evidence for the X-ray origin. We found the variabilities not only in M 0.66–0.02, Sgr B2 cloud, but also in G 0.570–0.018. The sizes of M 0.66–0.02 and G 0.570–0.018 are ~ 10 light years, comparable to the variation time scale. This fact requires X-ray lights or relativistic particles as the external factor, however, high energy electrons have few cross section to neutral iron. On the other hand, protons, suggested by a TeV gamma-ray emission in the Galactic molecular clouds (Aharonian et al. 2006), can be also considered as the origin. Reviewed in section 2.3, the spectrum by proton impact is characterised by the broad bump features and the weak continuum with respect to the lines. We find no clear evidences for bump structures. In addition, we examine the variability of the continuum emission. Since the inverse bremsstrahlung by protons is very weak, no variability can be seen while the continuum is variable with the X-ray reflection by Thomson scattering. Figure 7.1 shows the variation

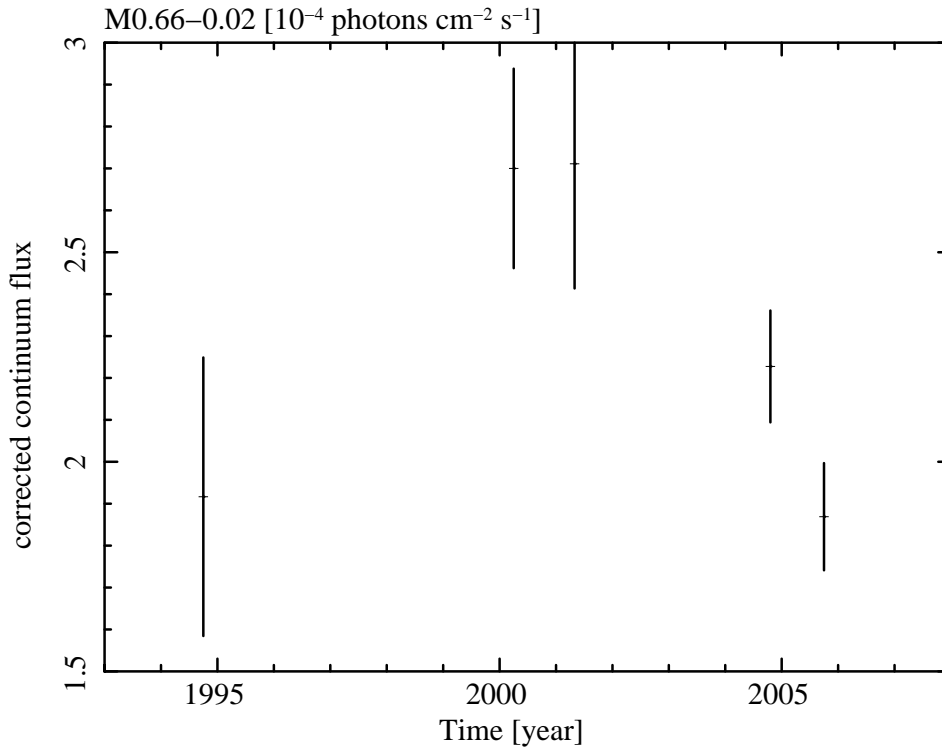


Figure 7.1: The time trend of the continuum fluxes in M 0.66–0.02. XMM values in 2001 and 2004 are the average of MOS and PN. In this plot, each error bar indicates the 90% confidence limit.

of the continuum (5–8 keV) flux in M 0.66–0.02. We can see a slight variation, whereas we do not discuss the significance because this continuum includes the thermal GCDX component and the CXB and suffers large systematic error caused by the background subtraction particularly in the XMM-Newton data.

With these observational results, we have concluded that the most likely origin of the neutral line emissions in the Sgr B2 complex is X-ray fluorescence.

7.2.2 Relation to the Past Activity of Sgr A*

Since the similar spectral features in M 0.66–0.02 and M 0.74–0.09 and the similar variation in M 0.66–0.02 and G 0.570–0.018, we consider these three sources have the same origin. The variation time scale and intensity of the 6.40 keV line requires a bright source with a luminosity of more than 10^{37} erg s⁻¹ located at the distance of a few parsec from the 6.40 keV sources. The point sources in the Galactic center region have been catalogued with many satellites, but no transient source brighter

than 10^{37} erg s^{-1} in a time scale of ten years has been ever found. Thus we have concluded that the most probable source is our Galactic massive black hole Sgr A*.

With this scenerio, the light curves of the 6.40 keV line flux in the molecular clouds can be regarded as the light curve of Sgr A* in the past. The required luminosity to account for the 6.40 keV flux in 2000 is 2×10^{39} ergs s^{-1} (Murakami et al. 2001), and decreases to about a half in 2005. Sgr A* shows frequent short-term (~ 1 hour) and low-level (~ 10 – 100 times of the quiescent level) flares (Baganoff et al. 2001), however, no variation with long time scale (10 years) is ever found in the present Sgr A*. Similar variabilities are also found in the molecular cloud in the Sgr A region, M0.11–0.11, and indicate an outburst of Sgr A* with a luminosity of at least 10^{38} ergs s^{-1} , which would have occurred about 60 years ago and lasted 2–3 years (Muno et al. 2007). The variabilities of the Sgr B2 clouds also suggest that Sgr A* was in an active phase about 300 years ago, 10^6 times brighter than the present, and experienced a giant flare. The X-rays illuminate the molecular clouds after 300 years travel. We now see a decay of the flare as the fluorescence iron emission of molecular clouds.

Acknowledgement

First of all, I am deeply grateful to my supervisor, Prof. K. Koyama, Assoc. Prof. T. Tsuru, and Res. Assoc. H. Matsumoto for their continual guidance, advice and support throughout my graduate career. I also thank my collaborators, Prof. S. Yamauchi, Dr. H. Murakami, Mr. Y. Hyodo, Mr. Y. Takikawa and Mr. M. Nobukawa for thier helpful comments and constructive discussions. I thank all the members of the Cosmic-ray laboratory in Kyoto University for the daily discussion and insightful comments. I express my gratitude to all the members of the Suzaku team.

Finally I thank all my family and friends for thier encouragement.

References

- Aharonian, F., et al. 2004, *A&A*, 425, L13
- Aharonian, F., et al. 2006, *Nature*, 439, 695
- Atoyan, A., & Dermer, C. D. 2004, *ApJL*, 617, L123
- Baganoff, F. K., et al. 2001, *Nature*, 413, 45
- Baganoff, F. K., et al. 2003, *ApJ*, 591, 891
- Balick, B., & Brown, R. L. 1974, *ApJ*, 194, 265
- Bautz, M. W., Kissel, S. E., Prigozhin, G. Y., LaMarr, B., Burke, B. E., & Gregory, J. A. 2004, *Proc. SPIE*, 5501, 111
- Borkowski, K. J., Lyerly, W. J., & Reynolds, S. P. 2001, *ApJ*, 548, 820
- Burke, B. E., et al. 1994, *IEEE*, 41, 375
- Carter, J. A., & Read, A. M. 2007, *A&A*, 464, 1155
- Dogiel, V. A., Ichimura, A., Inoue, H., & Masai, K. 1998, *PASJ*, 50, 567
- Eckart, A., Schödel, R., Meyer, L., Trippe, S., Ott, T., & Genzel, R. 2006, *A&A*, 455, 1
- Eisenhauer, F., et al. 2005, *ApJ*, 628, 246
- Garcia, J. D., Fortner, R. J., & Kavanagh, T. M. 1973, *Reviews of Modern Physics*, 45, 111
- Gaume, R. A., Claussen, M. J., de Pree, C. G., Goss, W. M., & Mehringer, D. M. 1995, *ApJ*, 449, 663
- Gendreau, K. C. 1995, Ph.D. Thesis,
- Genzel, R., Schödel, R., Ott, T., Eckart, A., Alexander, T., Lacombe, F., Rouan, D., & Aschenbach, B. 2003, *Nature*, 425, 934
- Ghez, A. M., Salim, S., Hornstein, S. D., Tanner, A., Lu, J. R., Morris, M., Becklin, E. E., & Duchêne, G. 2005, *ApJ*, 620, 744
- Goldston, J. E., Quataert, E., & Igumenshchev, I. V. 2005, *ApJ*, 621, 785
- Goldwurm, A., Brion, E., Goldoni, P., Ferrando, P., Daigne, F., Decourchelle, A., Warwick, R. S., & Predehl, P. 2003, *ApJ*, 584, 751
- Gordon, M. A., Berkermann, U., Mezger, P. G., Zylka, R., Haslam, C. G. T., Kreysa, E., Sievers, A., & Lemke, R. 1993, *A&A*, 280, 208
- Green, D. A. 2004, *Bulletin of the Astronomical Society of India*, 32, 335
- Hoffmann, D. H. H., Brendel, C., Genz, H., Löw, W., Müller, S., & Richter, A. 1979, *Zeitschrift für Physik*, 293, 187
- Inoue, H. 1985, *Space Science Reviews*, 40, 317
- Kaastra, J. S., & Mewe, R. 1993, *A&AS*, 97, 443
- Kosack, K., et al. 2004, *ApJL*, 608, L97
- Koyama, K., Awaki, H., Kunieda, H., Takano, S., & Tawara, Y. 1989, *Nature*, 339, 603
- Koyama, K., Maeda, Y., Sonobe, T., Takeshima, T., Tanaka, Y., & Yamauchi, S. 1996, *PASJ*, 48, 249

- Koyama, K. et al. 2007a, PASJ, 59, S23,
Koyama, K. et al. 2007b, PASJ, 59, S221
Koyama, K. et al. 2007c, PASJ, 59, S237
Koyama, K. et al. 2007d, PASJ, 59, S245
Koyama, K. et al. 2008, PASJ, accepted (#3188) (astroph/0711.2853)
Liu, S., Petrosian, V., & Melia, F. 2004, ApJL, 611, L101
Maeda, Y., et al. 2002, ApJ, 570, 671
Makishima, K., et al. 1996, PASJ, 48, 171
Markoff, S. 2005, ApJL, 618, L103
Mayer-Hasselwander, H. A., et al. 1998, A&A, 335, 161
Mehringer, D. M., Palmer, P., & Goss, W. M. 1995, ApJS, 97, 497
Mehringer, D. M., & Menten, K. M. 1997, ApJ, 474, 346
Mitsuda, K. et al. 2007, PASJ, 59, S1
Miyazaki, A., & Tsuboi, M. 2000, ApJ, 536, 357
Mori, H., et al.. 2008, PASJ, accepted (#3131)
Morris, M., & Serabyn, E. 1996, ARA&A, 34, 645
Muno, M. P., et al. 2003, ApJ, 589, 225
Muno, M. P., Baganoff, F. K., Brandt, W. N., Park, S., & Morris, M. R. 2007, ApJL, 656, L69
Murakami, H., Koyama, K., & Maeda, Y. 2001, ApJ, 558, 687
Murakami, H. 2002, Ph.D. Thesis,
Nobukawa, M. et al. 2008, PASJ, accepted (#3110) (astroph/0712.0877)
Oka, T., Hasegawa, T., Sato, F., Tsuboi, M., & Miyazaki, A. 1998, ApJS, 118, 455
Ohashi, T., et al. 1996, PASJ, 48, 157
Park, S., et al. 2005, ApJ, 631, 964
Reid, M. J., Schneps, M. H., Moran, J. M., Gwinn, C. R., Genzel, R., Downes, D., & Roennaeng, B. 1988, ApJ, 330, 809
Rho, J., & Petre, R. 1998, ApJL, 503, L167
Sakano, M., Koyama, K., Murakami, H., Maeda, Y., & Yamauchi, S. 2002, ApJS, 138, 19
Sakano, M., Warwick, R.S., Decourchelle, A., & Predehl, P. 2004, MNRAS, 350, 129
Sato, F., Hasegawa, T., Whiteoak, J. B., & Miyawaki, R. 2000, ApJ, 535, 857
Schwartz, D. A., et al. 2000, Proc. SPIE, 4012, 28
Senda, A., Murakami, H., & Koyama, K. 2002, ApJ, 565, 1017
Serlemitsos, P. J., et al. 1995, PASJ, 47, 105
Serlemitsos, P. J., et al. 2007, PASJ, 59, S9
Strüder, L., et al. 2001, A&A, 365, L18

- Takagi, S., Murakami, H., & Koyama, K. 2002, *ApJ*, 573, 275
- Tanaka, Y., Inoue, H., & Holt, S. S. 1994, *PASJ*, 46, L37
- Tatischeff, V. 2003, in *Final Stage of Stellar Evolution*, ed. C. Motch & Hameury (EAS publication Series vol.7), 79
- Tawa, N., et al. 2008, *PASJ*, accepted (#3176)
- Tsuboi, M., Handa, T., & Ukita, N. 1999, *ApJS*, 120, 1
- Tsuchiya, K., et al. 2004, *ApJL*, 606, L115
- Turner, M. J. L., et al. 2001, *A&A*, 365, L27
- Valinia, A., Tatischeff, V., Arnaud, K., Ebisawa, K., & Ramaty, R. 2000, *ApJ*, 543, 733
- Weisskopf, M. C., Brinkman, B., Canizares, C., Garmire, G., Murray, S., & Van Speybroeck, L. P. 2002, *PASP*, 114, 1
- Weisskopf, M. C., et al. 2003, *Experimental Astronomy*, 16, 1
- Yamauchi, S., Kawada, M., Koyama, K., Kunieda, H., & Tawara, Y. 1990, *ApJ*, 365, 532
- Yuan, F., Quataert, E., & Narayan, R. 2004, *ApJ*, 606, 894
- Yusef-Zadeh, F., et al. 2006, *ApJ*, 644, 198
- Yusef-Zadeh, F., Munro, M., Wardle, M., & Lis, D. C. 2007, *ApJ*, 656, 847

Appendix A

Tables for Spectral Results of M 0.66–0.02

A.1 Continuum Models

Using N_{H} and Γ values obtained by Suzaku fit, we fit spectra with three types of continuum models (Model II–IV described in section 6.1.1).

A.2 Background Analysis of the MOS and the PN detector

Using the background correction factors derived in section 6.1.2, we multiplied the blank-sky background spectra. We fit source spectra applied with the new backgrounds. The results are shown in table A.4 and A.5.

Table A.1: The result of spectral fitting for M0.66–0.02 with Model II

Observatory	Suzaku	XMM-Newton		XMM-Newton		Chandra	ASCA
Detector	XIS	MOS	PN	MOS	PN	ACIS	SIS [†]
(1) N_{H}	$5.0^{+0.5}_{-0.3}$	$4.9^{+1.1}_{-1.0}$	$5.4^{+0.3}_{-0.2}$	$5.0^{+1.5}_{-1.5}$	$5.8^{+1.9}_{-1.7}$	$7.0^{+1.1}_{-0.9}$	$5.0^{+0.7}_{-1.0}$
(2) Γ	$3.0^{+0.3}_{-0.3}$	3.0^a					
(3) F_{pow}	$2.0^{+0.1}_{-0.1}$	$1.7^{+0.1}_{-0.1}$	$2.3^{+0.1}_{-0.1}$	$2.6^{+0.2}_{-0.2}$	$2.3^{+0.2}_{-0.2}$	$2.5^{+0.1}_{-0.1}$	$2.2^{+0.2}_{-0.2}$
—Neutral iron lines—							
(4) E_{640}	6399^{+4}_{-3}	6399^a					
(5) F_{640}	$0.66^{+0.02}_{-0.02}$	$0.59^{+0.02}_{-0.05}$	$0.57^{+0.03}_{-0.04}$	$0.89^{+0.10}_{-0.10}$	$0.80^{+0.10}_{-0.10}$	$1.00^{+0.06}_{-0.05}$	$0.99^{+0.12}_{-0.13}$
(6) E_{706}	7057^b						
(7) F_{706}	$0.06^{+0.04}_{-0.04}$	$0.07^{+0.04}_{-0.04}$	$0.05^{+0.02}_{-0.03}$	$0.10^{+0.09}_{-0.09}$	$0.11^{+0.08}_{-0.06}$	$0.12^{+0.04}_{-0.06}$	$0.17^{+0.08}_{-0.12}$
—Ionized iron lines—							
(8) E_{667}	6670^{+5}_{-5}	6670^a					
(9) σ_{667}	29^{+12}_{-16}	29^a					
(10) F_{667}	$0.36^{+0.02}_{-0.02}$	$0.30^{+0.02}_{-0.04}$	$0.25^{+0.03}_{-0.03}$	$0.40^{+0.09}_{-0.09}$	$0.24^{+0.08}_{-0.08}$	$0.25^{+0.04}_{-0.03}$	$0.40^{+0.12}_{-0.11}$
(11) E_{697}	6967^{+21}_{-21}	6967^a					
(12) F_{697}	$0.12^{+0.03}_{-0.02}$	0.10^c	0.08^c	0.13^c	0.08^c	0.08^c	0.13^c
(13) δ_{Gain}	0(fix)	0(fix)	23^{+13}_{-4}	0(fix)	36^{+1}_{-28}	-18^{+9}_{-3}	81^{+20}_{-19}
χ^2/dof	348.41/354	37.03/41	90.79/69	50.69/39	22.66/28	152.47/145	37.29/38

Note—Parentheses indicate the 90% confidence limit. (1): Absorption column density (10^{23} H cm $^{-2}$). (2): Photon index. (3): Observed flux of a powerlaw continuum in the 5–8 keV band (10^{-4} photons cm $^{-2}$ s $^{-1}$). (4),(6),(8),(11): Line centroid (eV). (5),(7),(10),(12): Observed line flux (10^{-4} photons cm $^{-2}$ s $^{-1}$). (9): Line width in gaussian sigma (eV). The other line widths are fixed at zero. (13): Additional gain offset (eV).

[†] Values are obtained from region 'P'.

^a Fixed at the value obtained with Suzaku fit.

^b The energy gap between K α (6400 eV) and K β (7058 eV) is fixed at the theoretical value (+658 eV) (Kaastra & Mewe 1993).

^c The intensity of Fe XXVI K α is fixed at 34% of that of Fe XXV K α obtained with Suzaku.

Table A.2: The result of spectral fitting for M0.66–0.02 with Model III

Observatory	Suzaku	XMM-Newton		XMM-Newton		Chandra	ASCA
Detector	XIS	MOS	PN	MOS	PN	ACIS	SIS [†]
(1) N_{H}	$5.0^{+0.5}_{-0.3}$	5.0^a					
(2) Γ	$3.0^{+0.3}_{-0.3}$	$3.1^{+0.6}_{-0.5}$	$2.1^{+0.3}_{-0.2}$	$2.0^{+0.8}_{-0.7}$	$2.0^{+0.7}_{-0.8}$	$1.5^{+0.5}_{-0.5}$	$3.0^{+0.7}_{-1.0}$
(3) F_{pow}	$2.0^{+0.1}_{-0.1}$	$1.6^{+0.1}_{-0.1}$	$2.4^{+0.1}_{-0.1}$	$3.0^{+0.2}_{-0.2}$	$2.5^{+0.2}_{-0.2}$	$2.7^{+0.1}_{-0.1}$	$2.2^{+0.2}_{-0.2}$
—Neutral iron lines—							
(4) E_{640}	6399^{+4}_{-3}	6399^a					
(5) F_{640}	$0.66^{+0.02}_{-0.02}$	$0.59^{+0.04}_{-0.05}$	$0.56^{+0.03}_{-0.05}$	$0.85^{+0.11}_{-0.11}$	$0.79^{+0.10}_{-0.10}$	$0.99^{+0.05}_{-0.05}$	$0.99^{+0.11}_{-0.13}$
(6) E_{706}	7057^b						
(7) F_{706}	$0.06^{+0.04}_{-0.04}$	$0.08^{+0.04}_{-0.04}$	$0.03^{+0.02}_{-0.03}$	$0.06^{+0.09}_{-0.06}$	$0.10^{+0.07}_{-0.07}$	$0.07^{+0.05}_{-0.04}$	$0.17^{+0.08}_{-0.12}$
—Ionized iron lines—							
(8) E_{667}	6670^{+5}_{-5}	6670^a					
(9) σ_{667}	29^{+12}_{-16}	29^a					
(10) F_{667}	$0.36^{+0.02}_{-0.02}$	$0.30^{+0.04}_{-0.04}$	$0.23^{+0.03}_{-0.03}$	$0.35^{+0.10}_{-0.10}$	$0.23^{+0.08}_{-0.08}$	$0.24^{+0.04}_{-0.04}$	$0.40^{+0.12}_{-0.11}$
(11) E_{697}	6967^{+21}_{-21}	6967^a					
(12) F_{697}	$0.12^{+0.03}_{-0.02}$	0.10^c	0.08^c	0.13^c	0.08^c	0.08^c	0.13^c
(13) δ_{Gain}	0(fix)	0(fix)	23^{+6}_{-4}	0(fix)	33^{+4}_{-27}	-19^{+10}_{-3}	81^{+35}_{-20}
χ^2/dof	348.41/354	36.98/41	74.91/69	46.19/39	18.78/28	142.83/145	37.29/38

Note—Parentheses indicate the 90% confidence limit. (1): Absorption column density (10^{23} H cm $^{-2}$). (2): Photon index. (3): Observed flux of a powerlaw continuum in the 5–8 keV band (10^{-4} photons cm $^{-2}$ s $^{-1}$). (4),(6),(8),(11): Line centroid (eV). (5),(7),(10),(12): Observed line flux (10^{-4} photons cm $^{-2}$ s $^{-1}$). (9): Line width in gaussian sigma (eV). The other line widths are fixed at zero. (13): Additional gain offset (eV).

[†] Values are obtained from region 'P'.

^a Fixed at the value obtained with Suzaku fit.

^b The energy gap between K α (6400 eV) and K β (7058 eV) is fixed at the theoretical value (+658 eV) (Kaastra & Mewe 1993).

^c The intensity of Fe XXVI K α is fixed at 34% of that of Fe XXV K α obtained with Suzaku.

Table A.3: The result of spectral fitting for M0.66–0.02 with Model IV

Observatory	Suzaku	XMM-Newton		XMM-Newton		Chandra	ASCA
Detector	XIS	MOS	PN	MOS	PN	ACIS	SIS [†]
(1) N_{H}	$5.0^{+0.5}_{-0.3}$	5.0^a					
(2) Γ	$3.0^{+0.3}_{-0.3}$	3.0^a					
(3) F_{pow}	$2.0^{+0.1}_{-0.1}$	$1.7^{+0.1}_{-0.1}$	$2.2^{+0.1}_{-0.1}$	$2.6^{+0.2}_{-0.2}$	$2.2^{+0.2}_{-0.2}$	$2.2^{+0.1}_{-0.1}$	$2.2^{+0.2}_{-0.2}$
—Neutral iron lines—							
(4) E_{640}	6399^{+4}_{-3}	6399^a					
(5) F_{640}	$0.66^{+0.02}_{-0.02}$	$0.58^{+0.05}_{-0.04}$	$0.58^{+0.04}_{-0.05}$	$0.89^{+0.10}_{-0.10}$	$0.81^{+0.10}_{-0.09}$	$1.05^{+0.05}_{-0.06}$	$0.99^{+0.11}_{-0.13}$
(6) E_{706}	7057^b						
(7) F_{706}	$0.06^{+0.04}_{-0.04}$	$0.07^{+0.04}_{-0.04}$	$0.05^{+0.03}_{-0.04}$	$0.10^{+0.09}_{-0.09}$	$0.13^{+0.07}_{-0.07}$	$0.14^{+0.05}_{-0.04}$	$0.17^{+0.08}_{-0.12}$
—Ionized iron lines—							
(8) E_{667}	6670^{+5}_{-5}	6670^a					
(9) σ_{667}	29^{+12}_{-16}	29^a					
(10) F_{667}	$0.36^{+0.02}_{-0.02}$	$0.30^{+0.04}_{-0.04}$	$0.26^{+0.04}_{-0.04}$	$0.40^{+0.09}_{-0.09}$	$0.26^{+0.07}_{-0.07}$	$0.31^{+0.04}_{-0.04}$	$0.40^{+0.12}_{-0.11}$
(11) E_{697}	6967^{+21}_{-21}	6967^a					
(12) F_{697}	$0.12^{+0.03}_{-0.02}$	0.10^c	0.09^c	0.13^c	0.09^c	0.10^c	0.13^c
(13) δ_{Gain}	0(fix)	0(fix)	28^{+6}_{-7}	0(fix)	36^{+6}_{-28}	-18^{+8}_{-11}	81^{+22}_{-20}
χ^2/dof	348.41/354	37.04/42	95.88/70	50.70/40	23.15/29	165.18/146	37.29/39

Note—Parentheses indicate the 90% confidence limit. (1): Absorption column density (10^{23} H cm⁻²). (2): Photon index. (3): Observed flux of a powerlaw continuum in the 5–8 keV band (10^{-4} photons cm⁻² s⁻¹). (4),(6),(8),(11): Line centroid (eV). (5),(7),(10),(12): Observed line flux (10^{-4} photons cm⁻² s⁻¹). (9): Line width in gaussian sigma (eV). The other line widths are fixed at zero. (13): Additional gain offset (eV).

[†] Values are obtained from region 'P'.

^a Fixed at the value obtained with Suzaku fit.

^b The energy gap between K α (6400 eV) and K β (7058 eV) is fixed at the theoretical value (+658 eV) (Kaastra & Mewe 1993).

^c The intensity of Fe XXVI K α is fixed at 34% of that of Fe XXV K α obtained with Suzaku.

Table A.4: The XMM-Newton 2004 results of spectral fitting for M0.66–0.02 with multiplied blank-sky backgrounds

Model	N_{H}	Γ	F_{pow}	F_{640}	F_{706}	F_{667}	F_{697}	δ_{Gain}	χ^2/dof
	(1)	(2)	(3)	(4)	(5)	(6)	(7)	(8)	(9)
XMM-Newton 2004 MOS [†]									
I
II
III
IV
XMM-Newton 2004 PN									
I	$5.9^{+0.3}_{-1.5}$	$3.0^{+0.3}_{-0.4}$	$2.0^{+0.1}_{-0.1}$	$0.57^{+0.04}_{-0.04}$	$0.03^{+0.03}_{-0.02}$	$0.25^{+0.03}_{-0.03}$	0.08^c	23^{+6}_{-4}	85.48/68
II	$5.6^{+0.4}_{-0.8}$	3.0^a	$1.9^{+0.1}_{-0.1}$	$0.57^{+0.04}_{-0.04}$	$0.04^{+0.02}_{-0.03}$	$0.25^{+0.03}_{-0.03}$	0.08^c	23^{+6}_{-4}	85.23/69
III	5.0^a	$2.7^{+0.3}_{-0.4}$	$2.0^{+0.1}_{-0.1}$	$0.58^{+0.04}_{-0.04}$	$0.04^{+0.02}_{-0.03}$	$0.26^{+0.03}_{-0.03}$	0.09^c	17^{+5}_{-4}	85.47/69
IV	5.0^a	3.0^a	$1.9^{+0.1}_{-0.1}$	$0.58^{+0.04}_{-0.04}$	$0.04^{+0.03}_{-0.02}$	$0.27^{+0.03}_{-0.03}$	0.09^c	23^{+7}_{-4}	86.93/70

Note—Parentheses indicate the 90% confidence limit. (1): Absorption column density (10^{23} H cm⁻²). (2): Photon index. (3): Observed flux of a powerlaw continuum in the 5–8 keV band (10^{-4} photons cm⁻² s⁻¹). (4),(5),(6),(7): Observed line flux of 6.40, 7.06, 6.67, 6.97 keV line (10^{-4} photons cm⁻² s⁻¹). (8): Additional gain offset (eV). (9): χ^2 value per Degree of Freedom.

[†] No correction is needed.

^a Fixed at the value obtained with Suzaku fit.

^c The intensity of Fe XXVI K α is fixed at 30% of that of Fe XXV K α determined by the Suzaku fit.

Table A.5: The XMM-Newton 2001 results of spectral fitting for M0.66–0.02 with multiplied blank-sky backgrounds

Model	N_{H}	Γ	F_{pow}	F_{640}	F_{706}	F_{667}	F_{697}	δ_{Gain}	χ^2/dof
	(1)	(2)	(3)	(4)	(5)	(6)	(7)	(8)	(9)
XMM-Newton 2001 MOS									
I	$4.4^{+8.1}_{-4.4}$	$3.9^{+3.1}_{-2.5}$	$1.4^{+0.2}_{-0.2}$	$0.90^{+0.11}_{-0.11}$	$0.07^{+0.09}_{-0.07}$	$0.41^{+0.09}_{-0.09}$	0.14^c	0(fix)	35.64/38
II	$2.9^{+2.1}_{-2.2}$	3.0^a	$1.5^{+0.2}_{-0.2}$	$0.91^{+0.11}_{-0.11}$	$0.06^{+0.09}_{-0.06}$	$0.41^{+0.09}_{-0.09}$	0.14^c	0(fix)	35.89/39
III	5.0^a	$4.2^{+0.8}_{-1.2}$	$1.4^{+0.2}_{-0.2}$	$0.90^{+0.11}_{-0.11}$	$0.07^{+0.09}_{-0.07}$	$0.41^{+0.09}_{-0.09}$	0.14^c	0(fix)	35.66/39
IV	5.0^a	3.0^a	$1.6^{+0.2}_{-0.2}$	$0.88^{+0.11}_{-0.10}$	$0.04^{+0.08}_{-0.04}$	$0.37^{+0.09}_{-0.09}$	0.12^c	0(fix)	38.11/40
XMM-Newton 2001 PN									
I	$10.6^{+11.0}_{-3.9}$	$6.1^{+3.9}_{-3.4}$	$1.1^{+0.2}_{-0.2}$	$0.83^{+0.10}_{-0.10}$	$0.12^{+0.08}_{-0.07}$	$0.27^{+0.08}_{-0.08}$	0.09^c	33^{+1}_{-32}	17.68/27
II	$5.0^{+3.8}_{-3.6}$	3.0^a	$1.2^{+0.2}_{-0.2}$	$0.83^{+0.09}_{-0.10}$	$0.12^{+0.08}_{-0.08}$	$0.29^{+0.08}_{-0.07}$	0.10^c	21^{+13}_{-16}	19.94/28
III	5.0^a	$3.8^{+1.9}_{-1.5}$	$1.1^{+0.2}_{-0.2}$	$0.85^{+0.10}_{-0.10}$	$0.12^{+0.09}_{-0.07}$	$0.30^{+0.08}_{-0.08}$	0.10^c	33^{+6}_{-27}	19.28/28
IV	5.0^a	3.0^a	$1.2^{+0.2}_{-0.2}$	$0.83^{+0.10}_{-0.09}$	$0.12^{+0.08}_{-0.08}$	$0.29^{+0.07}_{-0.07}$	0.10^c	21^{+17}_{-15}	19.94/29

Note—Parentheses indicate the 90% confidence limit. (1): Absorption column density (10^{23} H cm $^{-2}$). (2): Photon index. (3): Observed flux of a powerlaw continuum in the 5–8 keV band (10^{-4} photons cm $^{-2}$ s $^{-1}$). (4),(5),(6),(7): Observed line flux of 6.40, 7.06, 6.67, 6.97 keV line (10^{-4} photons cm $^{-2}$ s $^{-1}$). (8): Additional gain offset (eV). (9): χ^2 value per Degree of Freedom.

^a Fixed at the value obtained with Suzaku fit.

^c The intensity of Fe XXVI K α is fixed at 30% of that of Fe XXV K α determined by the Suzaku fit.

Appendix B

Tables for Spectral Results of G 0.570–0.018

B.1 Continuum Models

Suzaku spectral analysis mentioned in 6.2.3 requires one additional line component for G 0.570–0.018. We fit spectra with Model II–IV including this line component.

B.2 Background Analysis of the MOS and the PN detector

Using the background correction factors derived in section 6.1.2, we multiplied the blank-sky background spectra. We fit source spectra applied with the new backgrounds. The results are shown in table B.4 and B.5.

Table B.1: The result of spectral fitting for G 0.570–0.018 with Model II plus one Gaussian function

Observatory	Suzaku	XMM-Newton		XMM-Newton		Chandra	ASCA
Detector	XIS	MOS	PN	MOS	PN	ACIS	SIS
(1) N_{H}	$1.5^{+1.3}_{-1.0}$	$3.7^{+0.8}_{-0.8}$	$1.8^{+0.6}_{-0.6}$	$5.0^{+0.9}_{-1.0}$	$2.6^{+1.1}_{-1.3}$	$2.9^{+1.2}_{-1.2}$	$2.9^{+1.9}_{-1.9}$
(2) Γ	$2.6^{+0.6}_{-0.5}$	2.6^a					
(3) F_{pow}	$1.1^{+0.2}_{-0.2}$	$1.1^{+0.1}_{-0.1}$	$1.3^{+0.1}_{-0.1}$	$1.8^{+0.1}_{-0.1}$	$1.2^{+0.1}_{-0.1}$	$1.1^{+0.1}_{-0.1}$	$0.9^{+0.1}_{-0.1}$
—Neutral iron lines—							
(4) E_{640}	6400^a						
(5) F_{640}	$0.16^{+0.02}_{-0.03}$	$0.11^{+0.04}_{-0.04}$	$0.13^{+0.03}_{-0.03}$	$0.17^{+0.06}_{-0.06}$	$0.19^{+0.06}_{-0.06}$	$0.26^{+0.04}_{-0.04}$	$0.11^{+0.054}_{-0.05}$
(6) E_{706}	7058^a						
(7) F_{706}	0.02^b	0.01^b	0.02^b	0.02^b	0.02^b	0.03^b	0.01^b
—Ionized iron lines—							
(8) E_{667}	6665^a						
(9) σ_{667}	27^a						
(10) F_{667}	$0.29^{+0.02}_{-0.02}$	$0.21^{+0.04}_{-0.04}$	$0.22^{+0.03}_{-0.03}$	$0.17^{+0.06}_{-0.06}$	$0.23^{+0.06}_{-0.06}$	$0.25^{+0.03}_{-0.03}$	$0.20^{+0.05}_{-0.05}$
(11) E_{697}	6966^a						
(12) F_{697}	0.09^c	0.07^c	0.07^c	0.05^c	0.07^c	0.08^c	0.06^c
(13) E_{651}	6505^{+25}_{-31}	6505^d					
(14) F_{651}	$0.07^{+0.03}_{-0.02}$	0.05^d	0.05^d	0.04^d	0.06^d	0.06^d	0.05^d
(15) δ_{Gain}	0(fix)	0(fix)	35(fix)	0(fix)	33(fix)	-18(fix)	71(fix)
χ^2/dof	192.33/181	58.38/52	73.07/79	48.12/26	21.35/16	82.71/94	9.21/19

Note—Parentheses indicate the 90% confidence limit. (1): Absorption column density (10^{23} H cm $^{-2}$). (2): Photon index. (3): Observed flux of a powerlaw continuum in the 5–8 keV band (10^{-4} photons cm $^{-2}$ s $^{-1}$). (4),(6),(8),(11),(13): Line centroid (eV). (5),(7),(10),(12),(14): Observed line flux (10^{-4} photons cm $^{-2}$ s $^{-1}$). (9): Line width in gaussian sigma (eV). The other line widths are fixed at zero. (15): Additional gain offset (eV).

^a Fixed at the value obtained with Suzaku fit.

^b The intensity of K β is fixed at 12.5% of that of K α (Kaastra & Mewe 1993).

^c The intensity of Fe XXVI K α is fixed at 30% of that of Fe XXV K α obtained with Suzaku.

Table B.2: The result of spectral fitting for G 0.570–0.018 with Model III plus one Gaussian function

Observatory	Suzaku	XMM-Newton		XMM-Newton		Chandra	ASCA
Detector	XIS	MOS	PN	MOS	PN	ACIS	SIS
(1) N_{H}	$1.5^{+1.3}_{-1.0}$	1.5^a					
(2) Γ	$2.6^{+0.6}_{-0.5}$	$2.0^{+0.6}_{-0.7}$	$1.8^{+0.8}_{-0.6}$	$0.6^{+0.7}_{-0.6}$	$2.0^{+0.8}_{-0.8}$	$1.8^{+0.6}_{-0.5}$	$1.7^{+0.8}_{-0.7}$
(3) F_{pow}	$1.1^{+0.2}_{-0.2}$	$1.1^{+0.1}_{-0.1}$	$1.3^{+0.1}_{-0.1}$	$1.9^{+0.1}_{-0.1}$	$1.2^{+0.1}_{-0.1}$	$1.0^{+0.1}_{-0.1}$	$0.9^{+0.1}_{-0.1}$
—Neutral iron lines—							
(4) E_{640}	6400^a						
(5) F_{640}	$0.16^{+0.02}_{-0.03}$	$0.11^{+0.04}_{-0.03}$	$0.13^{+0.03}_{-0.03}$	$0.20^{+0.04}_{-0.08}$	$0.19^{+0.06}_{-0.06}$	$0.26^{+0.04}_{-0.04}$	$0.11^{+0.05}_{-0.05}$
(6) E_{706}	7058^a						
(7) F_{706}	0.02^b	0.01^b	0.02^b	0.02^b	0.02^b	0.03^b	0.01^b
—Ionized iron lines—							
(8) E_{667}	6665^a						
(9) σ_{667}	27^a						
(10) F_{667}	$0.29^{+0.02}_{-0.02}$	$0.22^{+0.04}_{-0.04}$	$0.22^{+0.03}_{-0.03}$	$0.18^{+0.06}_{-0.06}$	$0.23^{+0.06}_{-0.06}$	$0.25^{+0.03}_{-0.03}$	$0.20^{+0.05}_{-0.05}$
(11) E_{697}	6966^a						
(12) F_{697}	0.09^c	0.07^c	0.07^c	0.05^c	0.07^c	0.08^c	0.06^c
(13) E_{651}	6505^{+25}_{-31}	6505^d					
(14) F_{651}	$0.07^{+0.03}_{-0.02}$	0.06^d	0.05^d	0.04^d	0.06^d	0.06^d	0.05^d
(15) δ_{Gain}	0(fix)	0(fix)	35(fix)	0(fix)	33(fix)	-18(fix)	71(fix)
χ^2/dof	192.33/181	62.86/52	71.81/79	41.20/26	21.01/16	82.39/94	7.24/19

Note—Parentheses indicate the 90% confidence limit. (1): Absorption column density (10^{23} H cm $^{-2}$). (2): Photon index. (3): Observed flux of a powerlaw continuum in the 5–8 keV band (10^{-4} photons cm $^{-2}$ s $^{-1}$). (4),(6),(8),(11),(13): Line centroid (eV). (5),(7),(10),(12),(14): Observed line flux (10^{-4} photons cm $^{-2}$ s $^{-1}$). (9): Line width in gaussian sigma (eV). The other line widths are fixed at zero. (15): Additional gain offset (eV).

^a Fixed at the value obtained with Suzaku fit.

^b The intensity of K β is fixed at 12.5% of that of K α (Kaastra & Mewe 1993).

^c The intensity of Fe XXVI K α is fixed at 30% of that of Fe XXV K α obtained with Suzaku.

Table B.3: The result of spectral fitting for G 0.570–0.018 with Model IV plus one Gaussian function

Observatory	Suzaku	XMM-Newton		XMM-Newton		Chandra	ASCA
Detector	XIS	MOS	PN	MOS	PN	ACIS	SIS
(1) N_{H}	$1.5_{-1.0}^{+1.3}$	1.5^a					
(2) Γ	$2.6_{-0.5}^{+0.6}$	2.6^a					
(3) F_{pow}	$1.1_{-0.2}^{+0.2}$	$1.0_{-0.1}^{+0.1}$	$1.3_{-0.1}^{+0.1}$	$1.5_{-0.1}^{+0.1}$	$1.2_{-0.1}^{+0.1}$	$1.2_{-0.1}^{+0.1}$	$0.8_{-0.1}^{+0.1}$
—Neutral iron lines—							
(4) E_{640}	6400^a						
(5) F_{640}	$0.16_{-0.03}^{+0.02}$	$0.12_{-0.03}^{+0.04}$	$0.14_{-0.03}^{+0.03}$	$0.22_{-0.06}^{+0.06}$	$0.20_{-0.06}^{+0.06}$	$0.27_{-0.03}^{+0.03}$	$0.12_{-0.05}^{+0.05}$
(6) E_{706}	7058^a						
(7) F_{706}	0.02^b	0.01^b	0.02^b	0.03^b	0.02^b	0.03^b	0.01^b
—Ionized iron lines—							
(8) E_{667}	6665^a						
(9) σ_{667}	27^a						
(10) F_{667}	$0.29_{-0.02}^{+0.02}$	$0.23_{-0.03}^{+0.04}$	$0.22_{-0.03}^{+0.03}$	$0.24_{-0.05}^{+0.05}$	$0.24_{-0.05}^{+0.05}$	$0.26_{-0.03}^{+0.03}$	$0.22_{-0.04}^{+0.04}$
(11) E_{697}	6966^a						
(12) F_{697}	0.09^c	0.07^c	0.07^c	0.07^c	0.08^c	0.08^c	0.07^c
(13) E_{651}	6505_{-31}^{+25}	6505^d					
(14) F_{651}	$0.07_{-0.02}^{+0.03}$	0.06^d	0.06^d	0.06^d	0.06^d	0.06^d	0.05^d
(15) δ_{Gain}	0(fix)	0(fix)	35(fix)	0(fix)	33(fix)	-18(fix)	71(fix)
χ^2/dof	192.33/181	64.69/53	73.28/80	51.44/27	22.09/17	86.00/95	10.54/20

Note—Parentheses indicate the 90% confidence limit. (1): Absorption column density (10^{23} H cm $^{-2}$). (2): Photon index. (3): Observed flux of a powerlaw continuum in the 5–8 keV band (10^{-4} photons cm $^{-2}$ s $^{-1}$). (4),(6),(8),(11),(13): Line centroid (eV). (5),(7),(10),(12),(14): Observed line flux (10^{-4} photons cm $^{-2}$ s $^{-1}$). (9): Line width in gaussian sigma (eV). The other line widths are fixed at zero. (15): Additional gain offset (eV).

^a Fixed at the value obtained with Suzaku fit.

^b The intensity of K β is fixed at 12.5% of that of K α (Kaastra & Mewe 1993).

^c The intensity of Fe XXVI K α is fixed at 30% of that of Fe XXV K α obtained with Suzaku.

Table B.4: The XMM-Newton 2004 results of spectral fitting for G 0.570–0.018 with multiplied blank-sky backgrounds

Model	N_{H}	Γ	F_{pow}	F_{640}	F_{706}	F_{667}	F_{697}	F_{651}	δ_{Gain}	χ^2/dof
	(1)	(2)	(3)	(4)	(5)	(6)	(7)	(8)	(9)	(10)
XMM-Newton 2004 MOS [†]										
I
II
III
IV
XMM-Newton 2004 PN										
I	$0.4^{+1.7}_{-0.4}$	$1.8^{+0.8}_{-0.6}$	$1.3^{+0.1}_{-0.1}$	$0.14^{+0.03}_{-0.03}$	0.02^b	$0.22^{+0.03}_{-0.03}$	0.07^c	0.06^d	35(fix)	70.76/78
II	$1.8^{+0.6}_{-0.6}$	2.6^a	$1.3^{+0.1}_{-0.1}$	$0.13^{+0.03}_{-0.03}$	0.02^b	$0.22^{+0.03}_{-0.03}$	0.07^c	0.05^d	35(fix)	73.07/79
III	1.5^a	$2.2^{+0.5}_{-0.4}$	$1.3^{+0.1}_{-0.1}$	$0.13^{+0.03}_{-0.03}$	0.02^b	$0.21^{+0.03}_{-0.03}$	0.07^c	0.05^d	35(fix)	71.81/79
IV	1.5^a	2.6^a	$1.3^{+0.1}_{-0.1}$	$0.14^{+0.03}_{-0.03}$	0.02^b	$0.22^{+0.03}_{-0.03}$	0.07^c	0.06^d	35(fix)	73.28/80

Note—Parentheses indicate the 90% confidence limit. (1): Absorption column density (10^{23} H cm⁻²). (2): Photon index. (3): Observed flux of a powerlaw continuum in the 5–8 keV band (10^{-4} photons cm⁻² s⁻¹). (4),(5),(6),(7),(8): Observed line flux of 6.40, 7.06, 6.67, 6.97, 6.51 keV line (10^{-4} photons cm⁻² s⁻¹). (9): Additional gain offset (eV). (10): χ^2 value per Degree of Freedom.

[†] No correction is needed.

^a Fixed at the value obtained with Suzaku fit.

^c The intensity of Fe XXVI K α is fixed at 30% of that of Fe XXV K α determined by the Suzaku fit.

Table B.5: The XMM-Newton 2001 results of spectral fitting for G 0.570–0.018 with multiplied blank-sky backgrounds

Model	N_{H}	Γ	F_{pow}	F_{640}	F_{706}	F_{667}	F_{697}	F_{651}	δ_{Gain}	χ^2/dof
	(1)	(2)	(3)	(4)	(5)	(6)	(7)	(8)	(9)	(10)
XMM-Newton 2004 MOS [†]										
I	$1.3^{+1.4}_{-1.3}$	$0.5^{+1.2}_{-0.9}$	$1.9^{+0.1}_{-0.1}$	$0.18^{+0.06}_{-0.06}$	0.02^b	$0.18^{+0.06}_{-0.06}$	0.05^c	0.04^d	0(fix)	40.89/25
II	$5.0^{+0.9}_{-1.0}$	2.6^a	$1.8^{+0.1}_{-0.1}$	$0.17^{+0.06}_{-0.06}$	0.02^b	$0.17^{+0.06}_{-0.06}$	0.05^c	0.04^d	0(fix)	48.12/26
III	1.5^a	$0.6^{+0.7}_{-0.6}$	$1.9^{+0.1}_{-0.1}$	$0.20^{+0.04}_{-0.08}$	0.02^b	$0.18^{+0.06}_{-0.06}$	0.05^c	0.04^d	0(fix)	41.20/26
IV	1.5^a	2.6^a	$1.5^{+0.1}_{-0.1}$	$0.22^{+0.06}_{-0.06}$	0.03^b	$0.24^{+0.05}_{-0.05}$	0.07^c	0.06^d	0(fix)	51.44/27
XMM-Newton 2004 PN										
I	$1.5^{+3.6}_{-1.5}$	$2.0^{+1.6}_{-1.2}$	$1.2^{+0.1}_{-0.1}$	$0.19^{+0.06}_{-0.06}$	0.02^b	$0.23^{+0.06}_{-0.06}$	0.07^c	0.06^d	33(fix)	21.01/15
II	$2.6^{+1.1}_{-1.3}$	2.6^a	$1.2^{+0.1}_{-0.1}$	$0.19^{+0.06}_{-0.06}$	0.02^b	$0.23^{+0.06}_{-0.06}$	0.07^c	0.06^d	33(fix)	21.35/16
III	1.5^a	$2.0^{+0.8}_{-0.8}$	$1.2^{+0.1}_{-0.1}$	$0.19^{+0.06}_{-0.06}$	0.02^b	$0.23^{+0.06}_{-0.06}$	0.07^c	0.06^d	33(fix)	21.01/16
IV	1.5^a	2.6^a	$1.2^{+0.1}_{-0.1}$	$0.20^{+0.06}_{-0.06}$	0.02^b	$0.24^{+0.05}_{-0.05}$	0.08^c	0.06^d	33(fix)	22.09/17

Note—Parentheses indicate the 90% confidence limit. (1): Absorption column density (10^{23} H cm⁻²). (2): Photon index. (3): Observed flux of a powerlaw continuum in the 5–8 keV band (10^{-4} photons cm⁻² s⁻¹). (4),(5),(6),(7),(8): Observed line flux of 6.40, 7.06, 6.67, 6.97, 6.51 keV line (10^{-4} photons cm⁻² s⁻¹). (9): Additional gain offset (eV). (10): χ^2 value per Degree of Freedom.

[†] No correction is needed.

^a Fixed at the value obtained with Suzaku fit.

^c The intensity of Fe XXVI K α is fixed at 30% of that of Fe XXV K α determined by the Suzaku fit.